ANALYSIS OF STRAIN IN A WELDED BLOCK AND ASH FLOW DEPOSIT, MOUNT MEAGER, SOUTHWESTERN BRITISH COLUMBIA

by

KRISTA A. MICHOL

BSc. (Honours), University of Ottawa, 2004

A THESIS SUBMITTED IN PARTIAL FULFILLMENT OF
THE REQUIREMENTS FOR THE DEGREE OF

MASTER OF SCIENCE

in

THE FACULTY OF GRADUATE STUDIES

(GEOLOGICAL SCIENCES)

THE UNIVERSITY OF BRITISH COLUMBIA

December 2006

ABSTRACT

The 2360 BP eruption of Mount Meager, British Columbia has produced a rare welded block and ash flow deposit along with non-welded equivalents. Here, I report on this sequence of block and ash flow deposits (herein referred to as the Keyhole Falls Member) with the aim of documenting the effects of welding and the mechanisms of strain attending the welding process. Multiple texture maps are drawn at the decimeter scale (field texture maps), and at the centimeter scale (slab texture maps), and are used for image analysis purposes to quantify the transition from unconsolidated block and ash flow deposits to dense, vitroclastic breccias. Image analysis establishes a welding trajectory, whereby average clast oblateness increases and average clast orientation (relative to the horizontal) decreases with increasing welding intensity. After accounting for an original oblateness of approximately 30%, estimates of strain from image analysis of field texture maps (FTMs) and slab texture maps (STMs) yield a volume strain of ~12%, or ~9% if treated as pure shear strain. An empirical experiment using image analysis of FTMs suggests that the most welded FTMs visually correspond to 30 – 40% volume strain relative to the least welded portions of the deposit. Distributions of oblateness and orientation for each FTM also prove more accurate in indicating welding intensity than do the average values. Physical property measurements of the non-welded and welded block and ash flow deposits correlate well with the empirical experiments. Unconsolidated deposits reveal an average total matrix porosity of ~41%, of which less than 1% is isolated porosity. Associated clasts possess an average of ~32% total porosity, with a maximum of 11% isolated porosity. As welding intensity increases, these values of average total porosity decrease to ~5% for clasts and ~17% for matrix. Isolated porosity is reduced to $\leq 1\%$ for both components. Thus, isolated

porosity is present mostly in non-welded clasts, and is lost in conjunction with connected porosity as welding progresses. These results also reveal an approximately equal amount of strain in clasts and matrix. The variations in physical property measurements suggest that both components record a maximum volume strain of ~38%, which is echoed in the results of the empirical experiment. There is also little manifestation of pure shear stress observed within the welded facies of the deposit (e.g. only occurs as rare pull-apart clasts and locally around accidental lithics), indicating that volume strain in the viscous regime is the main mechanism for welding of the Keyhole Falls Member. The deposit, as a whole, records an average of 31% strain, meaning that the lower block and ash flow deposits experienced 50 m of compaction during welding, form 162 to 112 m. In comparing the block and ash flow deposits to other volcanic deposits, it is evident that they were erupted in a more explosive manner than originally proposed. The most appropriate analogue is Soufrière Hills Volcano, Montserrat, where explosive dome collapse is triggered by a Vulcanian eruption.

TABLE OF CONTENTS

LIST OF FIGURES

LIST OF TABLES

ACKNOWLEDGEMENTS

CHAPTER ONE

INTRODUCTION

1.1. Block and Ash Flows and their Deposits

Block and ash flows, also known as nuées ardentes, are small-volume pyroclastic flows (generally less than 1 km^3) generated by the explosive or gravitational collapse of lava flows or domes (Cas and Wright, 1987). Block and ash flow deposits are topographically controlled, unsorted deposits with an ash-rich matrix and a near-monolithologic assemblage of generally poorly vesiculated clasts, commonly having radial cooling joints (Cas and Wright, 1987). They are deposited as hot avalanche-type deposits, commonly with reversely graded flow units, and may contain carbonized wood. Classic examples include deposits from Merapi (Bardintzeff, 1984; Boudon et al., 1993; Abdurachman et al., 2000), Unzen (Sato et al., 1992; Ui et al., 1999), and Montserrat (Calder et al., 2002; Woods et al., 2002). They differ from other pyroclastic flows (i.e., ignimbrites) in that ignimbrites generally contain variable amounts of ash, and the lapilli and block-sized clasts are pumiceous (e.g., porosity > 50%) (Cas and Wright, 1987). They are also distinguishable from debris flows and rock avalanches in that debris flows are much more diluted in terms of pyroclastic material, and rock avalanches are deposited cold. Similarly to rock avalanches, block and ash flows represent a significant hazard to human life and infrastructure, only more so due to their higher emplacement temperatures, increased fluidization from degassing, and the potential to decouple highly mobile elutriated ash clouds (Bourdier and Abdurachman, 2001; Stewart et al., 2003).

1

1.2. Welding in Volcaniclastic Deposits

Although most pyroclastic deposits are known to weld, welded block and ash flow deposits are apparently rare. Cas and Wright (1987, p.111) state that there are no previously documented occurrences. Welding is characterized by the coalescence of hot glassy pyroclasts (sintering) that typically involves concomitant flattening or stretching of pyroclasts due to a compactional load (Smith, 1960b; Guest and Rogers, 1967; Riehle et al., 1995). Generally, welding processes require temperatures above the melt's characteristic glass transition temperature (T_g: Giordano et al., 2000; Giordano et al., 2005; Russell and Quane, 2005). The best studied examples of welded pyroclastic deposits are silicic ignimbrites (Sheridan and Ragan, 1976; Streck and Grunder, 1995; Wilson and Hildreth, 2003; Quane and Russell, 2005a). However, welding processes operate on a variety of volcanic deposit types, including other pyroclastic flow deposits (Smith, 1960a,b; Boyd, 1961), pyroclastic fall deposits (Sparks and Wright, 1979), spatter-fed lavas (Wolff and Sumner, 2000; Gottsman and Dingwell, 2001), fire-fountain deposits (Sumner et al., 2005), the clastic bases and margins of lava flows (Naranjo et al., 1992; Sparks et al., 1993), and within infilled volcanic conduits (Kano et al., 1997; Tuffen et al., 2003). Welding is also common in subaqueous volcanic successions (e.g., Kokelaar & Busby, 1992; White & McPhie, 1997; Kokelaar & Königer, 2000). Welded deposits encompass a variety of magma compositions, from basalts to rhyolites, and even carbonatites (Barker and Nixon, 1983). In extreme cases, intensely welded deposits also experience ductile flow (rheomorphism) both during and after emplacement (Schmincke and Swanson, 1967; Wolff and Wright, 1981; Branney and Kokelaar, 1992; Soriano et al., 2002). The extent or intensity of the welding process is commonly manifest by combinations of the following: (a) decreases in porosity, (b) increases in density (Ragan and Sheridan, 1972; Streck and Grunder, 1995; Rust and Russell,

2000), (c) development of a foliation (Smith 1960a,b; Ragan and Sheridan, 1972; Sheridan and Ragan, 1976; Peterson, 1979; Quane and Russell, 2005b), and (d) increasing rock strength (Quane & Russell, 2005a). Mechanisms for welding include one or a combination of: (a) viscous deformation controlled by bubble collapse (Sheridan and Ragan, 1976); (b) viscous deformation due to shear strain (Smith, 1960a; Guest and Rogers, 1967; Ragan and Sheridan, 1972); and/or (c) mechanical deformation, should the deposit be cooler than its glass transition temperature (Sheridan and Ragan, 1976). Factors that appear to govern welding intensity include: melt rheology, emplacement temperature, volatile content, mass flux during deposition, cooling history, deposit thickness, permeability, and particle size distribution (Sparks et al., 1999; Giordano et al., 2000; Quane and Russell, 2005b; Russell and Quane, 2005).

Here I describe a unique welded block and ash flow deposit (the Keyhole Falls Member) at Mount Meager, southwestern British Columbia (Fig. 1). I define vertical welding facies variations within the deposit using a combination of field and laboratory techniques to quantify how strain is accommodated during welding. Texture mapping, image analysis, petrography, and physical property measurements allow me to document the welding trajectory of the Keyhole Falls member and recover the unique conditions and mechanism(s) under which this deposit has formed. These data sets also offer new insights into welding of non-coherent volcaniclastic deposits other than ignimbrites. My study demonstrates that components of welded block and ash flows behave differently than those found in ignimbrites, and that the amount of strain required to densely weld this particular block and ash flow deposit is significantly less than typical densely welded ignimbrites. Thus, my results will help to generalize our understanding of welding processes in volcanology.
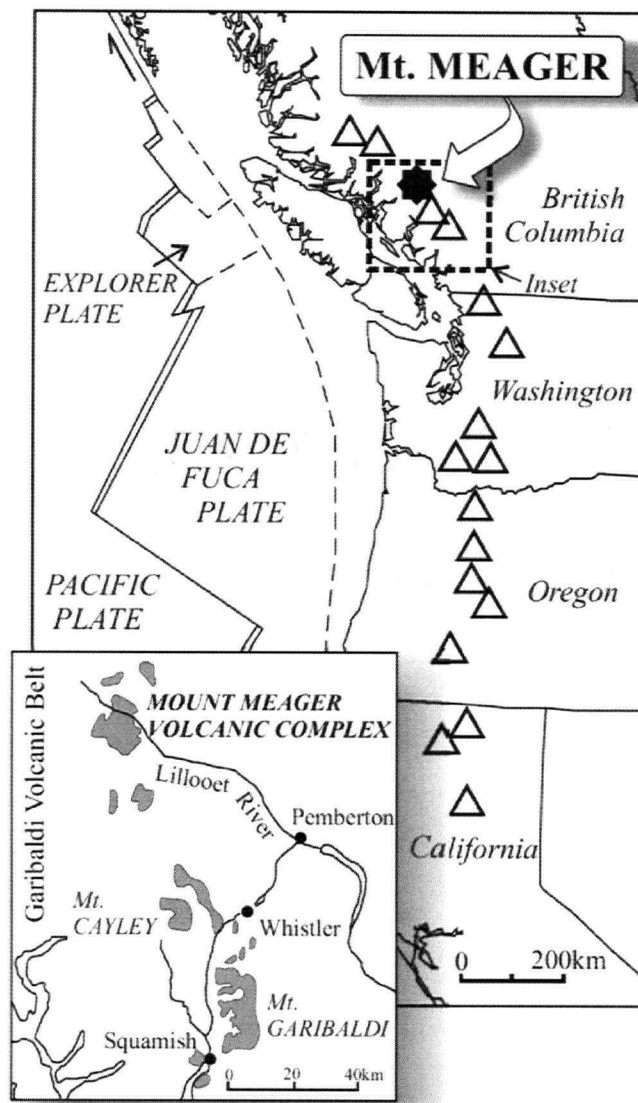
Figure 1: Location of the Mount Meager (star) within the Canadian portion of the Cascade volcanic belt (modified from Stewart et al., 2003). Triangles represent major Quaternary volcanoes. Inset shows geographic location of the Mount Meager Volcanic Complex (MMVC).

CHAPTER TWO

GEOLOGICAL SETTING

2.1.   The 2360 BP Eruption of Mount Meager and the Pebble Creek Formation

The Mount Meager Volcanic Complex (MMVC) is a component of the Garibaldi Volcanic Belt,

which is the northernmost segment of the Cascade Volcanic Belt (Fig. 1; Mathews, 1958; Green

et al., 1988; Read, 1990; Sherrod and Smith, 1990; Kelman et al., 2002; Clague et al., 2003;

Green and Sinha, 2005). Mount Meager is a composite stratovolcano located approximately 50

km northwest of Pemberton in the Coast Mountains, and rises to an elevation of 2645 m between

the Lillooet River and Meager Creek (Stasiuk et al., 1996). Volcanism associated with the

MMVC ranges from 2.2 Ma (K-Ar) to its most recent eruption at 2360 BP (Nasmith et al., 1967;

Read, 1977; Read, 1978; Clague et al., 1995). The edifice drapes over southern Coast Belt rocks

including Mesozoic metamorphic supracrustal rocks of the Cadwallader Formation, and Tertiary

monzonite intrusions of the Coast Plutonic Complex (Read, 1978; Gabrielse et al., 1992).

The vent for the 2360 BP eruption cuts through deposits of the preceding Plinth Assemblage (90

– 100 Ka; Read, 1978) and is situated at 1500 m elevation, roughly 1000 m above the present

stream bed of the Lillooet River (Stasiuk et al., 1996). The 2360 BP eruption (Nasmith et al.,

1967; Clague et al., 1995) produced the sequence of volcaniclastic dacite-rhyodacite deposits of

the Pebble Creek Formation (Fig. 2a; Read, 1978; Hickson et al., 1999; Stewart, 2002; Stewart et

al., 2003). The Pebble Creek Formation records an initial sub-Plinian eruption that produced a

pumice fall deposit and an ignimbrite, followed by emplacement of block and ash flow deposits,

the Keyhole Falls Member (here defined). The eruption cycle ended with the extrusion of a

rhyodacite lava (Stasiuk et al., 1996; Hickson et al., 1999; Stewart, 2002). There was no appreciable lapse in time during this sequence of events.

The MMVC region was originally mapped by Anderson (1975), and Read (1977, 1978, 1990); however, a more detailed mapping of the Pebble Creek Formation recognizing the presence and distributions of pyroclastic flow and block and ash flow deposits was completed by Stasiuk et al. (1996), Hickson et al. (1999), and Stewart (2002). Figure 2b is a simplified geological map from Stewart (2002) showing the distribution of the Pebble Creek Formation volcanic deposits resulting from the 2360 BP eruption.

2.2. The Keyhole Falls Member

The Keyhole Falls Member is chiefly confined to a steep-sided paleo-channel inferred to be a glacially-steepened, earlier incarnation of the Lillooet River (Stasiuk et al., 1996; Hickson et al., 1999). It is approximately 165 m thick immediately below the inferred vent at the type locality of Keyhole Falls (466400E 5614050N; Figs. 2a, 3). The Member is a wedge-shaped unit with an estimated volume of 0.44 km^3 (Stewart, 2002) that thins downstream to a total thickness of 25 m after 2.5 km.
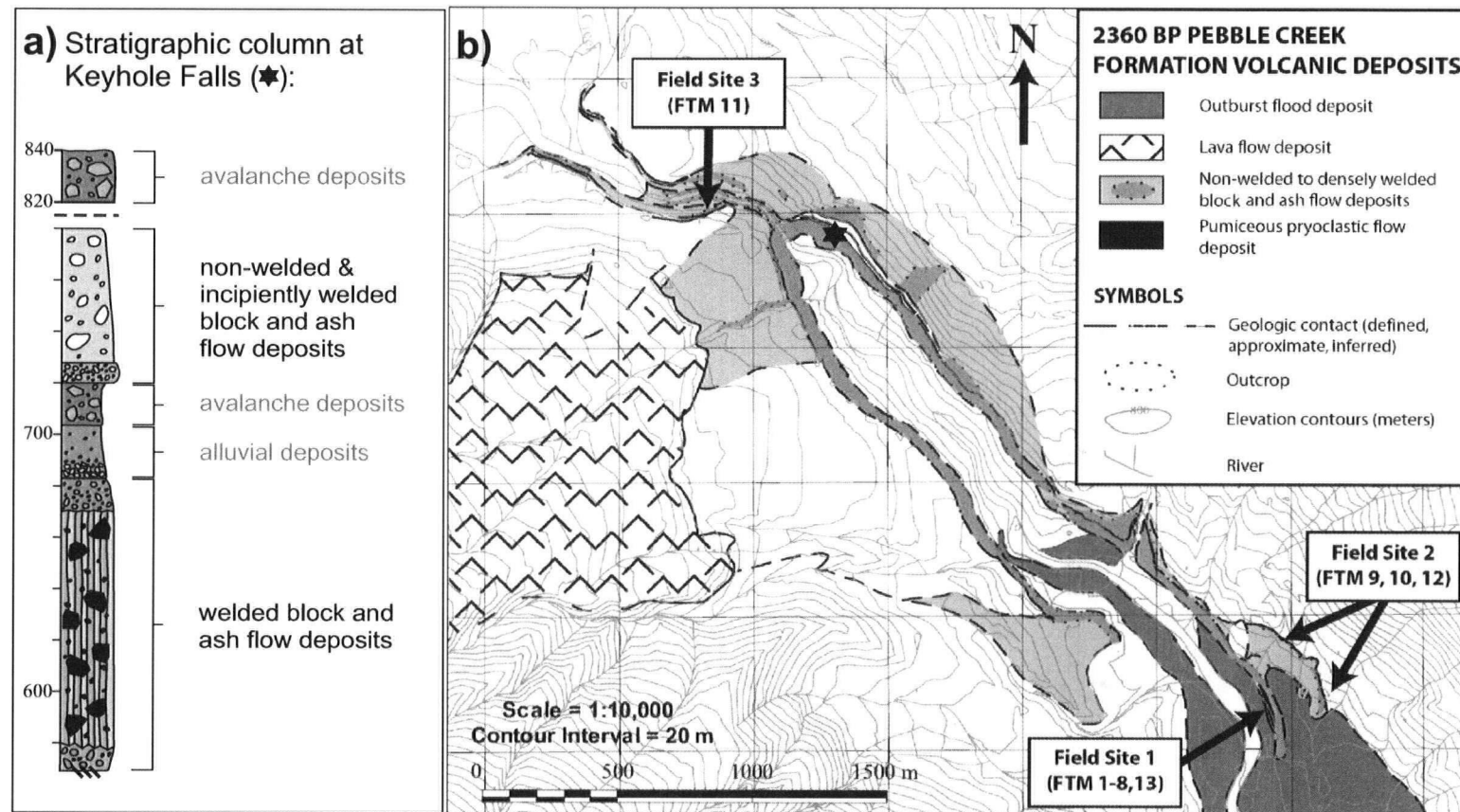
Figure 2: Stratigraphy and geology of the Pebble Creek Formation modified from Stewart (2002): **(a)** stratigraphic column for type locality Keyhole Falls (✱), non-volcanic deposits labeled in grey; **(b)** simplified geological map showing the variably welded block and ash flow deposits (light – medium grey), the rhyodacite lava flow deposit (patterned), the outburst flood deposit (dark grey), and the pumiceous pyroclastic flow deposits (black). Field sites and corresponding Field Texture Maps (FTMs) are indicated with arrows.
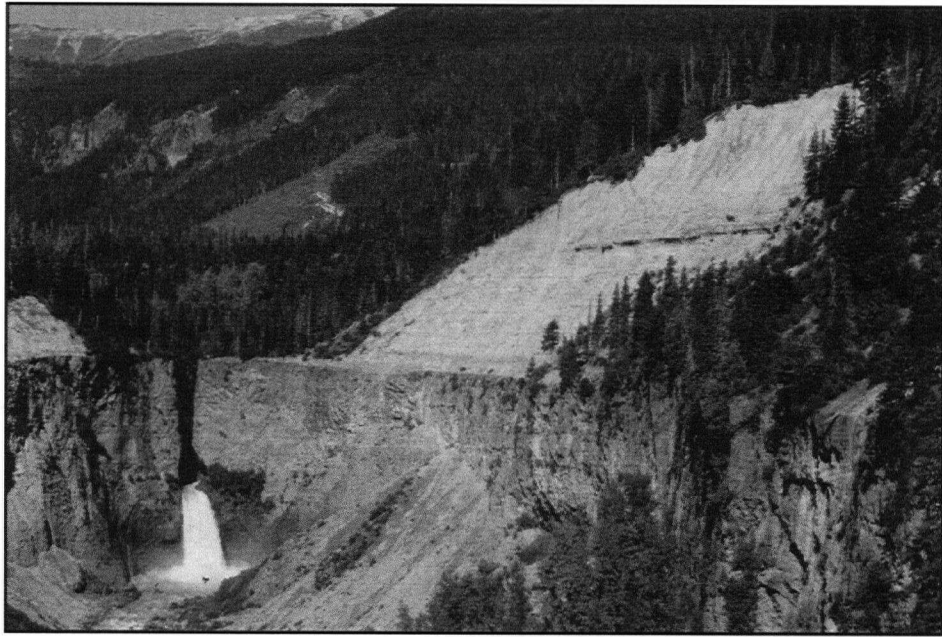
Figure 3: Northwest-facing field photograph showing block and ash pyroclastic flow deposits exposed at Keyhole Falls in the Lillooet River Valley. The lower cliff-forming unit comprises the densely welded facies and is approximately 100 m thick at this location. The upper recessive units (here, approximately 60 m) are bedded and variably sorted, comprising interbedded fluvial gravels and non-welded to incipiently welded block and ash flow deposits. The section is capped by younger rock avalanche deposits. The present-day canyon was formed by an outburst flood event shortly after deposition (Hickson et al., 1999; Stewart, 2002). The gorge in the cliff wall results from 2360 years of erosion by the Lillooet River through the residual welded block and ash flow deposit.

The Keyhole Falls Member is a dominantly monomict volcaniclastic breccia composed of centimeter- to metre-sized crystal-rich, rhyodacite obsidian clasts supported by a pumiceous ash-sized matrix. Accidental, centimetre-sized angular lithic clasts of monzonite, Plinth assemblage, and shale are uncommon. The Member is dominantly massive and very poorly sorted. Cryptic reversely graded bedding is exhibited in the densely welded material by variations in the apparent maximum clast size. Detailed petrographic and geochemical studies of the deposit can be found in Stasiuk et al. (1996) and Stewart (2002). The Member is inferred to be a block and ash flow deposit because it exhibits: (1) very poor sorting; (2) mostly monolithic clasts of rhyodacite lava; (3) an ash-rich matrix; and (4) cooling joints throughout the densely welded facies, indicating a hot emplacement (Stasiuk et al., 1996; Stewart 2002). These characteristics parallel those of block and ash flow deposits reported from other classic examples (e.g., Merapi, Unzen, Montserrat; Cas and Wright, 1987).

2.3.   Facies Variations

Variations in welding intensity are noted in several areas along the Lillooet River Valley, from non-welded and incipiently welded (Streck and Grunder, 1995) deposits that form a significant slope, to a lower, densely welded deposit that forms a prominent steep-sided gorge (Fig. 3). On the basis of welding intensity, I identify four separate welding facies in the Keyhole Falls Member (Fig. 4): (1) a basal non-welded facies; (2) a densely welded facies at, and up to 3.15 km downstream from Keyhole Falls; (3) an oxidized and incipiently welded facies greater than 3.15 km downstream from Keyhole Falls; and (4) an upper non-welded facies.
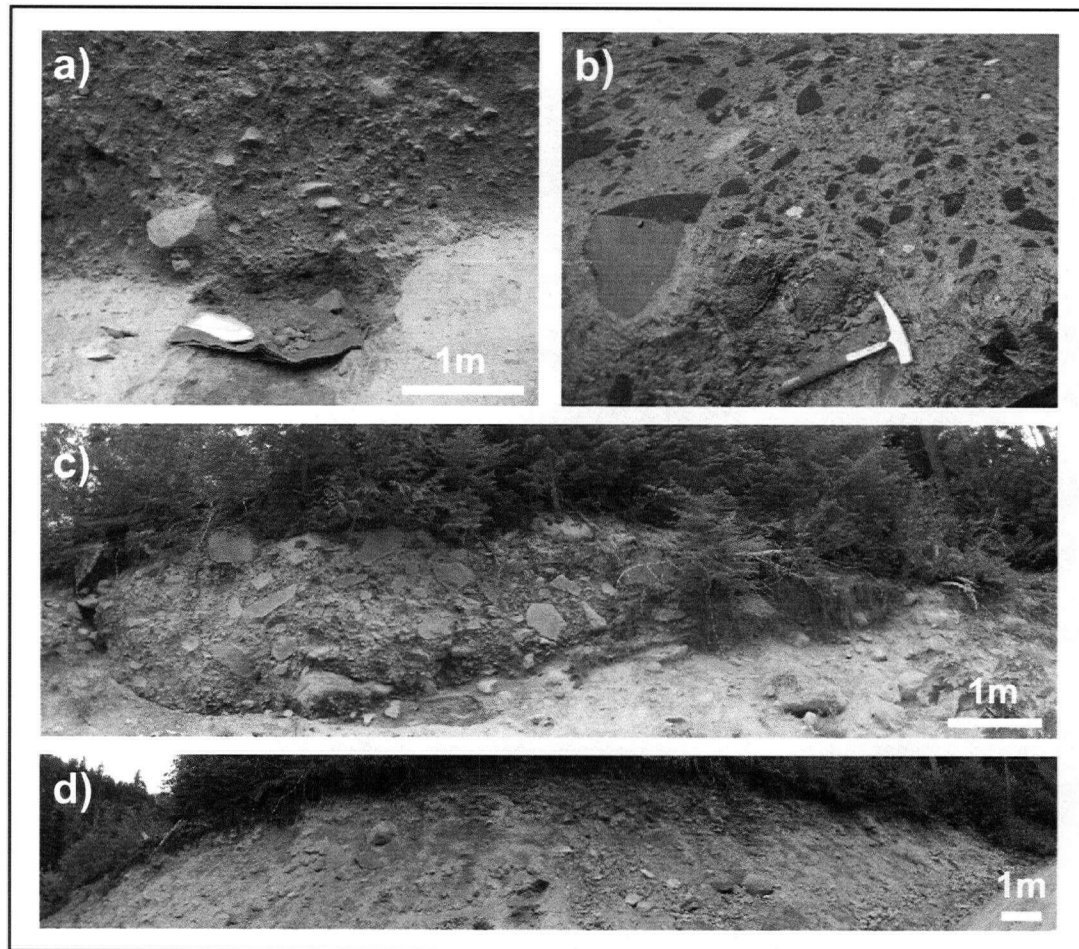
Figure 4: Field photographs showing the facies variations within the block and ash flow deposit: **(a)** basal, non-welded facies (Field Site 1, Fig. 2); **(b)** densely welded facies (Field Site 1, Fig. 2); **(c)** incipiently welded facies (oxidized) from the upper part of the succession (Field Site 2, Fig. 3); and, **(d)** non-welded facies (non-oxidized) from the upper part of the succession (Field Site 3, Fig. 2).

The basal non-welded facies (type locality Field Site 1; Table 1) is an approximately 2 m thick, non-welded and poorly-sorted volcaniclastic breccia supported by a grey, ash-sized matrix (Fig. 4a). Juvenile clasts are dominantly pumice (45 – 55%) and moderately dense rhyodacite (40 – 50%), with sporadic dense rhyodacite clasts (2 – 5%); rare accidental clasts of Plinth assemblage and Tertiary monzonite country rock are present as well as flow banded pumice-like clasts. Clasts are mostly sub-angular to sub-rounded, typically 5 – 15 cm in diameter, and rarely up to 1 m. The base is not exposed, but this facies is inferred to sit conformably on a deposit of pumiceous pyroclastic flow, and to grade upwards into the densely welded facies.

The densely welded facies (type locality Field Site 1, Table 1) is a 16 m thick, poorly-sorted volcaniclastic breccia supported by a grey, fine ash-sized matrix (Fig. 4b). Juvenile, angular to sub-rounded, vesicular and glassy rhyodacite clasts dominate (85 – 95%), with lesser quantities of accidental Plinth assemblage, granodiorite, monzonite and shale clasts present. Clasts are typically 5 – 15 cm in diameter, with local clasts up to 1 m across. Some clasts show vestiges of flow banding textures. Many obsidian clasts are demonstrably pyroclastic in nature, and define a prominent sub-horizontal fabric similar to eutaxitic fabrics observed in welded ignimbrites (e.g., Smith, 1960b). Columnar joints are continuous throughout the thickness of the densely welded facies, suggesting that it represents a single cooling unit (*sensu* Smith, 1960b).

Table 1. Location and description of field sites, including associated field texture maps (FTMs) and slab texture maps (STMs).

Field Site	Description	UTM Coordinates		Block and Ash Flow Deposit Facies	Field Texture Map	Slab Texture Map
		Easting	Northing			
1	Valley wall exposure in Lillooet River valley; cliff and fallen blocks	468404	5612192	Densely welded (middle of deposit)	01	16
					02	11
						12
						13
						14
						15
					03	-
					04	01
						02
					05	07
						08
						09
						10
					06	03
						04
						05
						06
				Unwelded (base of deposit)	07	-
					08	-
					13	-
2	Roadcut exposure ~300m NE of Field Site 1	468531	5612414	Incipiently welded (upper oxidized section)	09	-
					10	-
					12	-
3	Roadcut exposure; on south side of bridge at Keyhole Falls	466400	5614050	Unwelded (upper unoxidized section)	11	-

The incipiently welded facies (type locality Field Site 2; Table 1) is an approximately 5 m thick, poorly-sorted volcaniclastic breccia supported by an oxidized, orange-brown matrix of ash-sized particles and clast fragments (Fig. 4c). It contains sub-angular to sub-rounded juvenile clasts which vary in from pumice-like (70 – 95%) to dense and glassy (5 – 30%); observed lithics include rare Plinth assemblage and monzonite clasts. Some juvenile clasts display flow banded or bread-crust textures, and locally exhibit long-axis alignment. Clasts average 5 – 15 cm in diameter, with rare clasts up to 1.5 m.

The upper non-welded facies (type locality Field Site 3; Table 1) is an approximately 5 m thick, poorly-sorted volcaniclastic breccia supported by a grey-brown matrix of ash-sized particles and clast fragments (Fig. 4d). Juvenile clasts (85 – 90%) are typically sub-angular to sub-rounded and variably dense (pumice to glassy); accidental lithic clasts of the Plinth assemblage are also present (5 – 10%), with minor amounts of intrusive igneous and metamorphic clasts (1 – 2%). Clasts average 5 – 15 cm in diameter, with local clasts up to 50 cm. Unlike the basal non-welded facies, no fabric or clast orientation is observed.

2.4.   Emplacement History

The distribution of welded facies within the block and ash flow deposit is an indication of their formation and depositional processes. The block and ash flow deposits resulted from continued effusion of block and ash flows from rhyodacite lava flows or domes (Stasiuk et al., 1996; Hickson et al., 1999; Stewart, 2002). Although the eruption was not observed, eruption analogues may include Monserrat, where block and ash flows are produced by Vulcanian

13

eruption-triggered explosive dome collapse (Cole et al., 2002; Woods et al., 2002; Formenti and Druitt, 2003); Merapi, where block and ash flows commonly result from the gravitational collapse of domes or lava flows (Bardintzeff, 1984; Boudon et al., 1993; Abdurachman et al., 2000.); or Unzen, where they can result from the exogenous or endogenous growth of domes (Sato et al., 1992; Ui et al., 1999; Miyabuchi, 1999). The flows then traveled down the steep slopes of the volcanic edifice and were captured and entrained by the paleo-Lillooet river valley. Continuously erupting over time, these flows accumulated in the valley, spreading downstream, increasing in thickness, and welding together. Regardless of how the block and ash flows were initiated (explosive vs. gravitational collapse), the welding was facilitated by the fact that the block and ash flows were contained within a steep, narrow, and mountainous drainage system. The pyroclastic flows must also have accumulated relatively rapidly to have retained heat and not entrained air as they traveled down the Lillooet River valley. The welding process was sufficiently intense that it transformed a significant portion of the originally unconsolidated material into a mass of dense, competent vitrophyre.

Shortly after this phase of eruption began, the block and ash flow deposits proceeded to disrupt the Lillooet River drainage and cause the river to dam upstream of Keyhole Falls. The thickness and welded character of the pyroclastic deposits then caused the Lillooet River to back up and form a lake upstream of Keyhole Falls (Read, 1990; Stasiuk et al., 1996; Hickson, 1999; Stewart, 2002; Stewart et al., 2003). The block and ash flow deposit withheld its heat while a lake began to form behind it that was substantial enough to accumulate alluvial sediments (Cordy, 1999; Schipper, 2002; Stewart, 2002). The pyroclastic dam was maintained throughout the entire eruption until the lake built up to a level that overtopped the densely welded section. Once the

lake reached this critical level, the dam failed catastrophically (possibly in two stages) and the welded block and ash flow deposit was disrupted again by outburst flood events (Stewart, 2002). These deluge events excavated a large canyon (Fig. 3) exposing up to 100 m of densely welded vitrophyric breccia. Radial cooling joints are pervasive throughout the multitude of blocks found in the outburst flood deposit, indicating the block and ash flow was still hot when it fragmented for the second time (Hickson, 1999). In an effort to return to its original state, the Lillooet River has cut down through the block and ash flow deposit over the past 2400 years.

In the following sections, I use a combination of detailed texture mapping, image analysis, and physical property measurements to quantify welding intensity within the various facies of the Keyhole Falls Member. These properties are used to document how welding of this deposit was accommodated. The variations in these properties provide estimates of volume strain and pure shear strain incurred by the welded block and ash flow deposits.

CHAPTER THREE

FABRIC ANALYSIS

Fabric analysis has previously been used to measure welding intensity in volcanic deposits (e.g. Ragan and Sheridan, 1972; Sheridan and Ragan, 1976; Ui et al., 1989; Boudon et al., 1993; Karatson et al., 2002; Quane and Russell, 2006), and thereby allow estimates of strain and rheology to be made. We employ two methods of fabric analysis to constrain the intensity of welding in the Keyhole Falls Member: (1) textural analysis undertaken on small-scale maps drawn in the field; and (2) textural analysis of fabrics observed in polished slabs of the densely welded facies.

3.1. Textural Data

I have employed textural mapping to describe and quantify the change in fabric and flattening of particles within the Keyhole Falls Member. This was conducted at two scales: (1) on 1 m^2 textural maps produced in the field; and (2) on polished slabs of the densely welded facies. By using these mapping methods in conjunction with image analysis software (Scion Image™, Image J™), the amount and type(s) of strain accumulated within the deposit can be constrained quantitatively, and the partitioning of strain between the clasts and matrix can be determined.

3.1.1. Field Texture Maps (FTMs)

Field texture maps were created by placing a 1 m^2 grid flush with the outcrop and then mapping the distribution, size, and shapes of all the clasts appearing in the designated area (Fig. 5a). Mapping involved a hand-drawn reproduction of each clast within the 1m^2 area, using the 10 cm^2 squares as a reference grid (Fig. 5b). All particles greater than 0.5 cm were identified as clasts, and the size fraction below this was treated as matrix. A total of thirteen FTMs were completed; twelve drawn perpendicular to bedding (non-welded facies) or foliation (welded facies), and one drawn on the foliation surface to gain a three-dimensional perspective. FTMs were drawn at a scale of 1:5 and a field photograph of the grid overlying the outcrop was taken for reference. The texture maps derive from individual outcrops at the three field sites (Fig. 2b; Table 1) and were selected to capture the full range of welding intensity within the Keyhole Falls Member. They were then retraced by hand, scanned (Fig. 5c) and imported into Scion Image™ and Image J™ for image analysis, where the specific dimensions, proportions and orientations of the clasts were determined (Fig. 5d). Output images from Scion Image™ are shown in Figure 6. For detailed descriptions and for a full suite of images depicting image analysis procedures for FTMs, refer to Appendices A and B, respectively.
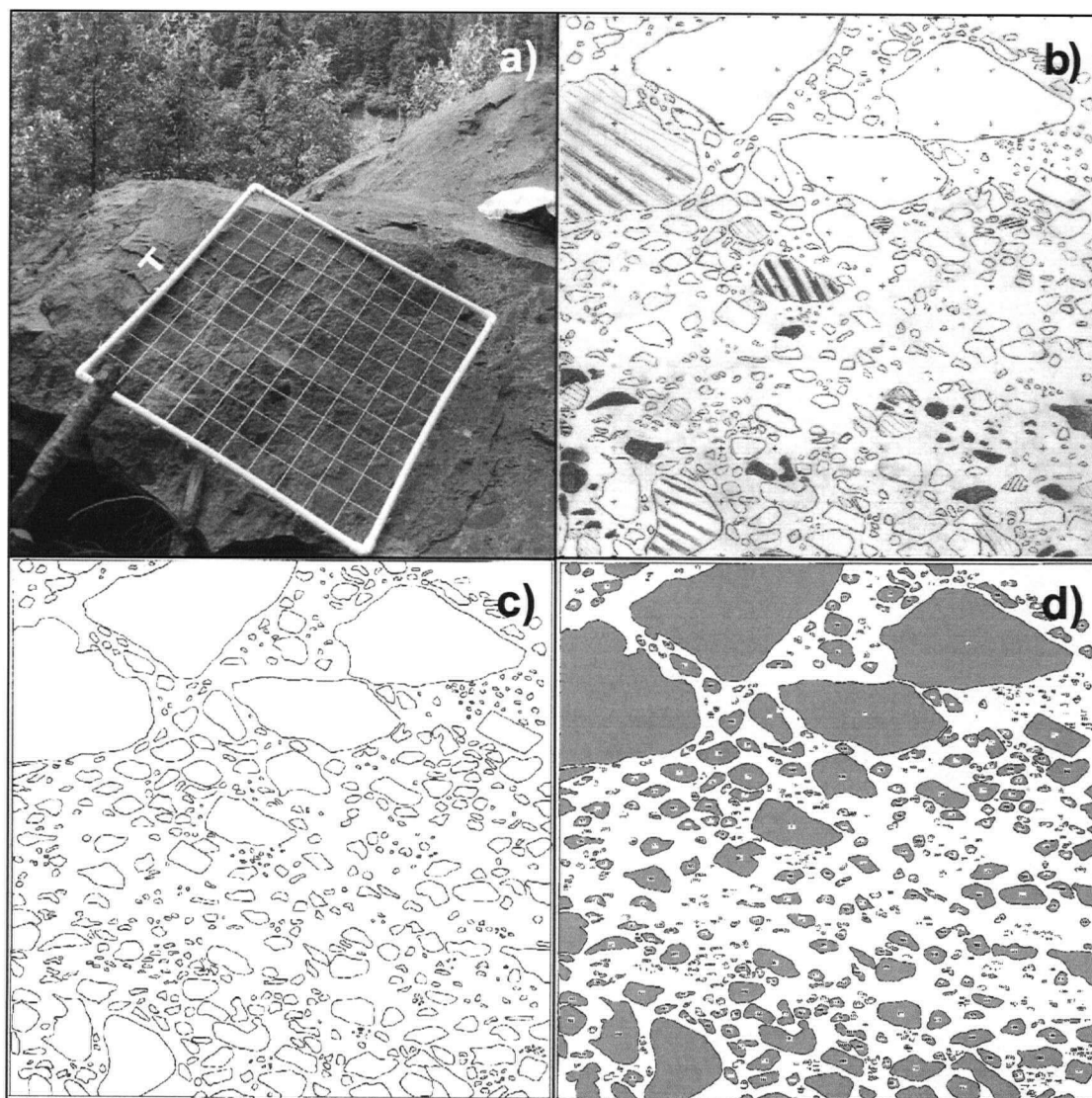
Figure 5: Procedure used for image analysis of field texture maps using FTM 01 as an example: **(a)** field photo of 1m x 1m grid on an outcrop of densely welded block and ash flow deposit (T denotes top of grid); **(b)** hand-drawn field texture map based on a minimum clast size of 0.5 cm; **(c)** digital scanned version FTM 01 used for image analysis (Scion Image™ or Image J™); **(d)** preliminary results of image analysis showing individual numbered clasts.

18
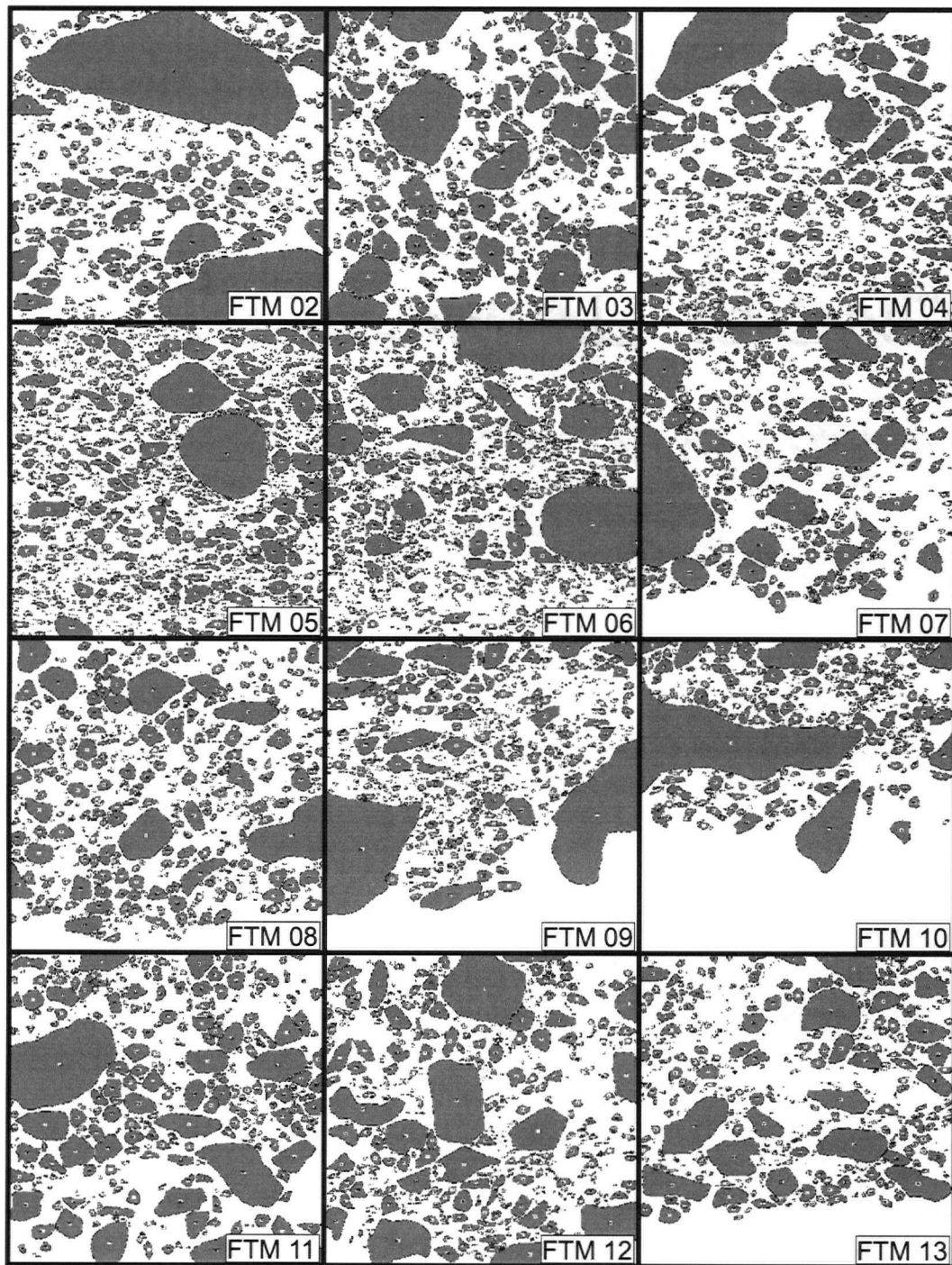
Figure 6: Results of image analysis for the twelve other FTMs, selected to represent the full range of welding intensity. Numbers of FTMs indicate the chronological order in which the field mapping was completed (e.g., not welding intensity).
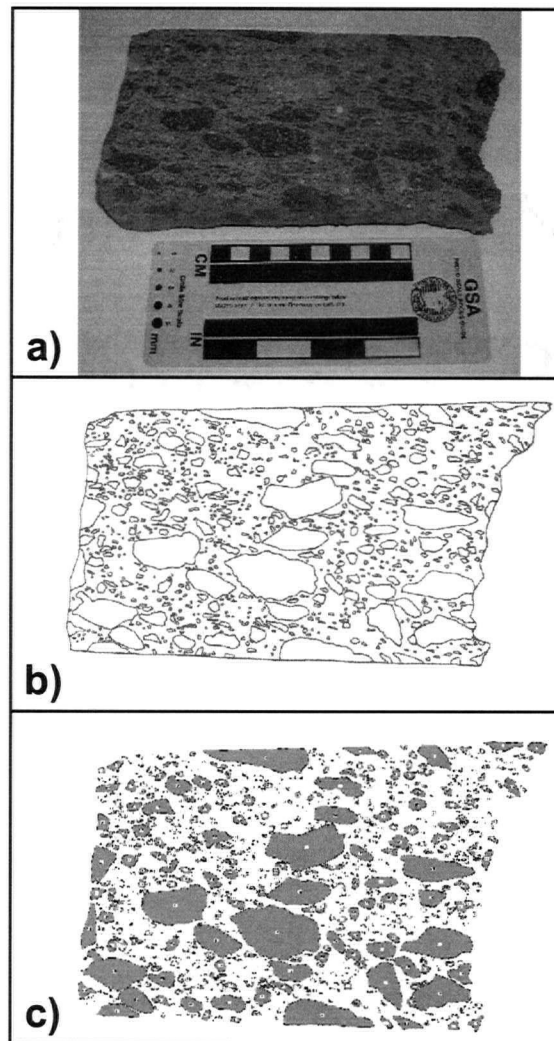
Figure 7: Graphical summary of procedures used for image analysis of slab texture maps, using STM 01 as an example: **(a)** hand sample photo of a slab (KM-05-011, side 1/1) of densely welded block and ash flow deposit; **(b)** digital scanned version of hand-drawn STM 01 used for image analysis (Scion Image™ or Image J™), where the minimum clast size is 0.5 mm; **(c)** preliminary results of image analysis showing individual numbered clasts.

3.1.2. Slab Texture Maps (STMs)

Sixteen slab texture maps were created from the densely welded block and ash flow deposits. This was accomplished by placing a sheet of acetate over the slab (Fig. 7a), and tracing clasts 0.5 mm or greater by hand; particles less than 0.5 mm were treated as matrix. STMs are drawn perpendicular to foliation, at a scale of 1:1 (Fig. 7b). These texture maps correspond to samples derived from five different FTMs (Table 1). The acetates were then retraced by hand, scanned into digital form (Fig. 7c), and imported into Scion Image™ and Image J™ for image analysis in the same manner as the FTMs (Fig. 7d). Resulting output images from Scion Image are displayed in Figure 8. For a full suite of images depicting image analysis procedures, refer to Appendix C.
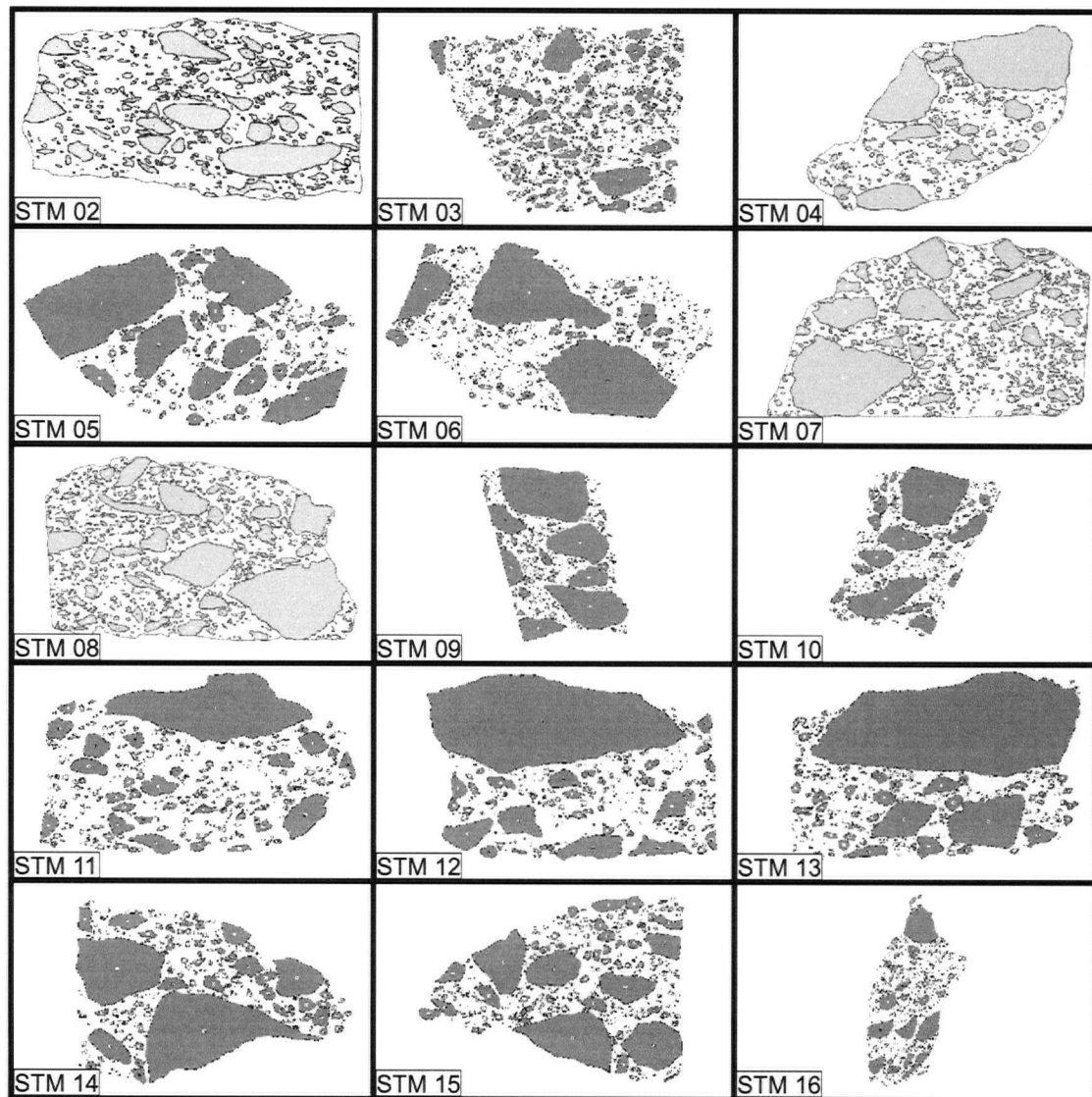
Figure 8: Results of image analysis for the fifteen other STMs, representing the heterogeneity of welding intensity in the block and ash flow deposit. Numbers indicate the chronological order in which the slab texture maps were completed (e.g., not welding intensity).

22

3.2. Image Analysis

Image analysis software was used to quantify the FTMs and STMs: Scion Image™ returned values of clast area, perimeter, minimum and maximum diameter, and orientation, whereas Image J™ calculated the proportions of clasts and matrix for both the FTMs and STMs (Tables 2 and 3, respectively). Clast-matrix ratios for the FTMs are almost constant, averaging $51 \pm 5\%$ and ranging between $43 - 59\%$ (Fig. 9a). Clast-matrix proportions for the STMs are more variable; clasts average $53 \pm 9\%$, and range from $39 - 69\%$ (Fig. 9b).

Grain size distributions were created using individual clast areas calculated with Scion Image™. FTMs show normal or near-normal distributions that are variably skewed towards smaller size fractions because the FTM data is truncated below 0.1 cm^2, corresponding to a minimum clast diameter of ~0.5 cm (Fig. 10). Distributions of the STMs show a sharp decrease from the smallest clast size fraction to the largest because size fractions are similarly truncated below 0.01 cm^2 due to a minimum clast diameter of 0.5 mm (Fig. 11). Neither the FTMs nor the STMs demonstrate any appreciable shift in grain size distribution with welding intensity. Cumulative grain size distributions were also created for the FTMs (Fig. 12a) and STMs (Fig. 12b); however, welding facies in the FTMs and blocks of densely welded material in the STMs are indistinguishable from one another based on their cumulative grain size distribution curves.

Table 2. Summary of properties of block and ash flow deposits derived from image analysis of FTMs, including: total map area (A_T), clast area (A), clast perimeter (P), ratio of area to perimeter (A/P), minimum (c) and maximum (a) clast dimensions, ratio of maximum to minimum clast radius (a/c), clast orientation, volume strain (ε_V), pure shear strain (ε_S), and % of clasts (C) and matrix (M) by area.

FTM	A_T (m²)	N[1]		A (cm²)	P (cm)	A/P	a (cm)	c (cm)	a/c	Orientation (°)	ε_V[2]	ε_S[3]	C (%)	M (%)
1	1.00	563	avg.	5.68	7.56	0.41	1.37	0.72	1.91	23.6	0.42	0.31		
			max	440.5	94.0	4.69	16.2	8.68	6.52	89.8	0.85	0.71	47	53
			min	0.14	1.44	0.06	0.28	0.15	1.03	0.2	0.02	0.02		
2	0.98	386	avg.	12.1	9.04	0.49	1.62	0.88	1.84	26.2	0.40	0.30		
			max	2404.7	240.5	10.00	44.2	17.3	5.33	88.4	0.81	0.67	59	41
			min	0.23	1.77	0.13	0.29	0.22	1.04	0.0	0.04	0.02		
3	1.00	400	avg.	10.2	9.75	0.54	1.67	1.02	1.71	41.3	0.36	0.27		
			max	534.7	95.2	5.62	14.2	12.0	5.15	89.4	0.81	0.66	54	46
			min	0.22	1.71	0.12	0.29	0.19	1.02	0.4	0.02	0.01		
4	0.93	530	avg.	6.27	8.31	0.44	1.49	0.80	1.87	25.4	0.41	0.30		
			max	432.1	115.0	3.76	18.3	7.50	5.11	88.6	0.80	0.66	49	51
			min	0.22	1.79	0.11	0.31	0.21	1.01	0.1	0.01	0.01		
5	1.00	1064	avg.	4.19	6.42	0.35	1.18	0.62	1.90	21.7	0.41	0.31		
			max	592.7	94.1	6.30	14.6	13.0	5.91	90.0	0.83	0.69	47	53
			min	0.17	1.58	0.10	0.25	0.18	1.03	0.0	0.03	0.02		
6	1.00	883	avg.	3.57	6.51	0.35	1.19	0.62	1.98	25.0	0.43	0.32		
			max	190.0	60.9	3.15	11.4	6.05	13.2	89.9	0.92	0.82	52	48
			min	0.17	1.52	0.11	0.25	0.16	1.03	0.0	0.03	0.02		
7	0.88	487	avg.	5.95	7.60	0.45	1.31	0.84	1.57	34.1	0.32	0.23		
			max	166.9	64.3	2.84	10.9	5.84	4.96	89.8	0.80	0.66	46	54
			min	0.13	1.33	0.10	0.23	0.19	1.02	0.1	0.02	0.01		
8	0.93	571	avg.	6.24	7.85	0.48	1.36	0.89	1.55	31.3	0.32	0.23		
			max	194.9	55.4	3.58	10.3	6.55	4.95	89.8	0.80	0.66	45	55
			min	0.19	1.53	0.12	0.27	0.22	1.01	0.0	0.01	0.01		
9	0.79	613	avg.	4.22	6.61	0.37	1.19	0.66	1.74	26.7	0.38	0.28		
			max	149.0	57.2	2.72	10.5	4.58	4.82	90.0	0.79	0.65	56	44
			min	0.15	1.59	0.06	0.27	0.16	1.01	0.0	0.01	0.01		
10	0.60	340	avg.	5.52	7.90	0.45	1.40	0.81	1.74	29.3	0.37	0.27		
			max	337.1	84.5	3.99	14.9	7.19	4.70	89.0	0.79	0.64	59	41
			min	0.23	1.80	0.13	0.28	0.26	1.02	0.1	0.02	0.01		
11	1.00	370	avg.	10.3	10.1	0.58	1.74	1.09	1.62	35.9	0.33	0.24		
			max	332.9	81.1	4.10	14.5	7.31	4.84	88.1	0.79	0.65	51	49
			min	0.23	1.77	0.13	0.29	0.22	1.02	0.5	0.02	0.01		
12	0.91	505	avg.	7.28	8.22	0.45	1.46	0.82	1.79	28.3	0.39	0.29		
			max	396.4	81.2	4.88	13.9	9.09	7.80	89.9	0.87	0.75	52	48
			min	0.14	1.35	0.10	0.24	0.19	1.03	0.0	0.03	0.02		
13	0.76	436	avg.	6.83	7.78	0.45	1.37	0.82	1.66	31.6	0.35	0.26		
			max	212.2	64.1	3.31	12.3	6.34	3.49	90.0	0.71	0.57	43	57
			min	0.17	1.47	0.05	0.26	0.21	1.01	0.1	0.01	0.01		

[1] N = number of particles; [2] ε_V = volume strain estimated from oblateness (1-c/a); [3] ε_S = pure shear strain estimated from oblateness (1-c/a$^{2/3}$)

Table 3. Average properties of the block and ash flow deposits based on image analysis of STMs, including: total map area (A), clast area (A), clast perimeter (P), ratio of area to perimeter (A/P), minimum (c) and maximum (a) clast dimensions, ratio of maximum to minimum clast dimensions (a/c), clast orientation, volume strain (ϵ_V), pure shear strain (ϵ_S), and % of clasts (C) and matrix (M) by area. Standard deviations (1σ) are shown where appropriate.

STM	A_T(cm²)	N[1]	A (cm²)	σ (cm²)	P (cm)	A/P	a (cm)	σ (cm)	c (cm)	σ (cm)	a/c	Orientation (°)	σ (°)	ϵ_V[4]	ϵ_S[5]	C (%)	M (%)
1	175.8	838	0.08	0.322	116.40	0.05	0.16	0.176	0.08	0.076	1.91	22.77	21.147	0.41	0.30	44	56
2	133.7	399	0.11	0.477	111.61	0.06	0.20	0.228	0.10	0.079	1.98	21.34	18.338	0.43	0.32	39	61
3	124.4	598	0.07	0.254	112.04	0.05	0.16	0.142	0.09	0.070	1.73	28.58	23.716	0.37	0.27	40	60
4	113.5	305	0.07	0.208	116.45	0.05	0.15	0.143	0.09	0.066	1.79	26.66	23.164	0.38	0.28	54	46
5	106.4	181	0.14	0.470	106.17	0.06	0.19	0.212	0.11	0.108	1.67	32.32	22.956	0.35	0.26	58	42
6	147.0	468	0.04	0.079	129.77	0.04	0.12	0.085	0.07	0.042	1.75	31.19	22.584	0.37	0.27	52	48
7	157.7	634	0.07	0.324	112.53	0.05	0.15	0.156	0.08	0.071	1.71	27.03	21.897	0.36	0.27	49	51
8	159.0	653	0.08	0.358	114.73	0.05	0.15	0.166	0.09	0.077	1.72	25.76	21.967	0.37	0.27	51	49
9	111.5	289	0.09	0.642	118.34	0.04	0.13	0.178	0.08	0.097	1.73	35.98	25.315	0.37	0.27	68	32
10	113.3	340	0.11	0.699	114.28	0.05	0.15	0.238	0.08	0.096	1.77	31.23	23.746	0.37	0.27	56	44
11	108.1	304	0.07	0.152	105.23	0.05	0.16	0.119	0.09	0.067	1.90	25.60	22.463	0.41	0.31	45	55
12	113.9	234	0.06	0.213	107.23	0.05	0.14	0.124	0.09	0.072	1.70	30.38	24.104	0.36	0.26	61	39
13	122.7	284	0.09	0.564	114.52	0.05	0.15	0.177	0.08	0.103	1.85	28.33	23.633	0.39	0.29	69	31
14	88.7	226	0.08	0.196	108.67	0.05	0.16	0.143	0.10	0.074	1.71	32.75	26.046	0.36	0.27	62	38
15	78.3	288	0.07	0.279	120.79	0.05	0.15	0.140	0.08	0.071	1.81	34.37	25.325	0.38	0.28	55	45
16	124.5	590	0.06	0.254	119.79	0.04	0.14	0.149	0.07	0.070	1.94	32.83	22.535	0.41	0.31	44	56

[1]N = number of particles; [2]ϵ_V = volume strain estimated from oblateness (1-c/a); [3]ϵ_S = pure shear strain estimated from oblateness (1-c/a²ᐟ³)
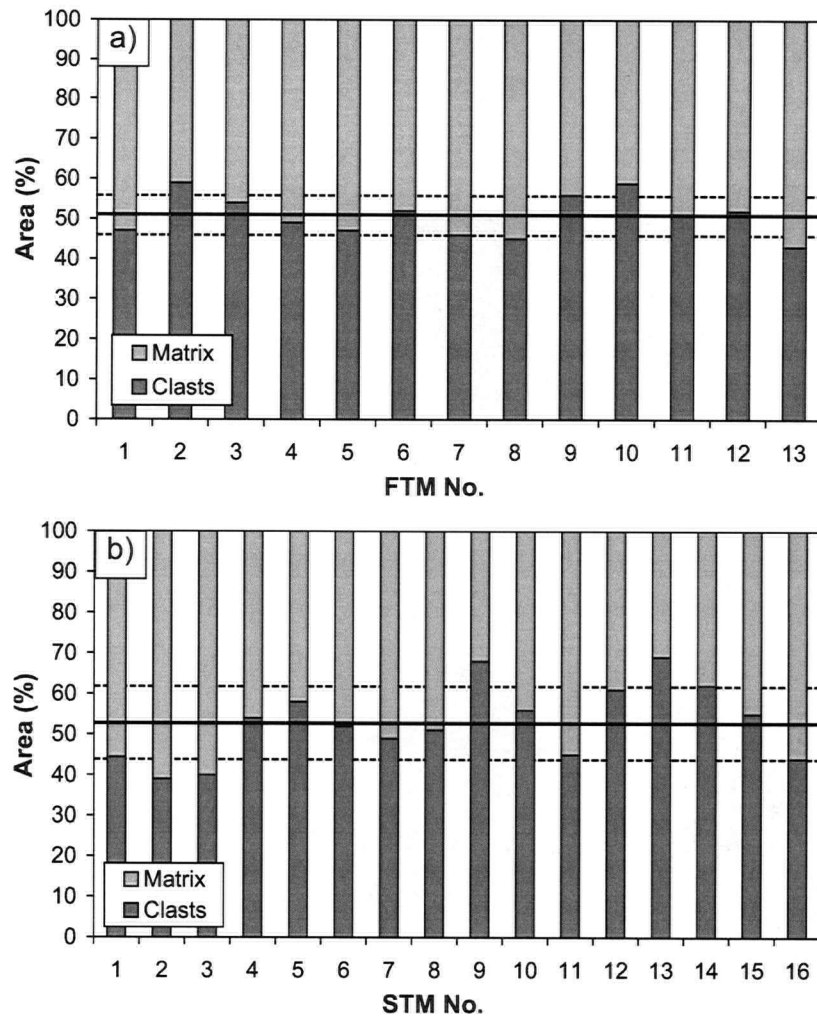
Figure 9: Proportions of clasts and matrix based on cross-sectional area, for: **(a)** FTMs, and **(b)** slab texture maps (STMs). The average proportion of clasts (>0.5 cm) in the FTMs is 51 ± 5%. Clasts never represent more than 60% of the total field texture map area. The average proportion of clasts (>0.5 mm) in the STMs is 53 ± 9%, but vary from 39-69%.

26
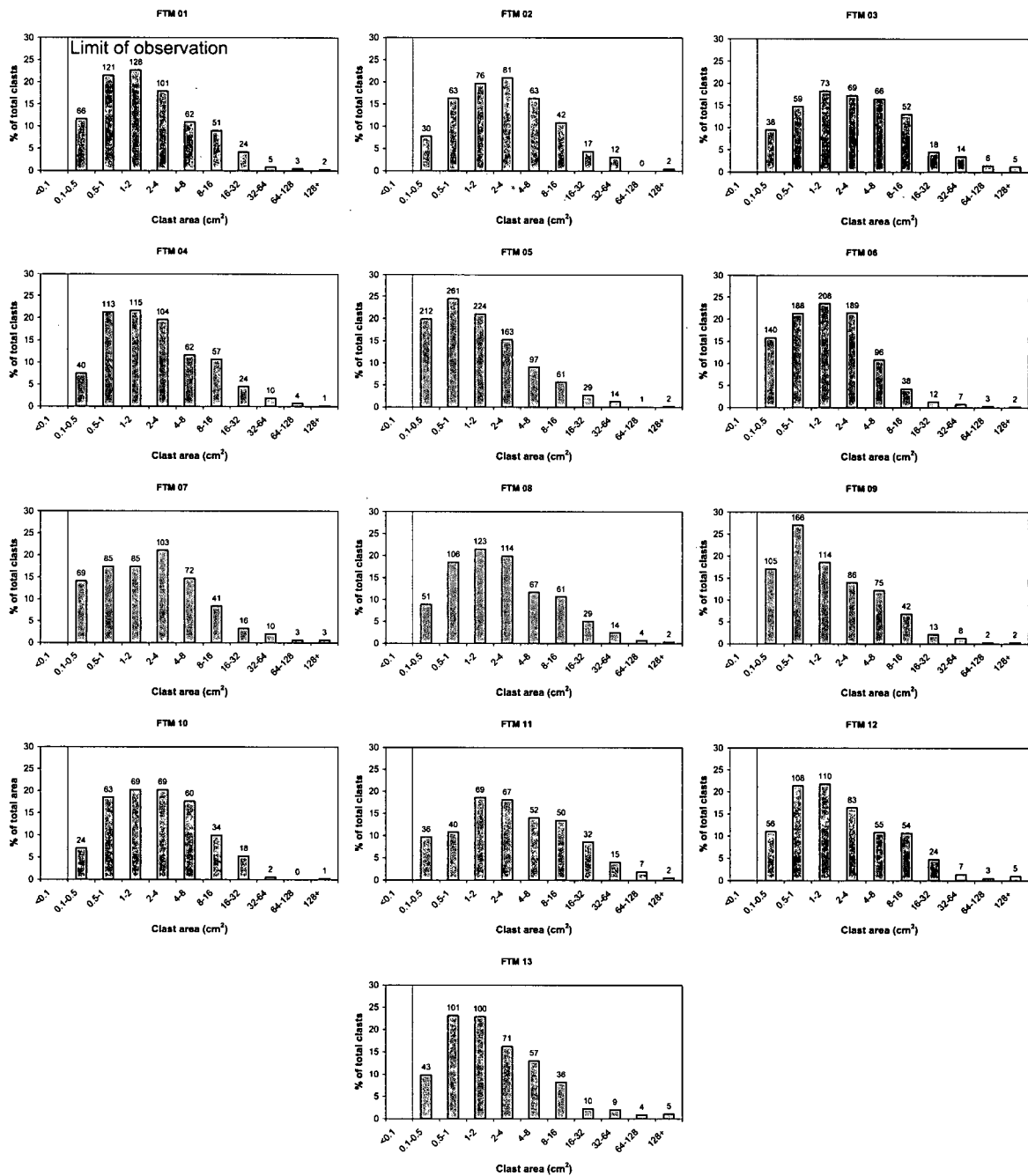
Figure 10: FTM grain size distribution by clast area as calculated by image analysis. The distribution is truncated below 0.1 cm^2 due to the scale limitations of the field texture map (i.e. minimum clast diameter = 0.5 cm). Note that there is no significant shift in dominant grain size with welding intensity.
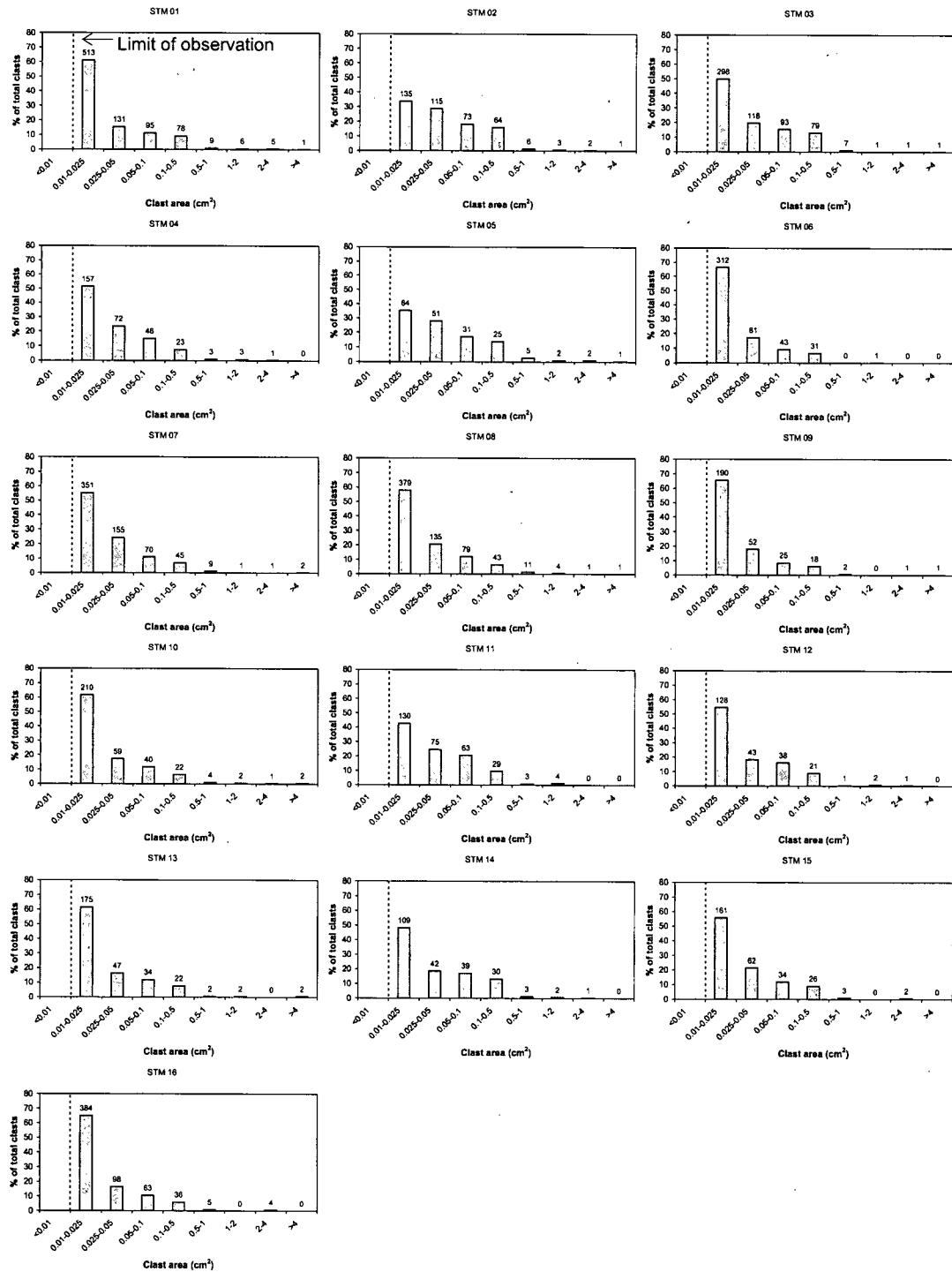
Figure 11: STM grain size distribution by clast area as calculated by image analysis. The distribution is truncated below $0.01 cm^2$ due to the scale limitations of the field texture map (i.e., minimum clast diameter = 0.5 mm). Note that there is no significant shift in dominant grain size with welding intensity.

28
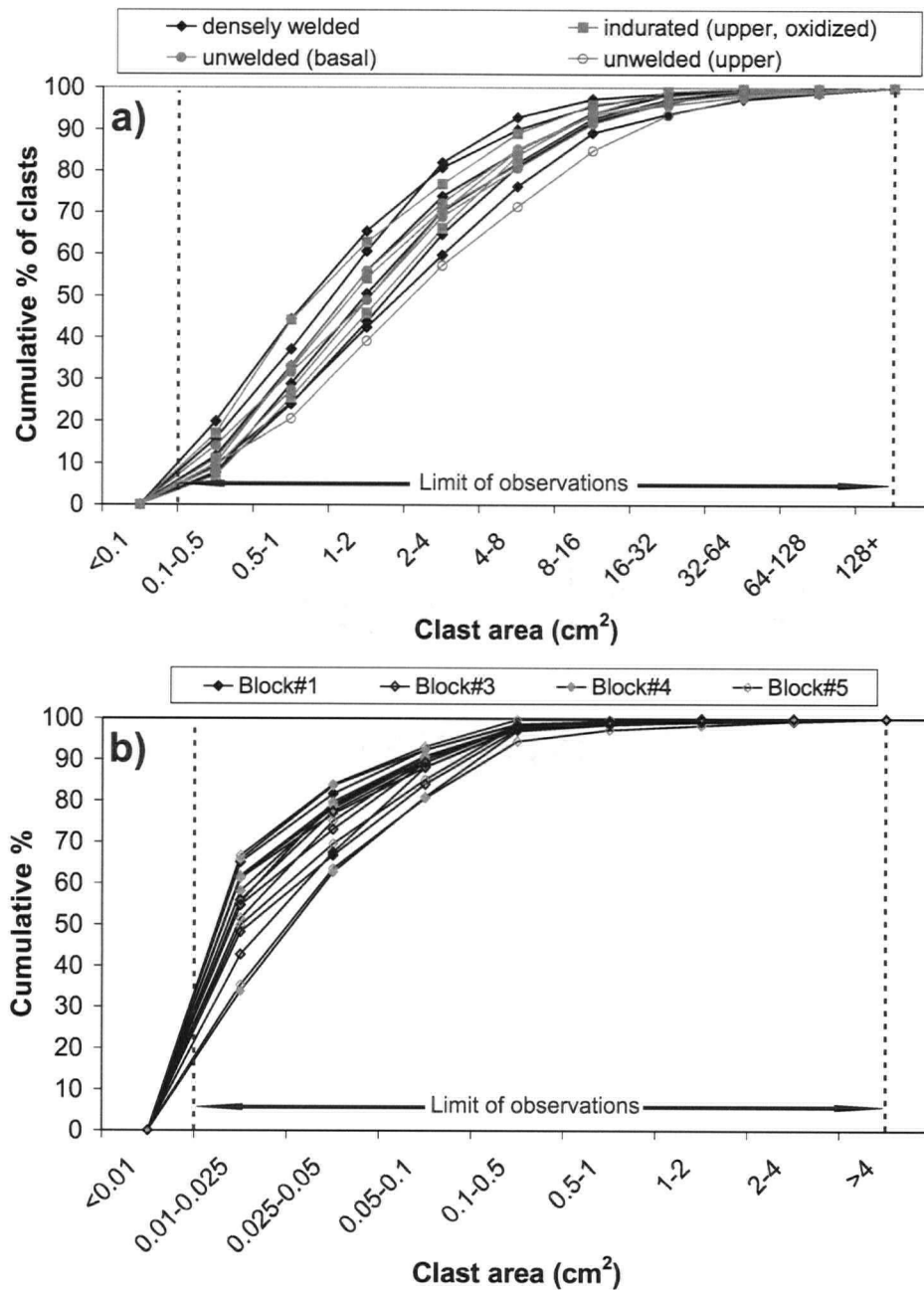
Figure 12: Cumulative grain size distribution for **(a)** FTMs, separated by facies, and **(b)** STMs, separated by block of densely welded block and ash flow deposit. It is important to note that the various facies/blocks of material cannot be distinguished by their grain size distribution at these scales.

29

Other properties of the clast population were also examined through image analysis. Oblateness has been proposed as an indicator of welding intensity (Quane and Russell, 2005a) and it is calculated using the following formula:

$$Oblateness = 1 - \frac{c}{a} \qquad (1)$$

where c = minimum clast diameter, and a = maximum clast diameter. The more flattened and compacted a clast is, the more welded it is, and thus, the higher its oblateness will be. Another indicator of welding intensity may be clast orientation; Sheridan and Ragan (1976) reported that mechanical deformation (i.e., non-viscous, below T_g) was insufficient to change the orientation and alignment of particles. They argued that a compactional load driving viscous deformation (i.e., above T_g) was responsible for producing elongated clasts that then rotate towards the horizontal (Ragan and Sheridan, 1972; Sheridan and Ragan, 1976). Alternatively, clasts in non-welded deposits are expected to have random orientations averaging 45° from the horizontal. Thus, a plot of averages of these two properties for each FTM (Fig. 13a) might serve to numerically distinguish between facies observed in the field. As evident in Figure 13a, each facies of this block and ash flow plots in order of increasing welding intensity from the bottom right to the top left in terms of orientation and oblateness. Upper non-welded deposits near Keyhole Falls have the highest (most random) average clast orientations (36°), and one of the lowest (least deformed) values of oblateness (0.33). The basal non-welded block and ash flow deposits, on average, have high clast orientations (32 – 34°), and low values of clast oblateness (0.32 – 0.35). Incipiently welded deposits show a decrease in average clast orientation (27 – 29°), and as expected, an increase in average clast oblateness (0.37 – 0.39). Finally, the densely welded block and ash flow deposits have the lowest average clast orientations (22 – 26°), and the

highest values of average clast oblateness (0.40 – 0.43). The FTM drawn in the plane of

flattening has a near-random average clast orientation (41°), and an intermediate value of average

clast oblateness (0.36). The STMs exhibit much greater ranges in these properties (Fig. 13b),

suggesting that on the centimeter scale, welding intensity is highly heterogeneous. Not only are

the blocks of densely welded material indistinguishable from one another, but the ranges of

average oblateness and orientation for all STMs nearly span the full range of oblateness (0.35 –

0.43) and orientation (21 – 36°) for the entire deposit. This is an indication that strain is much

more localized at this scale.
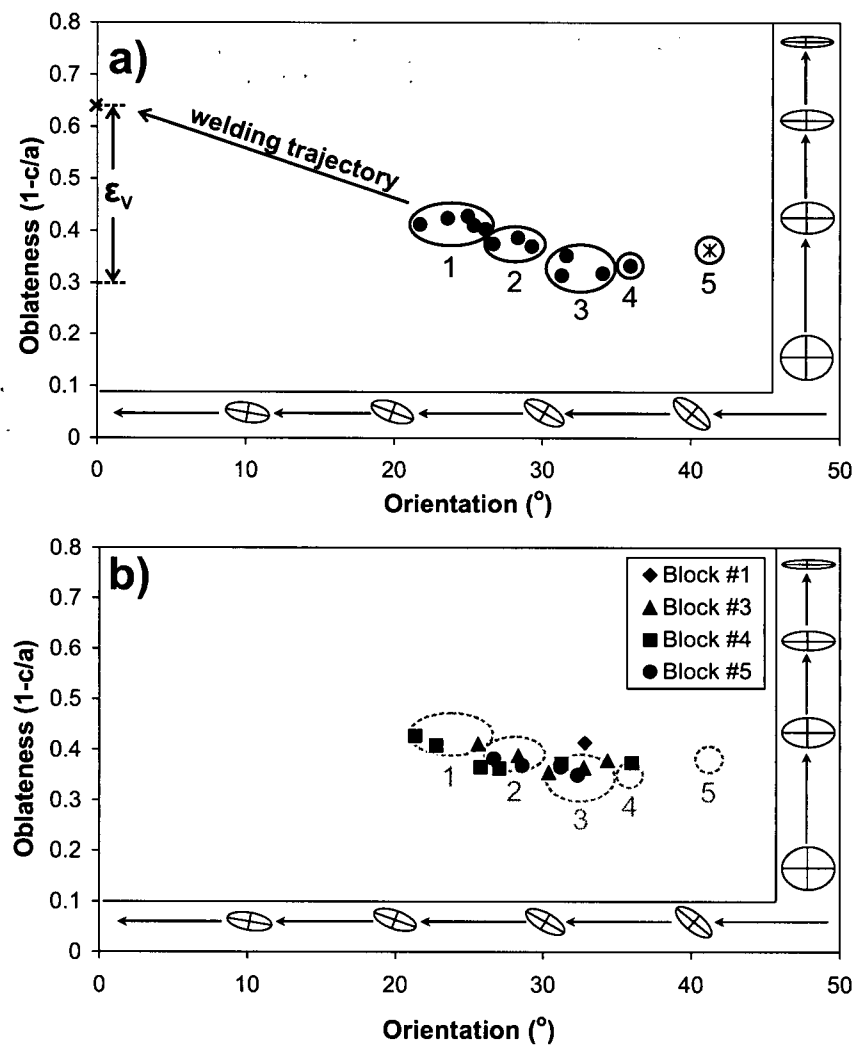
Figure 13: Average clast orientation is plotted against average clast oblateness for **(a)** FTMs, and **(b)** STMs. FTMs are grouped by facies: (1) densely welded facies, (2) upper, incipiently welded facies, (3) non-welded basal facies, (4) upper, non-welded facies and, (5) densely welded facies mapped in the plane of flattening. Welding is expected to promote high clast oblateness and low clast orientation due to compaction. Non-welded deposits would have a low clast oblateness (e.g. near-spherical), and a random clast orientation of 45°. The deposit remains heterogeneous at the sub-metre scale as indicated by data from the STMs. STM samples originate from the densely welded section (group 1 of the FTMs) but show as large a range as the entire suite of FTMs.

32

Oblateness is also a useful metric of strain. If all strain results in volume loss (e.g., volume

strain, ε_V), then oblateness is mathematically equal to strain for spherical particles:

$$\varepsilon_V = 1 - \frac{c}{a} \qquad (2)$$

If the strain conserves volume (e.g., pure shear strain, ε_S), then:

$$\varepsilon_S = 1 - \left(\frac{c}{a}\right)^{2/3} \qquad (3)$$

Two end-member strain paths are therefore possible for the clasts in the block and ash flow

deposit. Ideally, if the clasts start as spheres, oblateness and volume strain would have a linear

1:1 relationship. My values of oblateness define a curvilinear relationship against strain with a

non-zero intercept (Fig. 14, inset). The non-zero intercept suggests that the clasts in the non-

welded deposit had an original oblateness of approximately 0.30 (from Fig. 13a, 14). Taking

into account original clast oblateness, the values of oblateness for the most welded deposits

suggests a maximum of 12% volume strain, or approximately 9% pure shear strain. Strain

values for densely welded ignimbrites are usually much higher. For example, Quane and Russell

(2005a) define 'densely welded' ignimbrite deposits as those with oblateness values greater than

0.82. However, this deposit cannot be classified using Quane and Russell's (2005a) ranking

because its original oblateness is greater than zero, and because the blocks are not pumiceous in

nature.
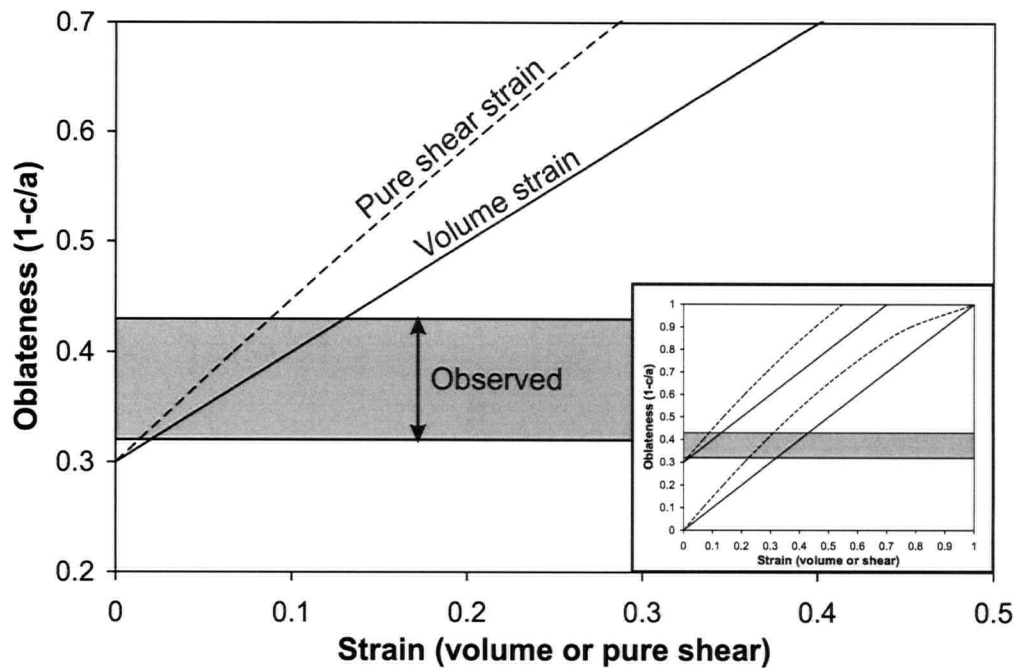
Figure 14: Strain *vs.* expected oblateness (1-c/a) for volume strain (solid line), and pure shear strain (dashed line). Inset shows complete strain paths assuming that particles are initially spherical. Main figure accounts for an original oblateness of 0.3, which is a conservative estimate based on non-welded deposits (Figure 13). If this is the case, values of strain incurred by the welded block and ash flow deposit are approximately 12% for volume strain and 9% for pure shear strain.

3.2.1. Empirical Experiment with Image Analysis

The welding trajectory is defined by average values of oblateness and orientation for FTMs, but they provide a substantially lower estimate of strain (12%) than expected. An empirical experiment was devised to investigate the progression of volume strain using the least welded FTM. FTM 08, a texture map deriving from a section of the basal non-welded facies was digitally reduced in its vertical dimension by 10, 20, 30, 40 and 50% which is exactly equivalent to a volume strain of 10, 20, 30, 40 and 50% (Fig. 15). FTMs from the densely welded facies (FTM 05, 06) were then compared to the digitally 'strained' images of FTM 08. The images of FTM 05 and 06 most closely resembled FTM 08 after a 'strain' of 30 – 40%. This experiment and visual comparison of images implies that the densely welded facies have undergone 30 – 40% volume strain, relative to the non-welded facies. This is a value much higher than 12%, as estimated using average oblateness of FTMs. Subsequently, image analysis of FTM 08 after a 'strain' of 50% was completed to obtain values of oblateness and orientation. Scion Image™ revealed FTM 08 had an average oblateness of only 0.54 after being digitally 'strained' by 50%. Thus, an accommodation of 50% volume strain only resulted in a 0.22 increase in average oblateness. This is consistent with the lower-than-expected average oblateness values associated with the densely welded FTMs and STMs.

Figure 15: Digital images produced from computer-simulated shortening of FTM 08, which represents the unwelded block and ash flow deposit. Simulations show incremental shortenings (e.g., volume strains) of 10, 20, 30, 40, and 50%. FTM 05 and 06 are displayed to show their similarity to FTM 08 after undergoing 30-40% volume strain. Of note is that average oblateness should parallel values of volume strain incurred, but $\varepsilon_v = 50\%$ produces a lower than expected average oblateness of 0.54.

FTM 05
(oblateness = 0.41)

FTM 06
(oblateness = 0.43)

FTM 08
basal unwelded
$\varepsilon_v = 0\%$
oblateness = 0.32

$\varepsilon_v = 10\%$
(volume strain by collapsing pores)

$\varepsilon_v = 20\%$

$\varepsilon_v = 30\%$

$\varepsilon_v = 40\%$

$\varepsilon_v = 50\%$
oblateness = 0.54

36
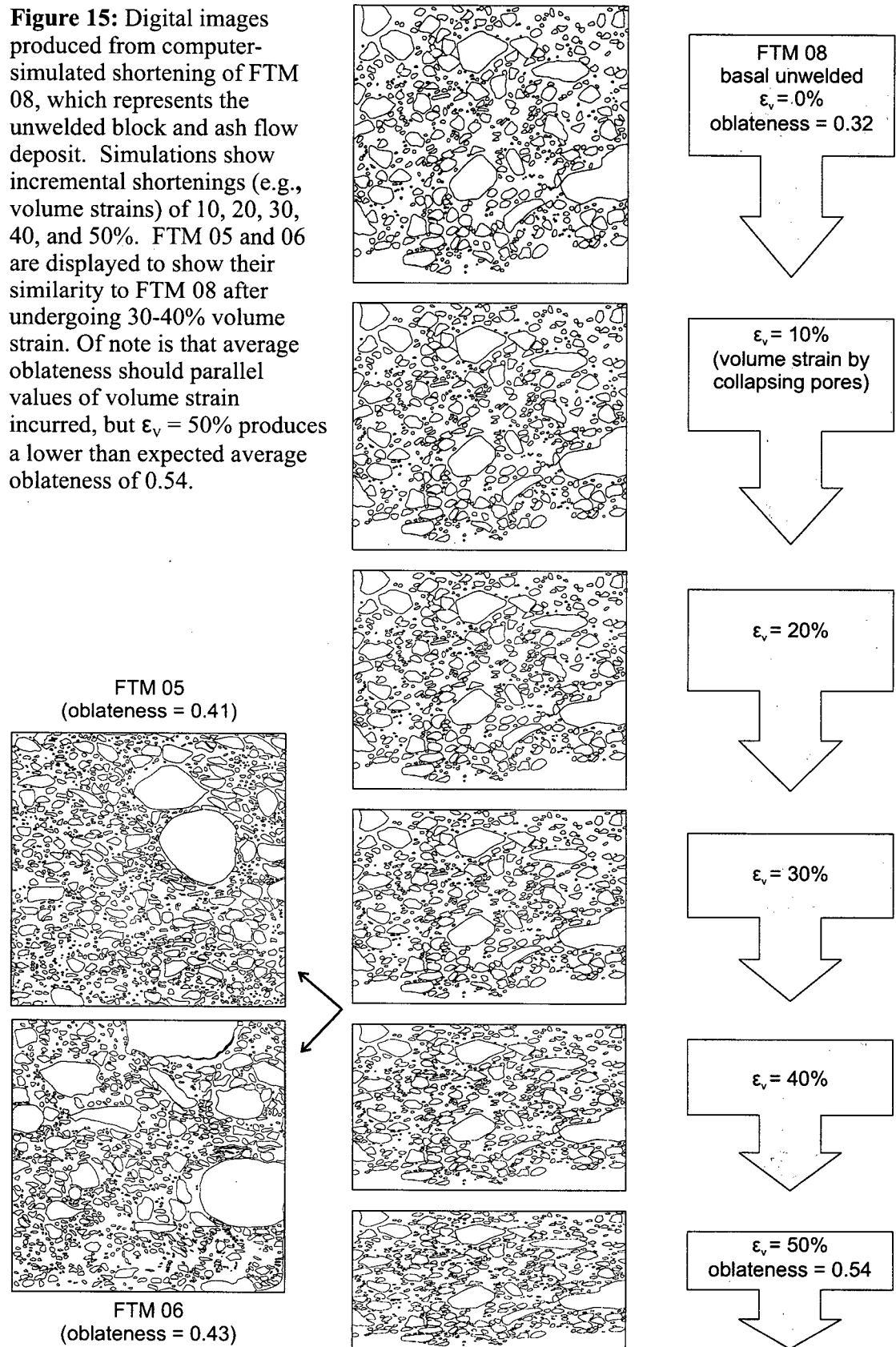
3.2.2. Distributions of Oblateness and Orientation

Distributions of clast oblateness and orientation were examined in the FTMs in an effort to further examine the nature of strain. The distributions were created using plots of normalized frequency *vs.* oblateness (bin size = 0.1) or orientation (bin size = 10°). Oblateness shows near-normal distributions whereby the degree of skewness to the right (towards larger values of oblateness) defines the degree of welding (Fig. 16). The densely welded facies (FTMs 01, 02, 04 – 06) show the most skewness towards the right, whereas non-welded facies (FTMs 07, 08, 13) show more normal distributions or even a skewness towards the left. Incipiently welded facies (FTMs 09, 10, 12) show intermediate trends. In most cases, a well defined peak also appears in those distributions representing densely welded sections. FTMs 04 – 06 show this feature, whereas some non-welded sections (i.e., FTM 11) show irregular distributions. Incipiently welded sections, once again, show intermediate results. The peak values of oblateness are also significantly higher than the averages calculated for each FTM. On average, the densely welded facies show a maximum frequency at 0.4 – 0.5, whereas the incipiently welded facies peak at 0.3 – 0.5, and the non-welded facies peak at 0.2 – 0.4. The distribution of oblateness seen in the digitally deformed FTM 08 (50% volume strain) is a prime example of these three features in a densely welded deposit (Fig. 17). FTM 03, drawn of the densely welded facies in the plane of flattening; it shows a sharp peak but it is skewed to the left at a maximum frequency of 0.3 – 0.4.
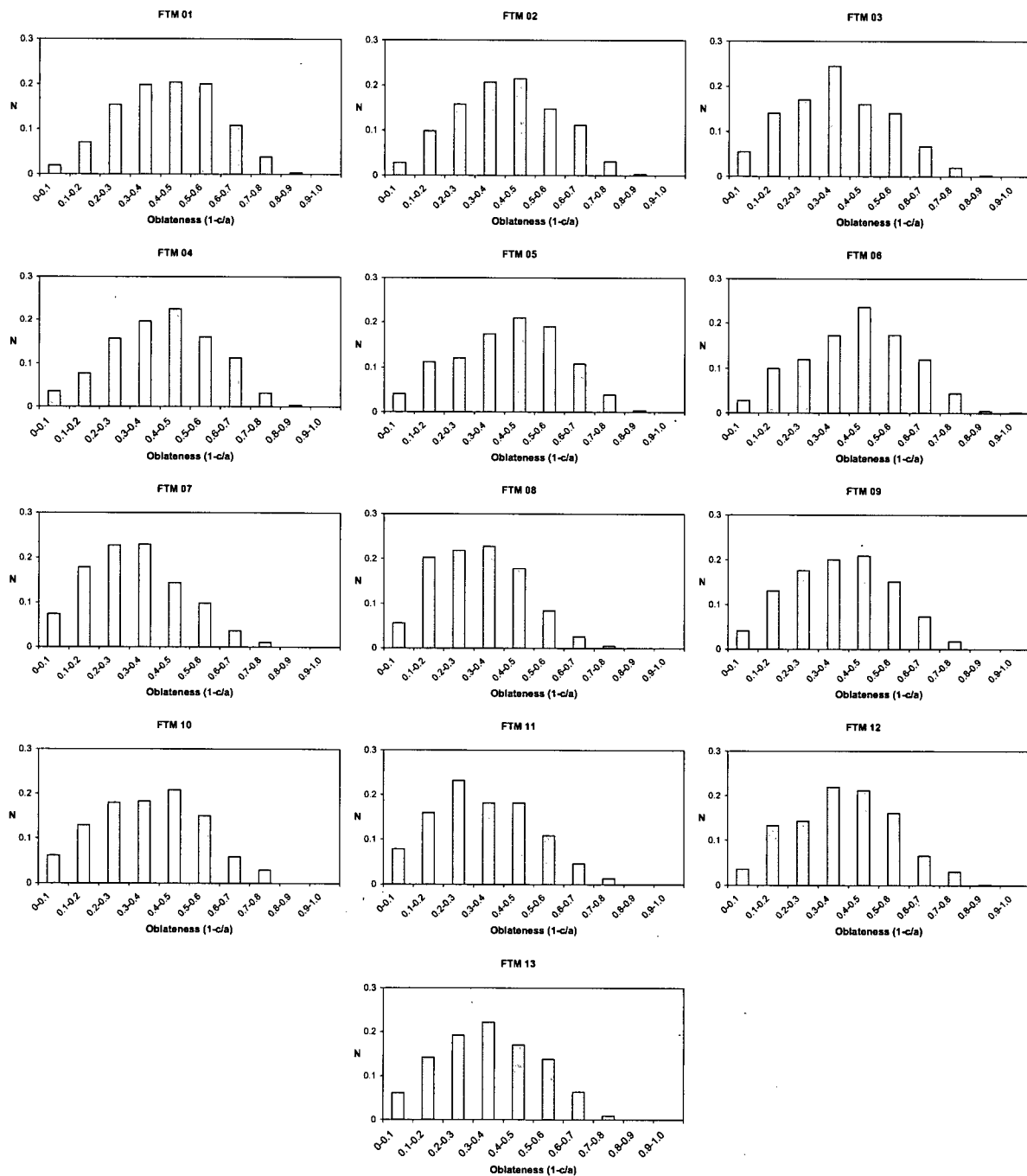
Figure 16: Distribution of oblateness for each FTM. Most display a normal or near-normal distribution which becomes progressively more skewed to the right as welding intensity and the peak oblateness values increase. Numbers indicate the chronological order in which the field texture maps were completed (e.g., not welding intensity).

FTM 08 (-50%)
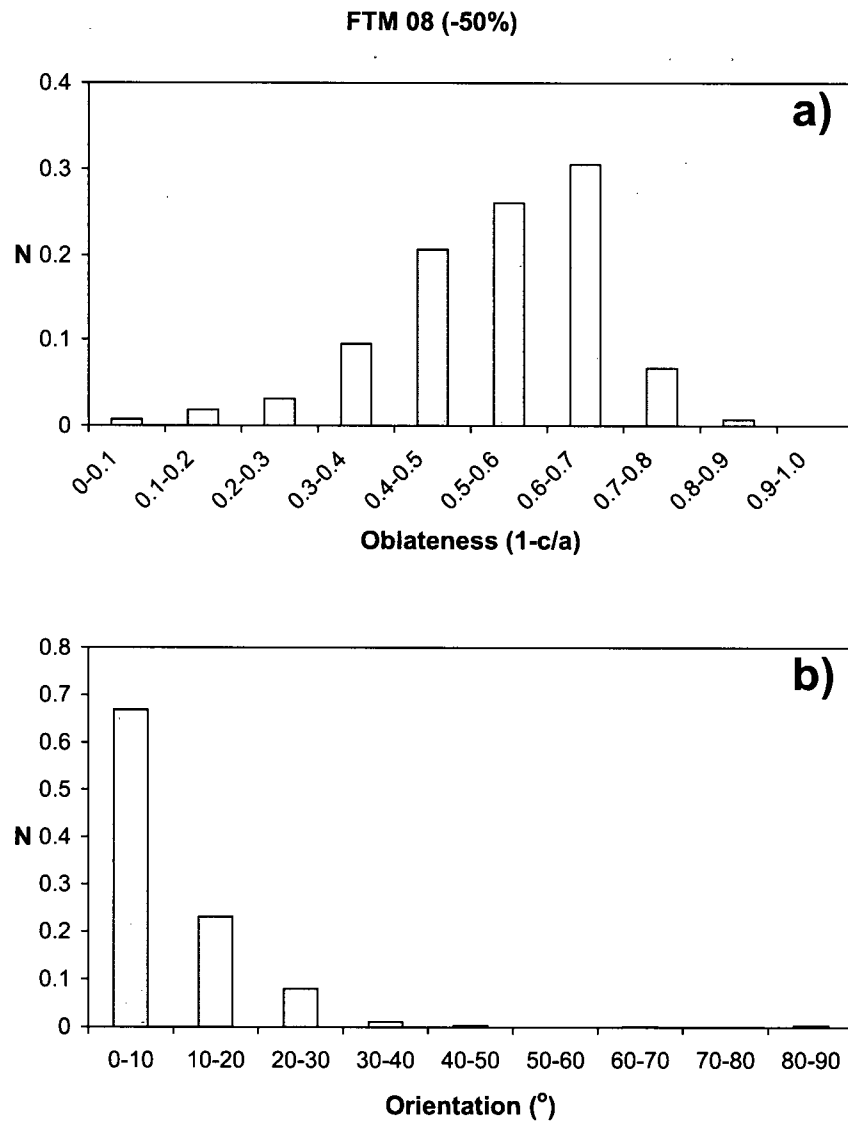
Figure 17: Distribution of **(a)** oblateness and **(b)** orientation for a 50% volume-reduced FTM 08. Oblatess shows a near-normal distribution skewed to the right, with a peak oblateness of 0.6 – 0.7. Orientation shows a negative exponential distribution with less than 1% of clasts at angles greater than 40° from the horizontal.

As welding intensifies, orientation shows an increasingly negative exponential distribution from low to high clast orientations (Fig. 18). Densely welded FTMs show the most pronounced exponential distributions with a strong peak at $0 - 10°$. Incipiently welded facies commonly show a more subtle or irregular curve with a maximum frequency at $0 - 10°$. Non-welded deposits show an irregular or nearly flat trend, although the maximum frequency still occurs at $0 - 10°$. The FTM drawn of the densely welded facies in the plane of flattening (FTM 03) demonstrates a nearly flat trend, with a maximum frequency of $30 - 40°$. The distribution of orientation seen in the digitally deformed FTM 08 shows an extremely steep negative exponential curve, with less than 1% of clasts having an orientation greater than $40°$ (Fig. 17).
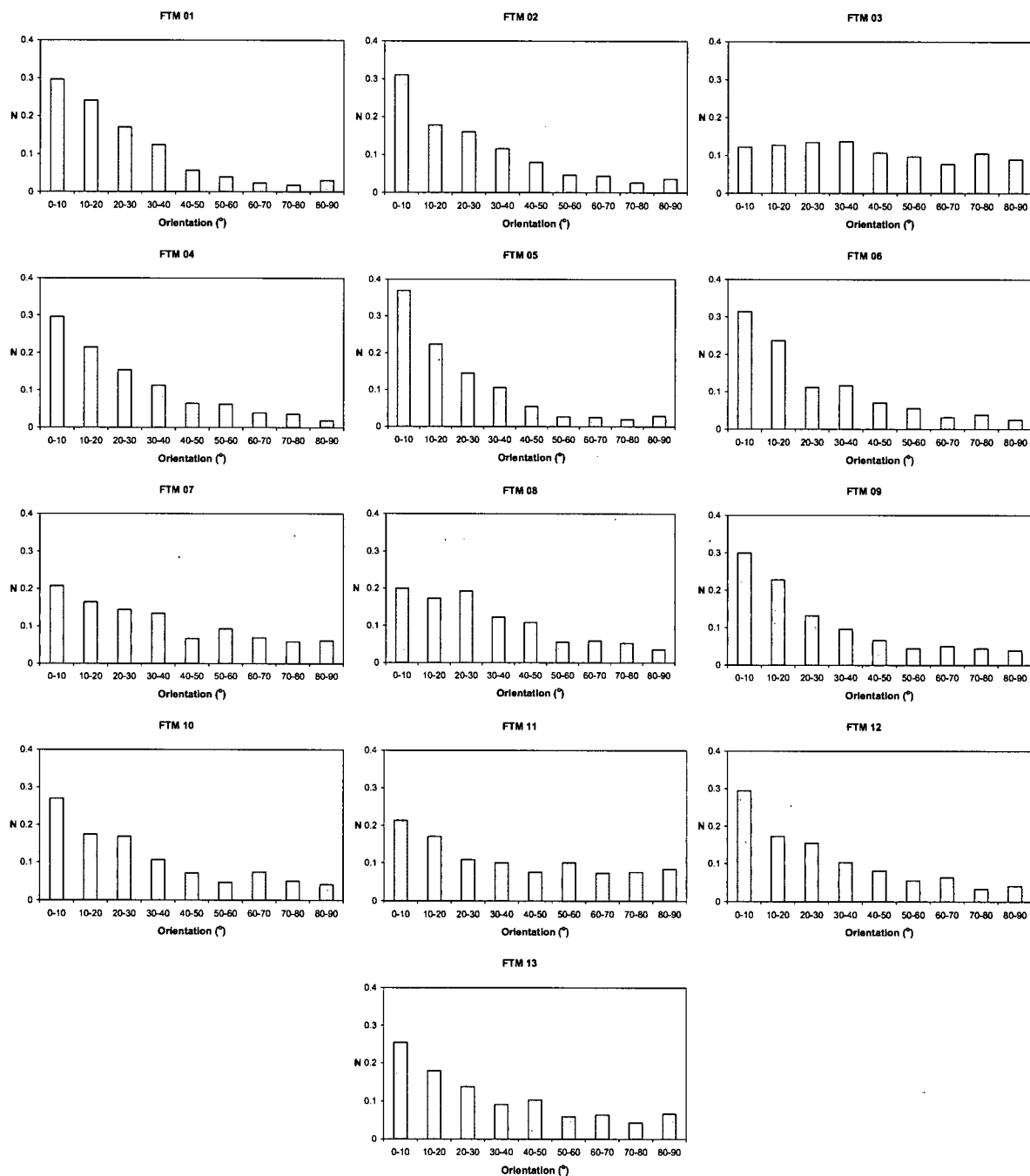
Figure 18: Distribution of orientation for each FTM. The distributions become progressively more exponential in shape as welding intensity increases. Numbers indicate the chronological order in which the field texture maps were completed (e.g., not welding intensity).

CHAPTER FOUR

PETROGRAPHY & SEM ANALYSIS OF TEXTURES

Petrography and analysis using the scanning electron microscope (SEM) are used to provide a description of the Keyhole Falls Member at the micro-scale. These observations reinforce the fact that this deposit is a welded block and ash flow. The textural observations provide evidence of welding processes that cause flattening of particles, development of fabric, and a loss of porosity. This chapter also serves to contrast components, porosity, textures and relations from non-welded to densely welded deposits. Lastly, these observations constrain the mechanisms involved in welding the block and ash flow deposits. For a detailed description of Pebble Creek Formation mineralogy, refer to Stasiuk et al. (1996).

4.1.   Petrography

Petrographic descriptions derive from 36 thin sections ranging from non-welded to densely welded facies of the block and ash flow deposit. Thin section analysis records the development of a foliation, progressive deformation of the clasts, and a reduction in total porosity in both clasts and matrix with increasing welding intensity.

4.1.1. Non-welded Facies

Due to the unconsolidated nature of the non-welded matrix, only non-welded juvenile clasts were examined in thin section. Clasts possess a glassy, highly vesicular groundmass with phenocrysts of plagioclase, orthopyroxene, amphibole, and biotite, with rare phenocrysts of clinopyroxene, quartz and apatite. Subhedral, sieve-textured plagioclase crystals dominate the phenocryst population, ranging in length from 1.5 – 4.0 mm. They are commonly complexly zoned, sometimes bearing an outer euhedral rim of plagioclase growth. Plagioclase also occurs as smaller, 0.2 – 1.0 mm, euhedral, albite-twinned, lath-shaped crystals. Euhedral crystals of 0.2 – 0.4 mm-long orthopyroxene represent the most abundant ferro-magnesian phase. Amphibole occurs as individual subhedral, 0.2 – 0.5 mm-long crystals as well as reaction rims on biotite crystals. Biotite is clearly out of equilibrium, occurring as 0.5 – 1.0 mm, highly corroded crystals or coring a reaction rim of amphibole+oxides±pyroxene. Also present are crystal clots or glomerocrysts. These clusters of crystals vary from 2 – 7 mm in diameter, but are present in all samples of block and ash flow deposits. Glomerocrysts comprise crystals of plagioclase, biotite-cored amphiboles and oxides, orthopyroxene, and apatite. Vesicles represent approximately 30 – 40% of the clast volume and are frequently located adjacent to phenocrysts or glomerocrysts (Fig. 19a). They are sub-spherical to elongate in shape, and range in size from 0.1 – 1.0 mm. Clasts may also demonstrate flow banding or mingling textures, whereby darker-coloured, more phenocryst-rich material is mingled with the material described above.

4.1.2. Incipiently Welded Facies

Juvenile clasts from the incipiently welded facies are mineralogically equivalent to those from the non-welded facies. Clast sizes range upwards from 0.5 mm in diameter and are sub-spherical to irregular in shape. Juvenile clasts are glassy to highly vesicular in nature, whereas clasts from the Plinth assemblage are plagioclase-porphyritic. Intrusive igneous clasts are holocrystalline and noticeably coarser grained, whereas other lithic clasts contain abundant acicular or lath-shaped plagioclase phenocrysts. Small, fine-grained lithic clasts of sedimentary rocks are also observed. Vesicles are variable in shape and size, but the largest ones are found in pumice-like clasts (Fig. 19b). Flow banding is visible in some juvenile clasts, similar to those found in juvenile clasts from the non-welded facies. The incipiently welded matrix of the block and ash flow deposits is vitroclastic; the matrix contains many broken crystals/clast fragments that are less than 0.25 mm in diameter. There is also, in general, a greater concentration of crystals in the matrix than in juvenile clasts. The porosity in the matrix is difficult to identify at this scale, but appears to consist of a network of small, connected vesicles. This material is sintered together, and there is little evidence of clast deformation. There may be slight differences in porosity between the non-welded and incipiently welded facies, but they are difficult to discern with the naked eye.
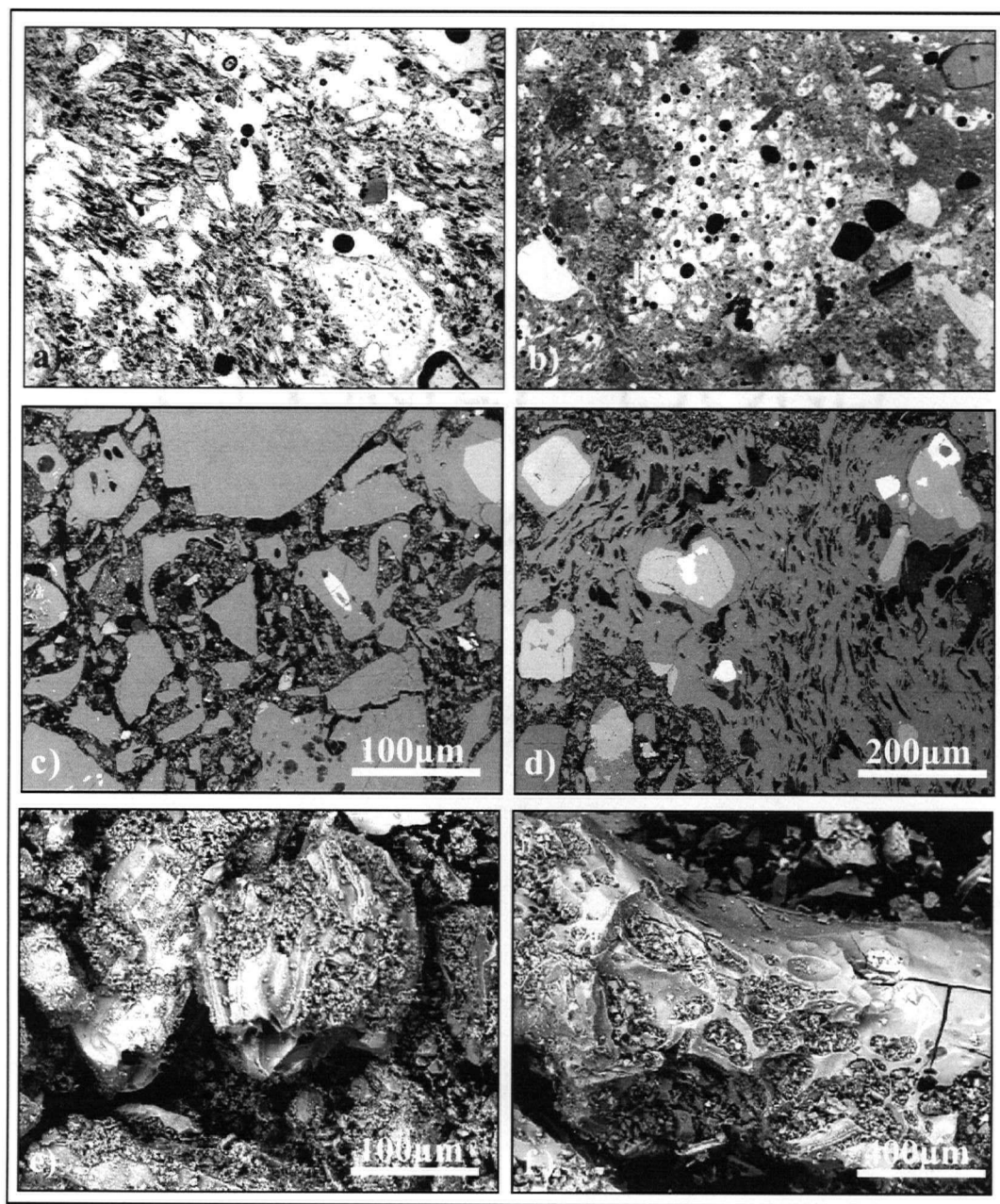
Figure 19: Summary of common features within the non-welded to incipiently welded block and ash flow deposits at Mount Meager: **(a)** vesicular, non-welded pumice-like clast (FOV = 3.9 mm); **(b)** vesicular pumice-like clast in incipiently welded deposits (FOV = 3.0 mm); **(c)** shard size range averaging 50 – 500 μm, **(d)** fragmented crystal and glass amalgamations; note the stretched vesicles in the larger shard all aligned in the same general manner, **(e)** moss-like adhesion of fine ash to larger particles, **(f)** spherical to discoid-shaped vesicles within a large blocky shard.

45

4.1.3. Welded Facies

The componentry and mineralogy of the welded facies parallels that described for the non-welded and incipiently welded facies. However, deformation due to compaction and volume strain is prominent. Clasts are noticeably more elongate in shape (Fig. 20a), in comparison to their less welded counterparts. In addition, elongate clasts show a particle alignment (perpendicular to flattening), resulting in a foliation (Fig. 20b). Loss of porosity due to volume strain is most evident in the clasts, where collapsed pores have left behind wispy structures (Fig. 20c). These wispy structures also have formed parallel to the length of the flattened clast (Fig. 20a). Where these wispy structures are absent, the collapsed pores may have been completely obliterated by the welding process. Where these structures are not aligned parallel to fabric, the clasts' groundmass has collapsed around a crystal/crystal fragment (Fig. 20d). Optically, there is very little discernable porosity remaining in the clasts (<5%) (Fig. 20e), and only slightly more remaining in the matrix (5-10%). Deformation in the matrix is less noticeable due to its glassy nature, but can be observed in areas between larger clasts. In these areas, the matrix has been reduced in volume to the extent that clasts in close proximity are interacting and deforming (Fig. 20f).
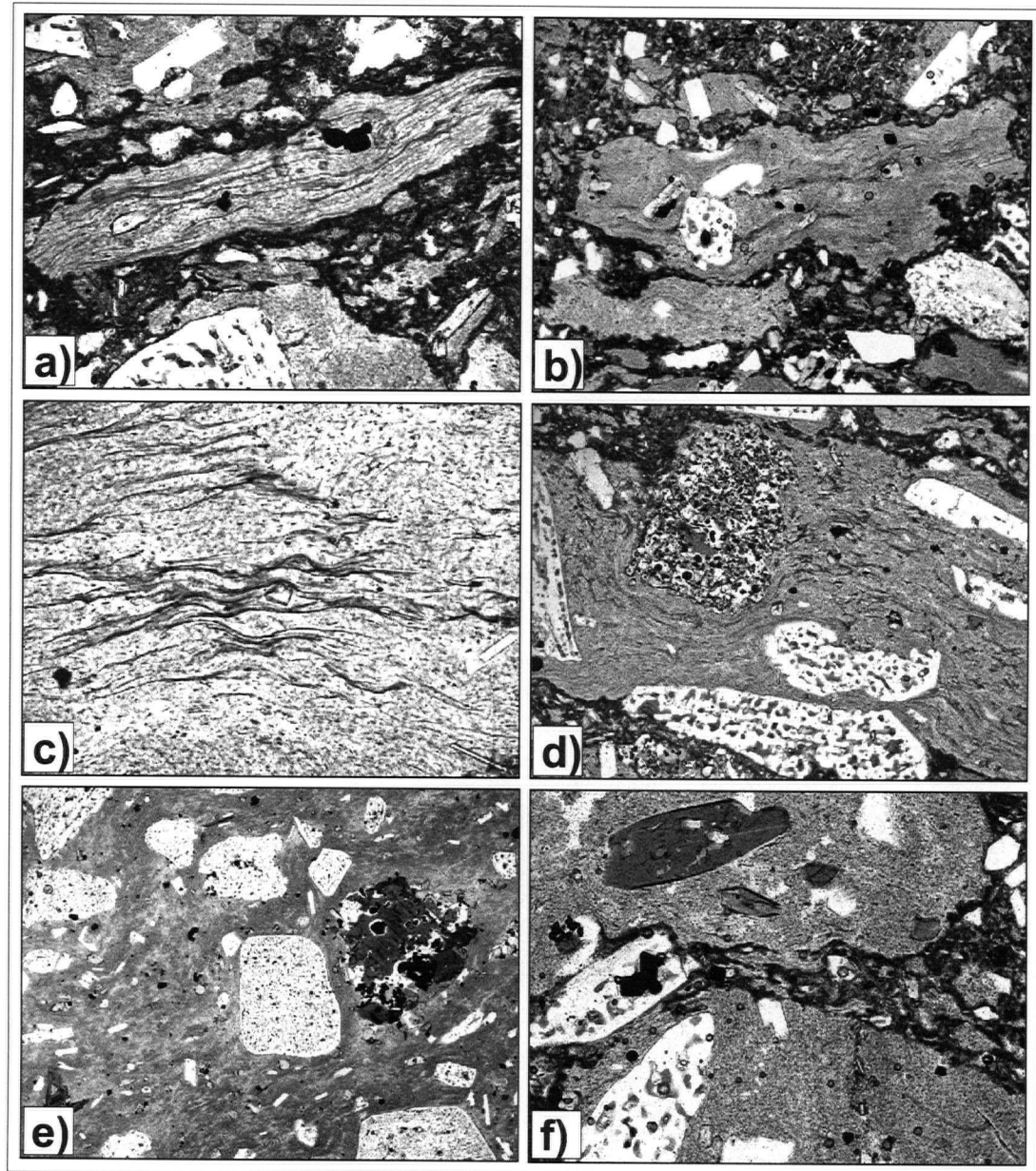
Figure 20: Welding textures observed in thin section: **(a)** elongated clast formed due to loss of porosity (FOV = 3.9 mm). It is important to note that the collapsed vesicles are consistently parallel to the length of the clast. **(b)** elongated clasts forming a parallel fabric (FOV = 3.9 mm); **(c)** close-up of collapsed vesicles around a small crystal fragment (FOV = 1.0 mm); and, **(d)** compacted vitrophyric rhyodacite clast showing collapsed vesicles (wispy structures) and localized strain in proximity to crystals (FOV = 3.9 mm); **(e)** dense vitrophyric glassy clast lacking porosity (FOV = 7.8 mm); and, **(f)** deformation in matrix evident between two larger clasts (FOV = 2.0 mm).

4.2. SEM Analysis

The SEM facilitates the detailed study of the ash fraction, which includes particles smaller than 2 mm (2000 μm). A detailed SEM examination of volcanic shards from samples of the Keyhole Falls Member is presented below, representing the following facies: (a) non-welded to incipiently welded, (b) moderately welded, and (c) densely welded block and ash flow deposits (Table 4). Samples from the non-welded to incipiently welded sections allow for primary textures and attributes of the pyroclastic material to be identified. SEM analysis of moderately to densely welded samples will reveal the changes in pyroclast texture due to welding and, thus, will constrain the mechanisms of the welding process.

The material used for SEM analysis comprised loose grains (matrix from non-welded deposits), small (~1 cm) rock fragments (from densely welded and incipiently welded deposits), and polished thin sections (from densely welded and incipiently welded deposits). The variety of sampling allows for two-dimensional and three-dimensional visualizations of the glass shards and pore space. Back-scattered electron images were acquired with a Philips XL-30 Scanning Electron Microscope with Princeton Gamma-Tech energy-dispersion X-ray spectrometer and image analysis systems. Attributes such as shard type, shard shape, shard size, and texture were observed in each sample, and then compared to each other in an effort to identify distinguishing features associated with the welding process. Image analysis software (Image J™) was used in conjunction with the SEM images taken from polished thin sections to recover porosity. This method, however, is approximate (total porosity (Φ_T) ± 5%) due to the thresholding limitations of the software and the subjectivity involved in identifying void space.

Table 4. Sample suite chosen for SEM study of a variably welded block and ash flow deposit, and expectations according to parallel research in ignimbrites.

Sample	Format	Welding facies	Expectation in ignimbrites
KM-04-018	loose grains	non-welded[*]	no deformation
KM-04-031	loose grains	non-welded	no deformation
KM-04-015c	thin section	incipiently welded	little to no deformation
KM-04-017	rock fragment	incipiently welded[*]	little to no deformation
KM-05-063	thin section	moderately welded	moderate deformation
KM-05-017c	rock fragment	densely welded	extensive deformation
KM-05-012	thin section	densely welded	extensive deformation

[*]oxidized sample

49

4.2.1 Non-welded Facies

SEM analysis of non-welded samples of the block and ash flow deposit, allows the study of primary, non-welded pyroclasts. Samples are of loose to barely consolidated ash of the block and ash flow deposit, and they comprise four main types of shards. Most (60%) of the particles are blocky in habit; others are bubble-wall (20%), platy (10%), and pumiceous (10%) shards (Fig. 21). The shards show little evidence of mechanical abrasion during transport as their overall shapes remain sharp, arcuate, curvilinear, or angular. Shard size varies from approximately 5 μm to several hundred μm, with most shards in the 50 – 500 μm range (Fig. 19c). The non-welded to incipiently welded section of the block and ash flow deposit comprise euhedral crystals of plagioclase, pyroxene, and amphibole enclosed by glass selvages. Some crystal and glass selvage ensembles are fragmented (Fig. 19d). Finer particles (5 – 50 μm) tend to adhere in a moss-like manner to the larger glass shards (Fig. 19e). Larger ash particles (500 – 1500 μm) commonly contain multiple vesicles which are stretched in the same general orientation (Fig. 19d). Otherwise, blocky, platy and bubble wall shards show vesicles that are dominantly spherical to discoid in shape (Fig. 19f). The more pumiceous shards commonly host abundant tubular vesicles (Fig. 21d).
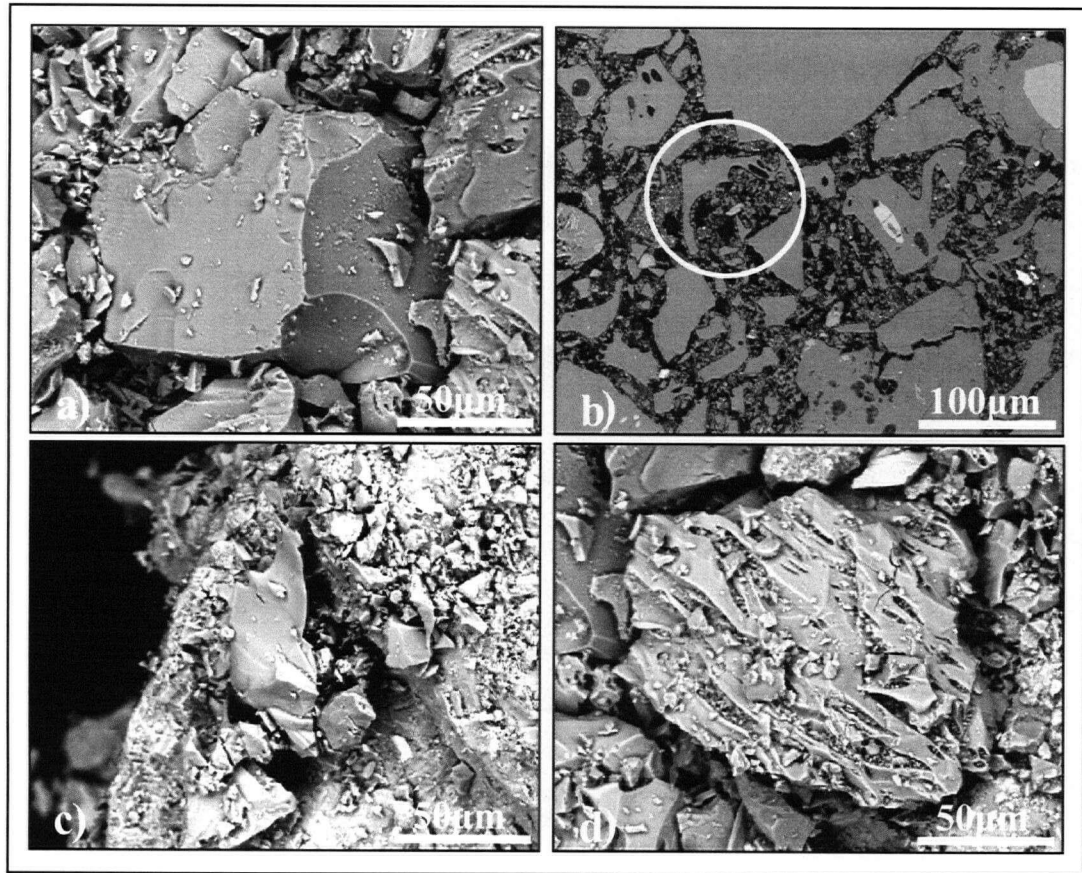
Figure 21: Shard types observed in the non-welded to incipiently welded block and ash flow deposits at Mount Meager: **(a)** blocky, **(b)** bubble-wall/cuspate, **(c)** platy, and **(d)** pumiceous.

4.2.2. Welded Facies

The examination of the densely welded block and ash flow deposits at Mount Meager under the SEM allow for a contrast with the non-welded deposits. It also allows for features that are only associated with the welding process to be isolated from those brought about by earlier processes such as fragmentation and transportation.

In general, there are five main types of glass shards identified in the ash of the densely welded deposits: (a) larger (>50 μm) blocky shards (50%), (b) bubble-wall shards (10%) and (c) platy (5%) shards (Fig. 22a-c), as well as smaller shards (<50 μm) that are (d) dendritic to moss-like (75%), or (e) acicular (25%) (Fig. 22d). The shards remain angular, curvilinear, and arcuate in shape, but tend to be more elongated than the non-welded samples (Fig. 22e). Shard size varies from less than 5 μm to approximately 1500 μm, where the bulk of the glass shards are 50 – 500 μm. The densely welded block and ash flow deposit samples comprise euhedral crystals of plagioclase, pyroxene, and amphibole enclosed within glass selvages. The amount of glass encompassing the crystals does not appear to be any thicker or thinner than the selvages observed in the non-welded to incipiently welded samples. The crystal and glass selvage assemblages, however, are fragmented more frequently than those in the non-welded samples. Finer particles, especially those less than 50 μm, tend to adhere in a moss-like fashion to the larger glass shards, and accumulate in the depressions of the larger shards (Fig. 22d). Some pitting and irregular surfaces are evident in larger shards (Fig. 22a, d) and vesicles are less common. Some larger ash particles (500 – 1500 μm) contain multiple vesicles that are stretched in the same direction. Otherwise, the blocky, platy and bubble wall shards show very few

vesicles. Approximately 10% of shards larger than 500 µm contain vapor-phase crystallization of feldspars within their isolated pores (Fig. 22f).

4.2.3. SEM Analysis of Porosity

At the outcrop or hand sample scale, the block and ash flow deposit shows a visible densification of the material with welding intensity. Analysis of porosity at the micro-scale will aid in determining whether this densification is due to a loss in porosity or whether shear stresses also contributed to the welding process. Twenty SEM images of three thin sections analyzed with Image J revealed that the non-welded samples have an average of 29% total porosity (range = 26 – 32%) (Fig. 23a). Densely welded samples have an average of 19% total porosity (range = 13 – 23%) (Fig. 23c). One sample of moderately welded block and ash flow deposit revealed a higher-than-expected average total porosity of 28% (range = 24 – 34%) (Fig. 23b). These values of total porosity can be further subdivided into two types – isolated and connected porosity. Both types are observed in the welded and non-welded deposits, and both are destroyed as welding intensity increases. Isolated porosity is identified qualitatively as voids that are completely hosted by shards or clasts, and where there is a lack of infilling material. In addition, vapour-phase crystallization occurs within some pores, suggesting that these pores were also sealed off from the surrounding environement (e.g., isolated). Pores that are filled with smaller ash or shard particles are common, and these are assumed to represent connected pores. Using these parameters, isolated porosity is visible only in the larger glass shards (> 50 µm). Connected porosity appears in all ash size fractions as both intra- and inter-shard porosity.

53
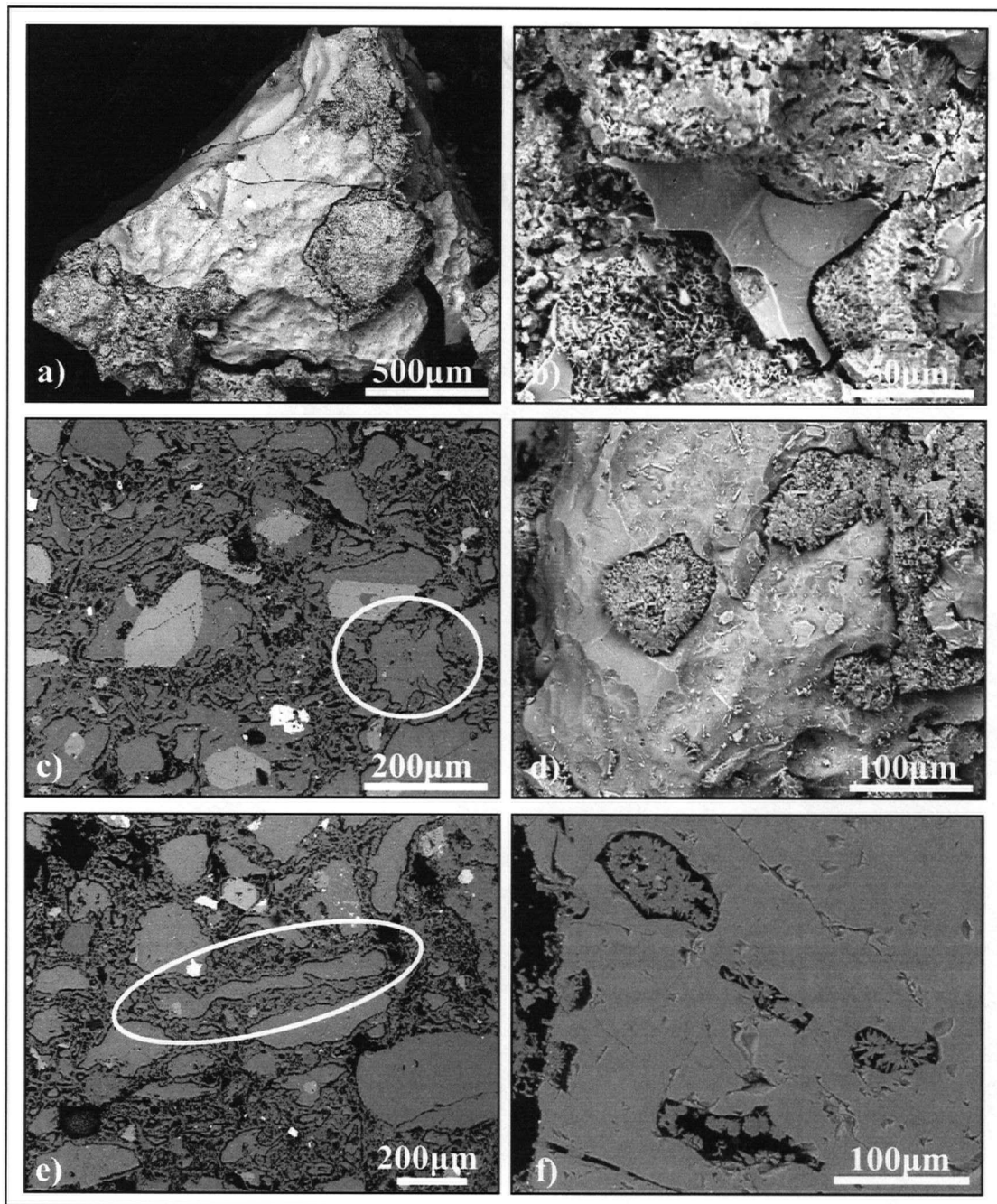
Figure 22: Attributes of the densely welded block and ash flow deposit: **(a)** large, blocky shard showing pitting or irregular surface textures, **(b)** platy shard with bubble-wall remnants, **(c)** bubble-wall/cuspate shard, **(d)** dendritic/acicular/moss-like fine ash filling depressions in larger shards, **(e)** elongated shards, **(f)** vapour-phase crystallization of feldspars within isolated pores of large shards.
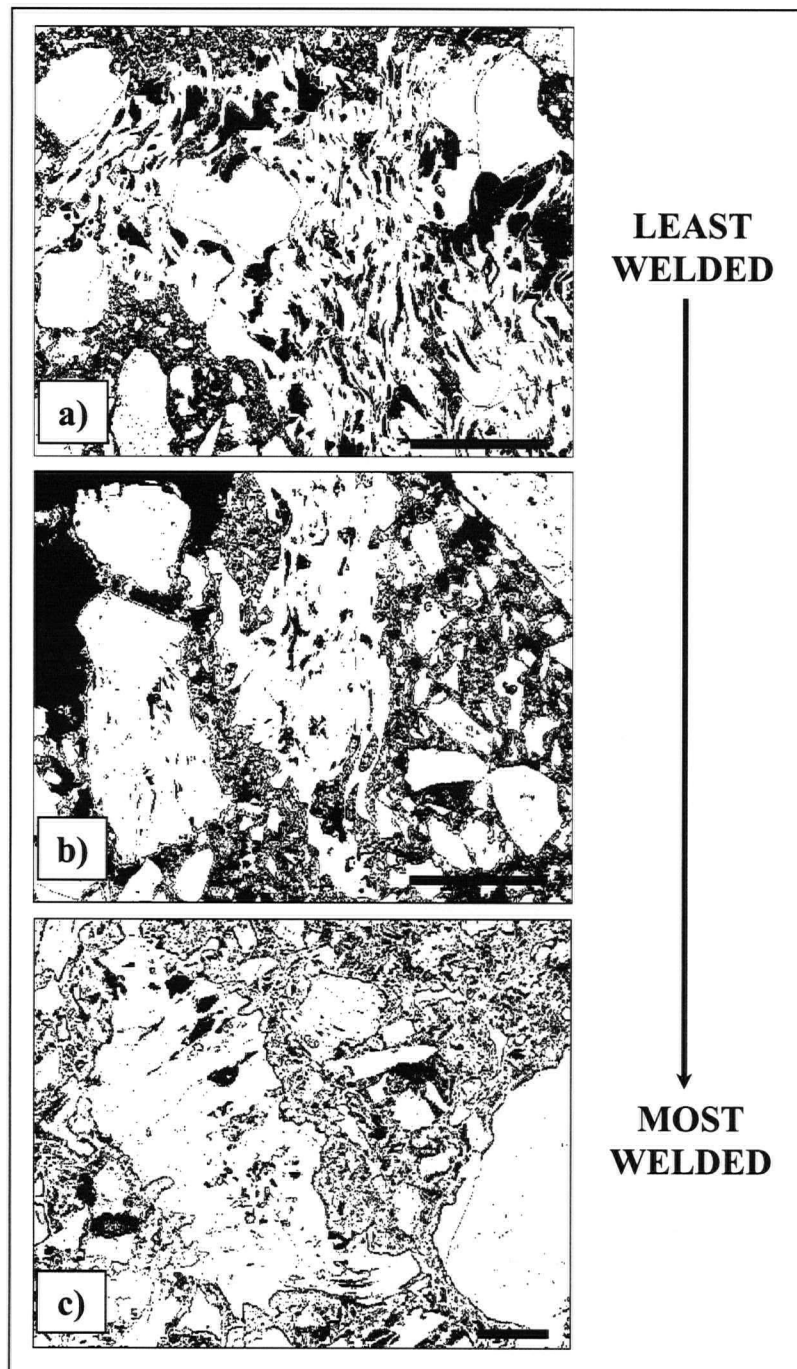
Figure 23: Output images from Image J™, where black = porosity and white = shards/crystals. There is a substantial decrease in average porosity from **(a)** the unwelded/incipiently welded sections (29%) to **(c)** the densely welded sections (19%). On average, however, the moderately welded section **(b)** conserves its high porosity (28%). All scale bars represent 200 μm.

55

CHAPTER FIVE

PHYSICAL PROPERTIES

Density and porosity are strongly coupled properties of pyroclastic rocks, and vary strongly with welding and compaction (Ragan and Sheridan 1972; Streck and Grunder 1995; Rust and Russell 2000; Quane and Russell, 2005a). A suite of more than 100 samples was collected from all facies of the block and ash flow deposits. Sample selection was done such that both matrix and clast components of the deposits are well represented. Density and porosity were measured for all samples and are used below to investigate the welding process. Specific methods and procedures for measuring density are summarized in Appendix D.

In this study, measurements of density and porosity involve three separate experiments. Bulk density (ρ_B) is used here to denote the density of the rock and all of its pores, including both connected and isolated pore space. Bulk density of consolidated samples derives from measurements of sample mass and geometrical volume (e.g., with digital calipers) calculated for cylindrical cores. For unconsolidated materials, a graduated cylinder was packed with sample to a specified volume and the mass was recorded (Appendix D). Skeletal density (ρ_S) is the density of the rock and its isolated (non-penetrated) porosity. Skeletal density of both cylindrical cores and unconsolidated materials was measured by helium pycnometry (Klug and Cashman, 1994; Russell and Stasiuk, 1997). Lastly, an aliquot of each sample was crushed into a powder and the rock powder density (ρ_R) was measured using He-pycnometry (Rust et al., 1999). The rock powder density represents the density of the solid material (powdered rock) only. These three

values of density are useful metrics of welding intensity but can also be used to calculate three

forms of porosity (Φ): total (T), connected (C), and isolated (I):

$$\Phi_T = 1 - \frac{\rho_B}{\rho_R} \tag{2}$$

$$\Phi_C = 1 - \frac{\rho_B}{\rho_S} \tag{3}$$

$$\Phi_I = 1 - \frac{\rho_S}{\rho_R} \tag{4}$$

These calculated values of porosity can also be validated by equating total porosity to the sum of

connected and isolated porosity:

$$\Phi_T \approx \Phi_C + \Phi_I \tag{5}$$

The physical properties for all samples are summarized in Tables 5 – 8. Complete tables of

physical property data can be found in Appendix E.

Table 5. Summary of physical property measurements on bulk samples of unconsolidated block and ash flow deposits, including: bulk density (ρ_B), skeletal density (ρ_S), rock density (ρ_R), total porosity (Φ_T), connected porosity (Φ_C), and isolated porosity (Φ_I). Standard deviations are reported as 1σ.

Sample	ρ_B (g/cm³)	σ	ρ_S (g/cm³)	σ	ρ_R (g/cm³)	σ	Φ_T (%)	σ	Φ_C (%)	σ	Φ_I (%)	σ
KM-04-018[1]	1.47	0.003	2.50	0.003	2.54	0.006	42.1	0.17	41.2	0.13	1.65	0.25
KM-04-019[1]	1.48	0.012	2.52	0.002	2.55	0.002	42.1	0.48	41.3	0.49	1.42	0.12
KM-04-020[1]	1.52	0.014	2.52	0.002	2.53	0.002	39.8	0.57	39.5	0.57	0.41	0.10
KM-04-031[2]	1.59	0.025	2.54	0.002	2.55	0.002	37.8	0.98	37.4	0.98	0.68	0.10
KM-05-023[3]	1.54	0.028	2.52	0.003	2.55	0.003	39.5	1.11	38.7	1.13	1.32	0.14
KM-05-032[1]	1.39	0.028	2.52	0.001	2.53	0.004	45.0	1.09	44.8	1.09	0.34	0.15
KM-05-036[2]	1.43	0.057	2.53	0.001	2.54	0.001	43.6	2.26	43.5	2.27	0.11	0.07

[1] Upper, incipiently welded block and ash flow deposit

[2] Basal, non-welded block and ash flow deposit

[3] Upper, non-welded block and ash flow deposit

Table 6. Summary of measured densities listed by welding facies of the block and ash flow deposit.

Facies	N	Bulk Density (g/cm^3)				Skeletal Density (g/cm^3)				Rock Density (g/cm^3)			
		Avg.	σ	Max	Min	Avg.	σ	Max	Min	Avg.	σ	Max	Min
Non-welded (upper section)	16	1.70	0.122	1.89	1.43	2.46	0.061	2.54	2.37	2.52	0.032	2.59	2.47
Incipiently welded (upper section)	12	1.83	0.275	2.10	1.39	2.44	0.062	2.52	2.34	2.50	0.029	2.55	2.46
Densely welded (middle of section)	57	2.19	0.113	2.37	1.98	2.51	0.040	2.58	2.42	2.52	0.034	2.60	2.45
Moderately welded (middle of section)	6	2.08	0.041	2.13	2.02	2.52	0.030	2.57	2.48	2.53	0.012	2.55	2.51
Non-welded (base of section)	15	1.64	0.126	1.88	1.50	2.31	0.069	2.52	2.24	2.49	0.023	2.55	2.46
All samples	106	1.99	0.273	2.37	1.39	2.47	0.084	2.58	2.24	2.52	0.033	2.60	2.45

Table 7. Summary of calculated porosity values listed by welding facies of the block and ash flow deposit.

Facies	N	Total Porosity (%)				Connected Porosity (%)				Isolated Porosity (%)			
		Avg.	σ	Max	Min	Avg.	σ	Max	Min	Avg.	σ	Max	Min
Non-welded (upper section)	16	32.7	4.88	43.6	24.3	31.0	4.76	43.5	25.0	2.38	1.953	5.7	-1.1
Incipiently welded (upper section)	12	27.4	11.96	45.0	16.1	25.4	13.07	44.8	14.5	2.54	1.821	5.5	0.3
Densely welded (middle of section)	57	13.5	5.41	22.6	3.6	13.1	5.51	21.5	3.8	0.53	1.231	3.9	-2.0
Moderately welded (middle of section)	6	17.5	1.59	20.1	15.8	17.2	2.16	21.4	15.4	0.37	1.268	1.9	-1.7
Non-welded (base of section)	15	33.9	5.64	40.4	23.9	28.9	5.30	38.7	20.0	7.02	2.610	10.8	1.3
All samples	106	21.2	10.88	45.0	3.6	19.8	10.05	44.8	3.8	1.92	2.729	10.8	-2.0

Table 8. Summary of density and calculated porosity values listed by component and welding intensity of the block and ash flow deposit.

Component/Welding Intensity		N	Bulk Density (g/cm³)		Skeletal Density (g/cm³)		Rock Density (g/cm³)		Total Porosity (%)		Connected Porosity (%)		Isolated Porosity (%)	
			Avg.	σ	Avg.	σ	Avg.	σ	Avg.	σ	Avg.	σ	Avg.	σ
Clasts	Non-welded	28	1.68	0.120	2.37	0.091	2.50	0.029	32.39	4.754	28.95	3.831	4.90	3.133
	Indurated	8	2.01	0.059	2.41	0.041	2.49	0.017	18.91	2.253	16.01	1.578	3.45	1.623
	Welded	11	2.34	0.035	2.46	0.022	2.48	0.026	5.35	1.070	4.79	0.992	0.98	1.071
Matrix	Non-welded	3	1.52	0.081	2.53	0.011	2.55	0.010	40.28	2.963	39.86	3.222	0.70	0.598
	Indurated	4	1.46	0.054	2.51	0.012	2.54	0.011	42.24	2.159	41.69	2.249	0.94	0.662
	Welded	46	2.13	0.082	2.52	0.029	2.54	0.025	16.63	2.954	16.29	3.031	0.39	1.261
Mixed	Welded	6	2.26	0.078	2.49	0.046	2.50	0.028	9.63	3.329	9.10	3.519	0.60	1.196
All samples		106	1.99	0.273	2.47	0.084	2.52	0.033	21.21	10.883	19.81	10.052	1.92	2.729

61

5.1. The 'Proto-deposit'

In order to relate variations in density and porosity to strain accumulated during welding, an estimate of the block and ash flow deposit properties when it was initially emplaced is required (e.g., prior to sintering and compaction). Our best estimate of this state derives from measurements on samples of the unconsolidated facies of the block and ash flow deposits (Table 5). A total of seven bulk samples from non-welded to incipiently welded facies were collected (Fig. 4d). Values of bulk densities (graduated cylinder technique) for the matrix vary by 15% between $1.39 - 1.59 \pm 0.057$ g/cm^3. Skeletal density, based on helium pycnometry, show less variation (1.5%), and range from $2.50 - 2.54 \pm 0.003$ g/cm^3. Lastly, the densities of powdered samples measured by helium pycnometry vary by less than 1% and return values between $2.53 - 2.55 \pm 0.006$ g/cm^3. From these three values of density, porosity can be inferred. The resulting values of total porosity for the non-welded/unconsolidated matrix range from $38 - 45 \pm 2.26\%$, where $37 - 45 \pm 2.27\%$ is connected, and $0.3 - 1.7 \pm 0.25\%$ is isolated. The average values of $\Phi_T = 41.4\%$, $\Phi_C = 40.9\%$, and $\Phi_I = 0.85\%$ are used as a baseline for subsequent calculations and analysis on matrix samples of block and ash flow deposit.

Large clasts sampled from the unconsolidated and incipiently welded facies were also sampled to estimate original conditions of the block and ash flow deposit. Bulk density values (geometric volume technique) for clasts vary 26%, ranging from $1.50 - 1.89 \pm 0.020$ g/cm^3. Skeletal density based on helium pycnometry shows less variation (13%), and ranges from $2.24 - 2.52 \pm 0.007$ g/cm^3. Lastly, the densities of powdered samples measured by helium pycnometry vary by 5% and return values of $2.46 - 2.59 \pm 0.009$ g/cm^3. From these three values of density, porosity

62

can be inferred. The values of total porosity for these non-welded/unconsolidated clasts range from $24 - 40 \pm 4.75\%$, where $19 - 34 \pm 3.83\%$ is connected, and $0 - 12 \pm 3.48\%$ is isolated. The average values of $\Phi_T = 32.4\%$, $\Phi_C = 28.9\%$, and $\Phi_I = 5.26\%$ are used as a baseline for subsequent calculations and analysis of clasts belonging to the block and ash flow deposit at Mount Meager.

5.2.   Bulk Density

Bulk densities were calculated for all 106 samples, representing the full welding spectrum of the deposit. They were calculated in order to determine the overall sample density (including all its porosity), and how it varies throughout the welding facies (Table 6), as well as how it varies between components of the block and ash flow deposit (Fig. 24a; Table 8). Bulk density values, in combination with other density measurements, are also used in obtaining total porosity values (Tables 7, 8).
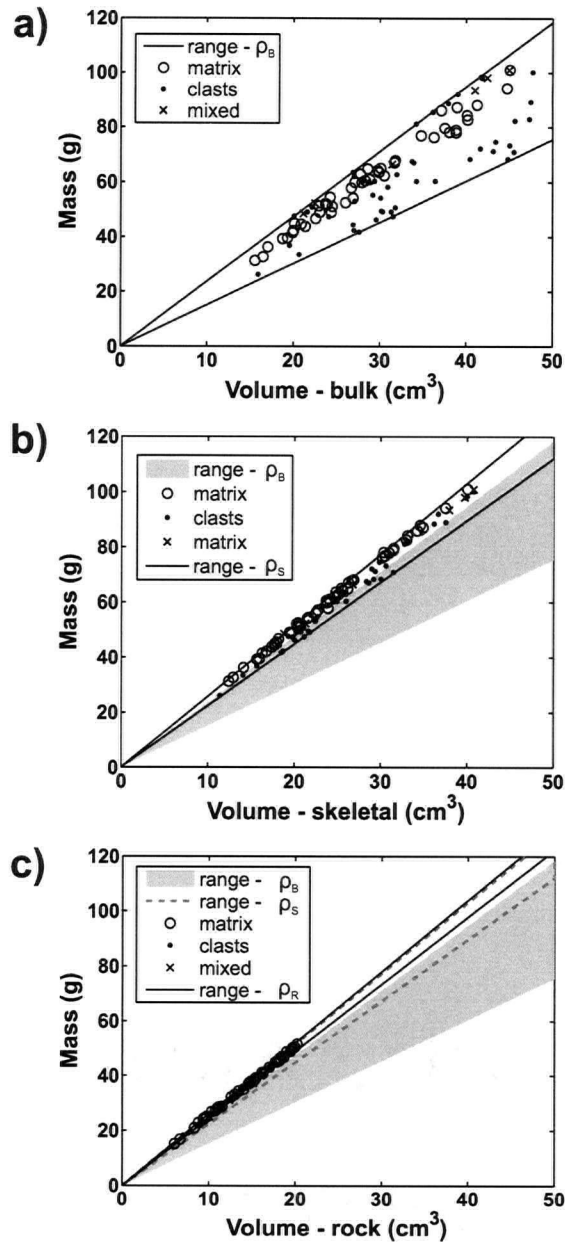
Figure 24: Mass-volume plots for all samples showing total ranges of: **(a)** bulk density (ρ_B), **(b)** skeletal density (ρ_S), and **(c)** rock density (ρ_R) for clasts (solid circle), matrix (open circles), and mixed samples (x's). In each case, the minimum and maximum densities are represented by solid lines. Grey shaded regions in **(b)** and **(c)** represent the range in bulk density shown in **(a)**. Dashed line in **(c)** represents the variation in skeletal density. In **(a)**, clasts show a wide range of bulk densities, but they are generally lower than the matrix. The matrix shows a tighter but higher overall range in bulk density. In **(b)**, the same pattern is observed, except ranges of skeletal density are much smaller than the ranges in bulk density. The range of rock powder densities seen in **(c)** is extremely narrow, and is independent of componentry.

64

5.2.1. Non-welded vs. Welded

Distinct variations in bulk density exist between non-welded and welded facies of the block and ash flow deposit. An average of fifteen basal non-welded samples resulted in a bulk density of 1.64 ± 0.126 g/cm^3. Sixteen upper non-welded samples averaged a bulk density of 1.70 ± 0.122 g/cm^3. The incipiently welded facies shows a slight increase in bulk density, but are more variable, averaging 1.83 ± 0.275 g/cm^3 for twelve samples. Six samples of a moderately welded block of material revealed a significantly higher average bulk density of 2.08 ± 0.041 g/cm^3, whereas the densely welded samples (N = 57) had the highest average with 2.19 ± 0.113 g/cm^3. Total porosity is inversely related to bulk density. The basal non-welded section contains an average total porosity of $33.9 \pm 5.64\%$, whereas the upper, non-welded section averages only slightly less at $32.7 \pm 4.88\%$. The incipiently welded facies maintains a total porosity of $27.4 \pm 11.96\%$. Moderately welded samples show a much lower total porosity of $17.6 \pm 1.59\%$, and the densely welded samples have the lowest porosity at $13.5 \pm 5.41\%$.

5.2.2. Clasts vs. Matrix

As with the trends seen in the different facies of the block and ash flow deposit, the bulk density trends between clasts and matrix are the most distinctive. Both clasts and matrix show an increase in bulk density as welding intensifies. Average clast density progresses from 1.68 ± 0.120 g/cm^3 (non-welded) to 2.01 ± 0.059 g/cm^3 in the incipiently welded facies, and finally to 2.34 ± 0.035 g/cm^3 for the welded facies. The matrix begins with a bulk density of 1.52 ± 0.081 g/cm^3, averages 1.46 ± 0.054 g/cm^3 where incipiently welded, and ends with a welded bulk

density of 2.13 ± 0.082 g/cm^3. Mixed samples reveal an intermediate welded density of 2.26 ± 0.078 g/cm^3. Total porosity again mirrors bulk density with an inverse relationship. Non-welded clasts start with an average total porosity of $32.4 \pm 4.75\%$, decreasing to $18.9 \pm 2.25\%$ where incipiently welded, and finally decrease to $5.35 \pm 1.070\%$ where they have become densely welded. The matrix contains $40.3 \pm 2.96\%$ total porosity when non-welded, and remains similar at $42.2 \pm 2.16\%$ where incipiently welded, but decreasing to $16.6 \pm 2.95\%$ in the densely welded facies. Mixed samples show an intermediate average total porosity of $9.63 \pm 3.329\%$ where welded.

5.3. Skeletal Density

Skeletal density has been measured by helium pycnometry on all 106 samples in order to determine the amount of connected porosity in the samples, and how it varies throughout the deposit and its components (Tables 5, 7). Overall, values of skeletal density are much higher than the values obtained for bulk density (Fig. 24b).

5.3.1 Non-welded vs. Welded

Much less variation in skeletal density is observed when comparing non-welded and welded facies of the block and ash flow deposit. Basal non-welded samples resulted in a skeletal density of 2.31 ± 0.069 g/cm^3, and averaged $28.9 \pm 5.30\%$ connected porosity. The upper non-welded samples had an average skeletal density of 2.46 ± 0.061 g/cm^3 with a connected porosity of $31.0 \pm 4.76\%$. The incipiently welded facies shows a similar average skeletal density of 2.44 ± 0.062

g/cm^3, but has a corresponding connected porosity of $25.4 \pm 13.07\%$. The large variation in this section is largely due to the presence of dense clasts, which represent only a small proportion of this facies. The basal section is therefore distinct from the upper non-welded to incipiently welded sections in terms of skeletal density, but not in terms of connected porosity. The moderately welded and densely welded samples show near identical values of 2.52 ± 0.030 g/cm^3 and 2.51 ± 0.040 g/cm^3, respectively. Connected porosity values are similar, with an average of $17.2 \pm 2.16\%$ for the moderately welded samples, and $13.1 \pm 5.51\%$ for the densely welded samples. Therefore, the upper non-welded facies of block and ash flow deposit has the most connected porosity, and, as expected, the densely welded intermediate facies retains the least amount of connected porosity. In addition, there is a general increase in skeletal density and decrease in connected porosity as welding progresses.

5.3.2. Clasts vs. Matrix

Both the clast and matrix components show very little variation in skeletal density despite their transition from the non-welded to the densely welded state. Clasts show a small increase in skeletal density as welding intensifies, but this increase is small relative to analytical uncertainty. Clasts, on average, have a starting skeletal density of 2.37 ± 0.091 g/cm^3 in the non-welded facies, which increases slightly to 2.41 ± 0.041 g/cm^3 in the incipiently welded section, and finally to a skeletal density of 2.46 ± 0.022 g/cm^3 where welded. Matrix samples show minute variations that are also within measurement error. The non-welded matrix has an average skeletal density of 2.53 ± 0.011 g/cm^3, averages 2.51 ± 0.012 g/cm^3 when incipiently welded, and ends with a welded skeletal density of 2.52 ± 0.082 g/cm^3. Mixed samples reveal an

67

intermediate skeletal density of 2.49 ± 0.046 g/cm^3 when welded. Connected porosity shows a more significant change as the components become welded. Non-welded clasts start with an average connected porosity of 29.0 ± 3.83%, decreasing to 16.0 ± 1.58% when incipiently welded, and are reduced to 4.79 ± 0.992% once the clasts have undergone welding. The matrix contains 39.9 ± 3.22% connected porosity when non-welded, stays fairly constant at 41.7 ± 2.25% when incipiently welded, and finishes off at 16.3 ± 3.03% when welded. Mixed samples show an intermediate average connected porosity of 9.10 ± 3.519% when welded. Note that values of total porosity and connected porosity for the matrix samples are very similar.

5.4.   Rock Powder Density

Rock powder density is the final step in characterizing the physical properties of the Mount Meager block and ash flow deposit, and is important in confirming the presence of isolated porosity. Overall observations reveal there is a further reduction in range for rock powder density, as we are measuring the rock only (i.e., accounting for all pore space) (Fig. 24c). This should remain constant throughout a deposit unless there is a geochemical or crystal content change during its eruption from the source.

5.4.1. Non-welded vs. Welded

Values of rock powder density for all facies show very little variation, and on average, range from 2.49 ± 0.040 g/cm^3 to 2.53 ± 0.040 g/cm^3 in the basal non-welded and moderately welded facies, respectively. The powder pycnometry does, however, confirm the presence of isolated

porosity. The basal non-welded facies contains the highest average isolated porosity, with $7.02 \pm 2.610\%$. The upper non-welded facies possesses $2.38 \pm 1.953\%$ isolated porosity, whereas the incipiently welded facies possess $2.54 \pm 1.821\%$. The welded facies contain little to no isolated porosity, with values of $0.53 \pm 1.231\%$ and $0.37 \pm 1.268\%$ for the moderately and densely samples, respectively. Therefore, there is a general decrease in isolated porosity with increasing welding intensity.

5.4.2. Clasts vs. Matrix

Clasts and matrix are nearly indistinguishable from each other on the basis of the results of powder pycnometry. Clasts, on average, range from 2.48 ± 0.026 g/cm^3 to 2.50 ± 0.029 g/cm^3 regardless of their welding intensity. Matrix samples show minute variations within analytical uncertainty, but are slightly denser than the clasts. The matrix has an overall average rock powder density of 2.54 ± 0.025 g/cm^3 to 2.55 ± 0.010 g/cm^3. Mixed samples contain a similar rock powder density of 2.50 ± 0.028 g/cm^3. Isolated porosity shows a slightly more evident trend. Non-welded clasts start with an average isolated porosity of $4.90 \pm 3.133\%$, decreasing slightly to $3.45 \pm 1.623\%$ when incipiently welded, and end up with $0.98 \pm 1.071\%$ isolated porosity (essentially none) once the clasts have been densely welded. The matrix and mixed samples all demonstrate average isolated porosities of less than 1%.

CHAPTER SIX

DISCUSSION

The aim of this study is to document the welding trajectory of the Keyhole Falls Member and recover the conditions and mechanism(s) under which this unique deposit formed. In previous chapters, I have described a welded block and ash flow deposit and presented data collected from field mapping, petrography, image analysis, SEM analysis and physical property measurements. In this chapter, those data sets and observations are used to: (a) document the welding process at Mount Meager, (b) discern the mechanism(s) involved, and (c) calculate the amount of strain accommodated by the deposit. This chapter will also compare the welding process as evidenced in the Keyhole Falls Member against welding features commonly found in ignimbrites.

6.1 Analysis of Porosity

Welding intensity is evaluated relative to the original properties in the non-welded block and ash flow deposit. These properties are represented by physical property measurements on the unconsolidated facies of the Keyhole Falls Member. Non-welded clasts reveal an initial bulk density of $1.50 - 1.89 \pm 0.020$ g/cm^3; given a rock powder density of 2.50 ± 0.029 g/cm^3, this corresponds to a total porosity of $24 - 40 \pm 4.75\%$. Non-welded matrix shows an initial bulk density of $1.39 - 1.59 \pm 0.057$ g/cm^3; given a rock powder density of 2.55 ± 0.010 g/cm^3, this corresponds to a porosity range of $38 - 45 \pm 2.26\%$.

Porosity can be further broken down into two categories: isolated and connected. The presence of isolated porosity is first demonstrated in Figure 25a, in which connected porosity is plotted against bulk density. The y-intercepts in this plot represent the range in skeletal density (2.24 – 2.57 g/cm^3) if there is no isolated porosity. The maximum y-intercept corresponds to a reasonable value; however, the minimum y-intercept is much lower than the density of the rock (2.49 – 2.53 g/cm^3). It can therefore be inferred that isolated porosity is the cause of the lower density samples. Rock powder pycnometry confirms this hypothesis, as illustrated in Figure 25b, in which rock powder density is plotted against skeletal density for all samples. Samples plotting below the 1:1 line, and outside the 95% confidence limits represent samples with apparent isolated porosity. It is further reinforced by a plot of total porosity *vs.* connected porosity (Fig. 25c), whereby several samples demonstrate total porosities greater than their connected porosities.

In terms of block and ash flow componentry, minimal isolated porosity exists in the matrix (<1.65%), regardless of welding intensity; most is connected (Fig. 25d). Overall, the matrix experiences a ~24% reduction in porosity, from the non-welded to the densely welded facies of the block and ash flow deposit. The implication is that as the deposit undergoes compaction during welding, the original interstitial gas contained within matrix porosity was allowed to escape out of the deposit and, thus, the matrix of the deposit maintained connected pathways (e.g., permeability) until the very end of welding.

Clasts contain mostly connected porosity (up to 40%); however, up to 12% isolated porosity exists in the more porous non-welded clasts (Fig. 25d). On average, both types of porosity are drastically reduced during the welding process: connected porosity is reduced to 5% and isolated

71

porosity is reduced to 1% in the dense, vitrophyric clasts. This is unforeseen, as it was expected that compaction and welding would cut off existing connected porosity pathways and create isolated porosity, and the same effect would be observed in the matrix. Thus, there must be additional processes acting upon these deposits causing isolated pores to collapse. For isolated porosity to collapse, however, is slightly more complicated because there are no existing gas escape pathways. As compaction and welding proceed, isolated pores could become connected by cracks forming within the deposit that are created mechanically during compaction. Alternatively, they could be infinitely flattened, due to pure shear strain. Another possibility is that the volatiles may be resorbed back into the glass rather than escaping from the compacting block and ash flow deposit (Sparks et al., 1999). This occurs when the isolated pore pressures remain high despite the deposit as a whole having degassed subsequent to eruption. This would create a pressure gradient, possibly allowing the gas to dissolve back into the viscously deforming deposit, and the empty pores to collapse.
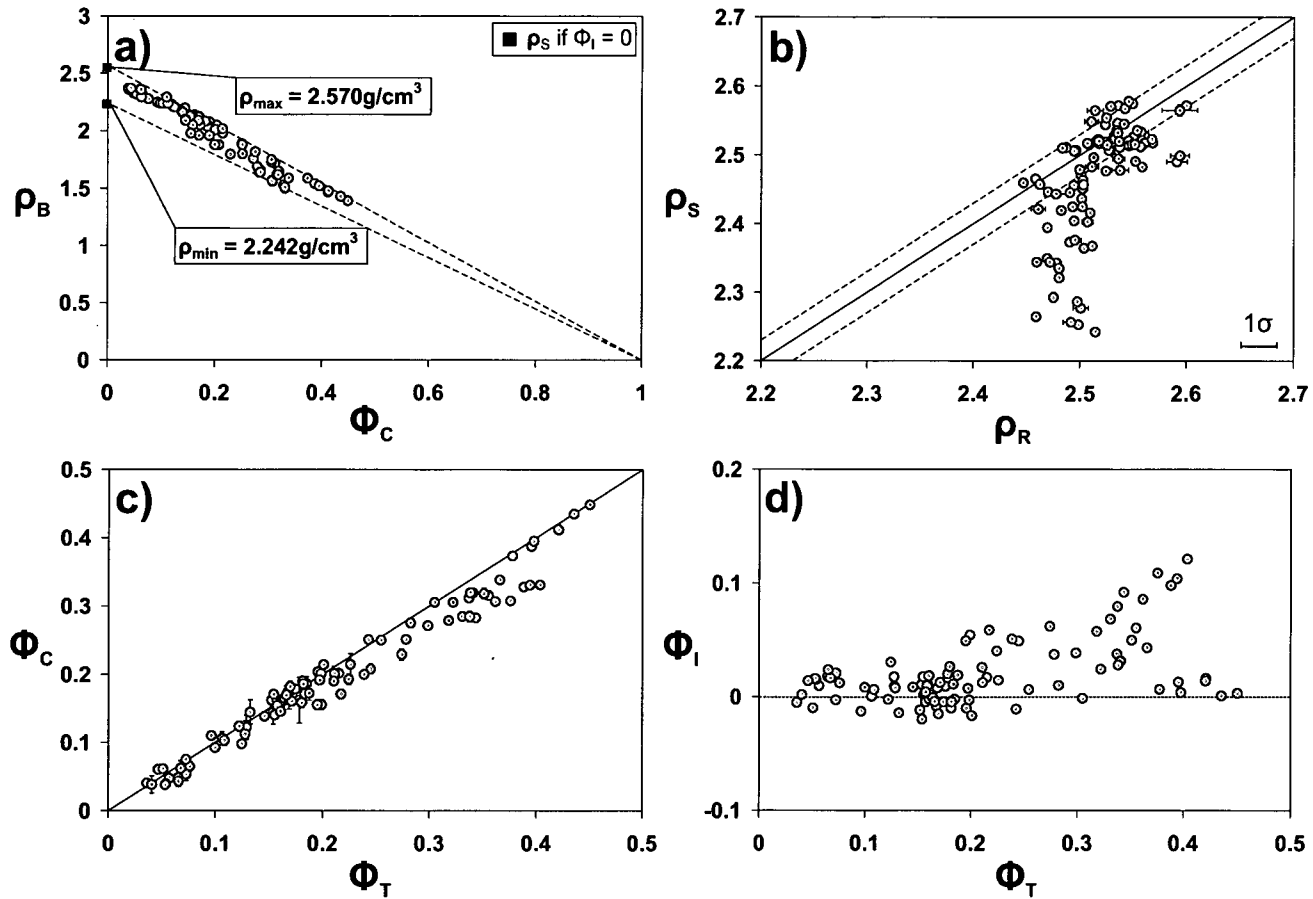
Figure 25: Plots of physical properties including: **(a)** connected porosity (Φ_C) *vs.* bulk density (ρ_B); y-intercepts define minimum and maximum values of density where there is no isolated porosity (Φ_I); **(b)** Rock powder density (ρ_R) plotted *vs.* skeletal density (ρ_S). Samples with no isolated porosity plot on the 1:1 line (solid line); samples with isolated porosity plot below the line ($\rho_R > \rho_S$). 95% confidence limits on 1:1 line are also shown as dashed lines; **(c)** Total porosity (Φ_T) *vs.* connected porosity (Φ_C). Samples lying below the 1:1 line (solid line) have isolated porosity represented by the vertical or horizontal distance to the 1:1 line; **(d)** Isolated porosity (Φ_I) *vs.* total porosity (Φ_T), showing that the isolated porosity content is positively correlated to total porosity.

6.2 Welding Mechanisms

Physical property measurements demonstrate that porosity decreases with increasing welding intensity. This decrease in porosity can be used to compute strain. The strain estimate is the total strain if all strain is volume strain (e.g., no shear strain) or is a minimum estimate of total strain if there is appreciable shear strain (e.g., constant volume strain). Quane and Russell (2006) use the original and final values of porosity to define total strain as:

$$\varepsilon_T = \frac{\Phi_o - \Phi_f}{1 - \Phi_f} \tag{6}$$

where it is assumed that (a) all strain is accommodated by porosity reduction, and (b) clasts and matrix each have a single starting porosity (40% and 45%, respectively). A plot of total strain *vs.* total porosity can be used to examine how porosity is affected by an increasing welding intensity, and can reveal how individual components accommodate strain. The resulting graph reveals two key aspects of the welding process occurring at Mount Meager (Fig. 26). First, clasts and matrix show parallel pathways with increasing strain (e.g., welding intensity). It therefore appears as though both components are simultaneously losing porosity at the same rate. This is contrary to observations of Sheridan and Ragan (1972) who state that pumiceous clasts in ignimbrites deform more rapidly than the surrounding matrix due their low relative viscosities and high initial porosities. Ross and Smith (1961) also observed that glass viscosity is very sensitive to volatile content and that pumice clasts in ignimbrite appear to retain a higher proportion of volatiles than the particulate ash.
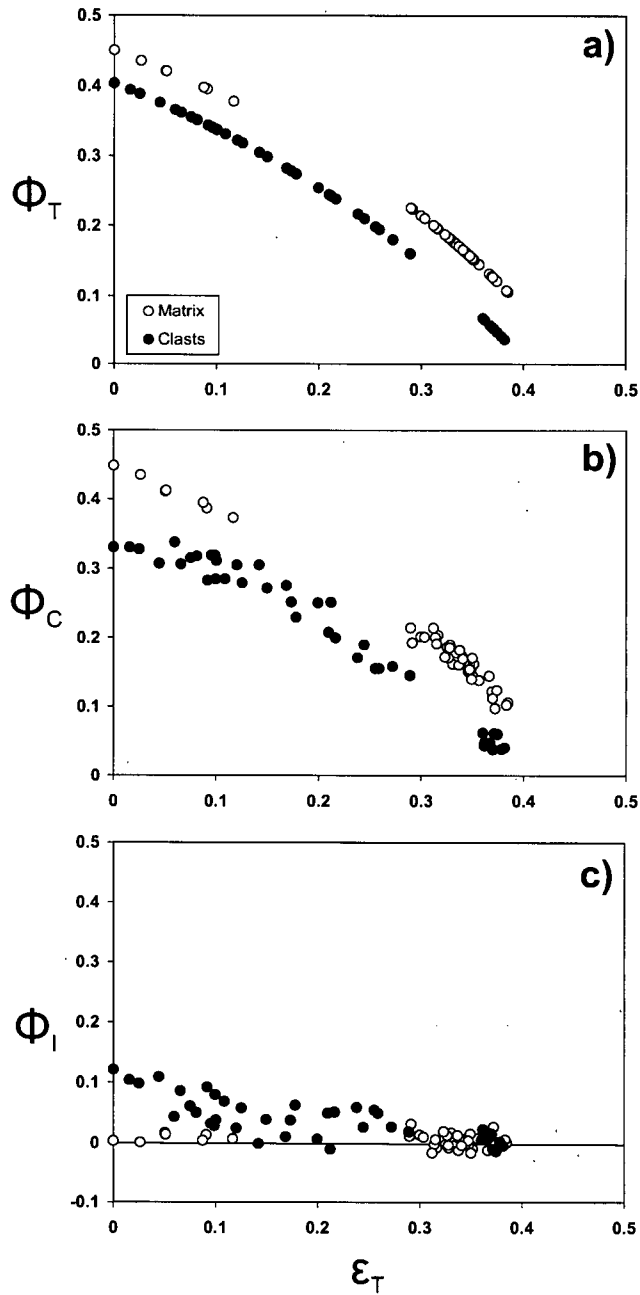
Figure 26: Values of calculated total strain ($\varepsilon_T = \Phi_o - \Phi_f/1 - \Phi_f$) are plotted *vs.* **(a)** observed total porosity (Φ_T), **(b)** observed connected porosity (Φ_C), and **(c)** observed isolated porosity (Φ_I) for clasts (closed circles) and matrix (open circles). Values of ε_T are calculated assuming: (i) all strain is due to volume loss, and (ii) clasts and matrix each had a single starting porosity (40% and 45%, respectively).

Second, both clasts and matrix record the same amount of maximum total strain, approximately 38%. This value correlates well with the empirical experiments presented in chapter 3.2.1, where the most welded FTM appears to have accumulated 30 – 40% volume strain. Also, the change in particle shape is fully consistent with volume strain. In other words, values of oblateness are low enough that they can be fully accounted for by volume strain, and a pure shear strain component need not be invoked. Thus it appears that the maximum amount of strain accommodated by the welded block and ash flow deposit at Mount Meager can be expressed as ~38% volume strain. This was expected because there is little evidence supporting other welding mechanisms. Mechanical deformation is not observed nor expected because the subsequent outburst flood event produced hot blocks of densely welded block and ash flow deposit. Pure shear strain in the viscous regime would produce a change in the radial dimensions of clasts; however, this is not evident when examining outcrop in the plane of flattening, where pure shear strain would produce a higher oblateness. Little other evidence is seen except rare pull-apart clasts or local deformation around lithics (e.g., clasts of Plinth assemblage) (Fig. 27). This localization likely results from small areas losing all or most of their porosity before the rest of the deposit, thus having to resort to a form of constant volume strain to deform further. Because values of strain correlate well between empirical experiments and physical property measurements, and manifestations of shear strain are localized, it can be deduced that viscous volume strain is the dominant mechanism in welding the block and ash flow at Mount Meager.
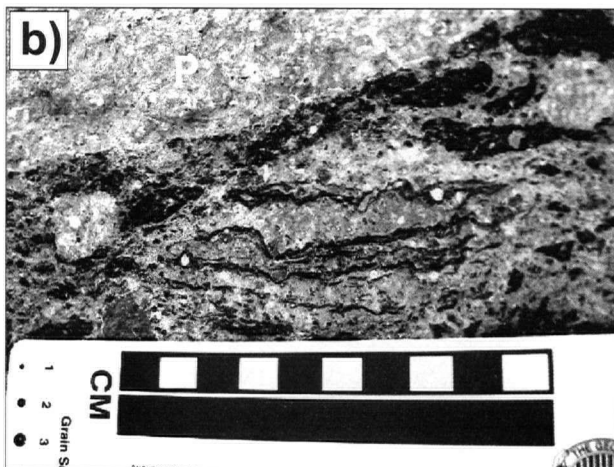
Figure 27: Uncommon textures indicating minimal effects of shear strain: **(a)** glassy pull-apart clast; **(b)** extreme flattening of glassy clasts near a lithic Plinth clast (P).

6.3 Original Thickness and Average Strain Calculations

The strain calculations depicted in Figure 26 can also be used to determine the deposit thickness prior to welding, as well as the average strain over the entire deposit. According to Stewart (2002), there is roughly 20 m of alluvial deposits, and 20 m of rock avalanche deposits overlying the welded block and ash flow deposits (Fig. 2a). Overlying these non-volcanic deposits is a further 60 m of non-welded to incipiently welded block and ash flow deposits. Because the deposits are not stratigraphically comfortable, only the lower section will be used in this calculation. The lower section is currently a total of 112 m at Keyhole Falls, which can be broken down into thicknesses of the three individual welding facies distinguished in section 2.3: (1) 10 m of basal non-welded facies, (2) 90 m of densely welded facies, and (3) 12 m of incipiently welded facies. Values of strain calculated using equation 6 are then averaged over the three welding facies to produce a strain profile (Fig 28). The facies thicknesses and average strain values are then combined to give an estimate of the original deposit thickness using the formulae below (Quane and Russell, 2005a).
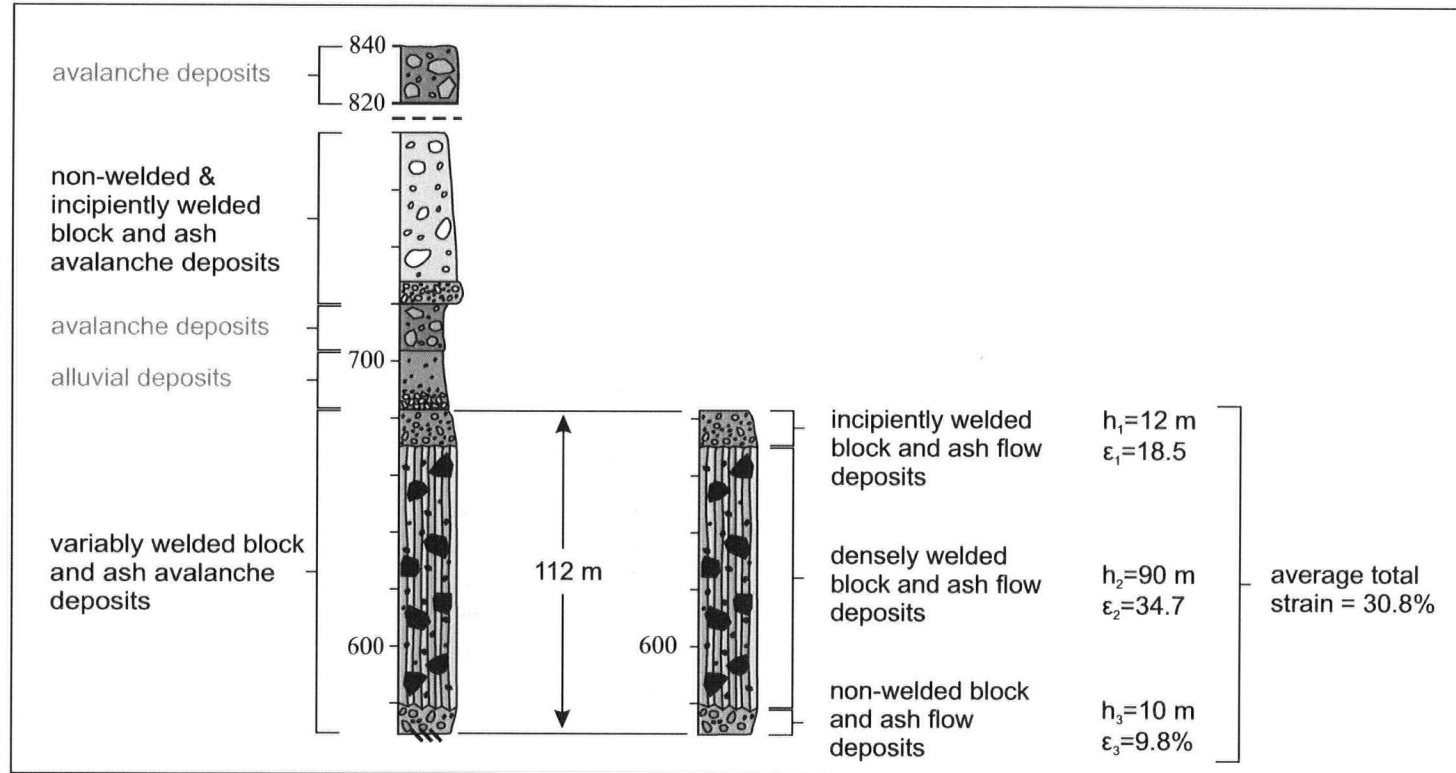
Figure 28: Strain profile of the lower welded block and ash flow deposits at Mount Meager, southwestern British Columbia, based on the stratigraphy of Stewart (2002). Only the lower section was used for the calculations due to the avalanche and alluvial deposits separating the upper and lower block and ash flow deposits. A total of 112 m of block and ash flow deposits exists in the lower section, consisting of: i) 12 m of incipiently welded deposits with an average strain of 19%; ii) 90 m of densely welded deposits with an average total strain of 35%; and, iii) 10 m of basal, non-welded block and ash flow deposits bearing an average total strain of 10%. Using the procedure followed in Quane and Russell (2005a), these values correspond to an overall average total strain of 31%.

First, the component of strain contributed by each welding facies (E_i) must be calculated:

$$E_i = \left(\frac{h_i}{\sum h} \right) \times \varepsilon_i \qquad (7)$$

The sum of these four strain components yields the average total strain (E_T) accommodated by the deposit as a whole:

$$E_T = \sum_i E_i \qquad (8)$$

This equation returns an average total strain of ~31% for the Keyhole Falls Member. In comparison, the Bishop Tuff in California yields an average total strain of 43%, the Bachelor Mountain Tuff yields 46%, and the Therasia welded tuff yields an average of 45% total strain (Quane and Russell, 2005a). Thus, the average strain value obtained for the Keyhole Falls Member is much lower than values obtained for welded ignimbrites.

Assuming that strain is represented by the ratio of change in thickness to the original thickness of the deposit, the original thickness of the Keyhole Falls Member can be determined:

$$L_o = \frac{L_{observed}}{1 - E_T} \qquad (9)$$

It is estimated that the original thickness at Keyhole Falls was ~162 m, meaning that welding and compaction reduced the block and ash flow deposit by 50 m.

6.4 Comparison to Other Volcanic Deposits

Physical properties of the Keyhole Falls Member sample suite provide a basis for comparing this welded block and ash flow deposit to other volcanic deposits. Below, porosity data for samples of the block and ash flow deposit at Mount Meager are compared to porosity data of: (a) pumices from the Pebble Creek Formation of Mount Meager, Lascar Volcano, Chile, and Soufriere Hills, Montserrat (Rust et al., 1999; Formenti and Druitt, 2003); (b) breadcrust bombs from Guagua Pichincha, Ecuador (Wright et al., 2007); (c) rhyodacite, andesite, and basalt lava flow deposits (Rust et al., 1999); (d) lava blocks from dome-collapse pyroclastic flow deposits at Soufriere Hills, Merapi, Cayambe, and Mount St. Helens (Formenti and Druitt, 2003); and (e) basalt scoria from Mauna Ulu (Rust et al., 1999). My comparison is based on total porosity (Φ_T), connected porosity (Φ_C), and isolated porosity (Fig. 29). Figure 29 shows plots of total porosity vs. connected porosity; the presence of isolated porosity is identified by points that plot below the 1:1 line. These data indicate that the values of total porosity cannot be fully explained by connected porosity.
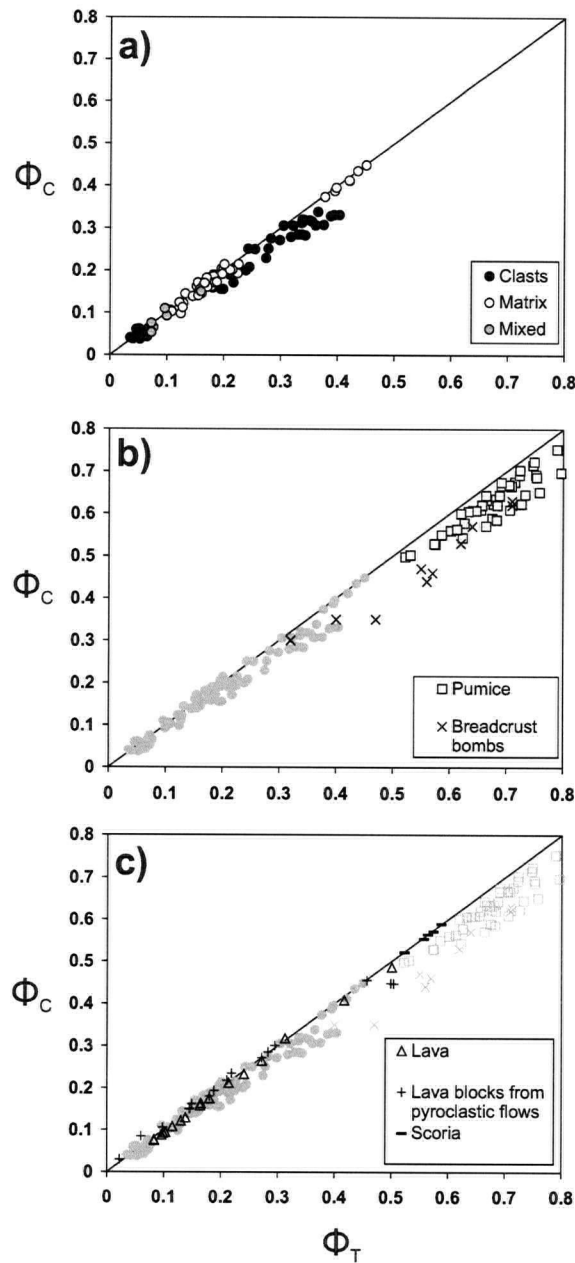
Figure 29: Plots of total porosity (Φ_T) *vs.* connected porosity (Φ_C) for: **(a)** Mount Meager block and ash flow deposits (clasts, matrix and mixed samples), **(b)** pumices (squares) from Mount Meager, Lascar Volcano, and Soufriere Hills (Rust et al., 1999; Formenti and Druitt, 2003), as well as breadcrust bombs (x's) from Guagua Pichincha (Wright et al., 2007), with block and ash deposits in grey, and **(c)** lava flow deposits (triangles) from Mount Meager, Ring Creek, and Cheakamus (Rust et al., 1999); lava blocks (pluses) from Soufriere Hills, Merapi, Cayambe, Mount St. Helens (Formenti and Druitt, 2003); and, scoria deposits (dashes) from Mauna Ulu (Rust et al., 1999), with Mount Meager block and ash flow deposits, pumices, and breadcrust bombs in grey.

82

Samples from the matrix from the Mount Meager block and ash flow deposits contain negligible isolated porosity (Fig. 29a). In contrast, the blocks within the deposit contain up to 12% isolated porosity. The maximum value of isolated porosity is found in the non-welded to incipiently welded facies, in which clasts contain 20 – 40% total porosity. However, as welding proceeds, that isolated porosity is destroyed along with most of the connected porosity. Pumice from Mount Meager, Lascar Volcano, and Soufriere Hills develop a maximum of 11% isolated porosity, but possess 52 – 75% total porosity (Fig. 29b). Breadcrust bombs from Guagua Pichincha have total porosities of 32 – 71%, and develop up to 12% isolated porosity when total porosity values are a minimum of 40% (Fig. 29b). Thus, the block and ash flow deposits at Mount Meager develop an isolated porosity at lower total porosities than typical pumices or breadcrust bombs.

With the exception of one location (Mount St. Helens), lava flow deposits, lava blocks from dome-collapse pyroclastic flow deposits and scoria deposits show no development of isolated porosity. Despite their broad range in total porosities (2 – 59%), only deposits from a disrupted cryptodome blast deposit at Mount St. Helens show any departure from the 1:1 line (up to 5% isolated porosity, with total porosities ~50%) (Fig. 29c). Thus, block and ash flow deposits at Mount Meager develop isolated porosities when lava flow deposits and dome-collapse pyroclastic flow deposits of similar densities fail to do so.

These trends in porosity can be explained by bubble nucleation events occurring prior to eruption. All pumice samples from fountain-collapse pyroclastic flows possess an isolated porosity, as do the non-welded to incipiently welded clasts from the block and ash flow deposits at Mount Meager. Blocks from dome-collapse pyroclastic flows only contain connected

83

porosity, and cryptodome blast samples from Mount St. Helens show a small amount of isolated porosity. Upon examination of samples under the SEM, Formenti and Druitt (2003) observe two populations of bubbles in the pumice samples: i) populations of large, connected vesicles, and ii) populations of small, isolated vesicles. There is no such distinction in porosity in the dome-collapse samples. As a result, it appears that fountain-collapse deposits undergo two nucleation events prior to eruption. The first population nucleates, grows and coalesces as the magma ascends in the conduit. The second population forms during a depressurization event just before erupting, when the magma is still above its glass transition temperature, producing smaller, isolated vesicles. Rapid quenching of the pumice as it is ejected from the volcanic edifice prevents the small isolated vesicles from coalescing. Dome-collapse deposits result from the gradual growth of a dome fueled by ascending magma, which possesses a population of bubbles that have nucleated, grown and coalesced as magma rises in the conduit. Given that domes are exposed to the external environment, they are commonly chilled below their glass transition temperatures. Thus, they may undergo depressurization prior to failure, but cannot produce a second population of vesicles. A cryptodome, however, forms below the surface, and can remain above its glass transition. A depressurizing event causing its exposure could cause a second nucleation event producing small isolated vesicles as measured by Formenti and Druitt (2003) at Mount St. Helens (Fig. 29).

The non-welded to incipiently welded clasts in the block and ash flow deposits possess significant isolated porosity; hence, it can be deduced that a depressurizing event occurred just prior to eruption, causing a population of small isolated vesicles to form. This signifies that the eruption at Mount Meager is not likely a Merapi-type eruption as previously thought, because the deposits would not have erupted above their glass transition temperature. The most likely

analogue is that of Soufrière Hills, Montserrat, where hot, explosive dome-collapse is triggered by a Vulcanian eruption. The presence of breadcrust bombs in the incipiently welded facies also supports this hypothesis (Wright et al, 2007). Furthermore, this eruption produced a block and ash flow that was also above its glass transition temperature such that it could undergo dense welding in the viscous regime.

CHAPTER SEVEN

CONCLUSIONS

Excellent outcrops and exposures at Mount Meager provide an opportunity to study a unique, welded block and ash pyroclastic flow deposit. Texture mapping and image analysis at two scales were completed as independent and objective means of quantifying the change in fabric and flattening of particles in the Keyhole Falls Member. Results indicate the following:

- Image analysis of FTMs demonstrate a welding trajectory whereby average oblateness increases and average orientation decreases with increasing welding intensity.

- This welding trajectory is more subtle than expected due to an original clast oblateness of approximately 30%; this results in an estimated maximum volume strain of 12% in the deposit or a maximum of 8% pure shear strain.

- Conversely, STMs show heterogeneity or strain localization in terms of average orientation and oblateness.

- An empirical experiment with image analysis reveals average oblateness does not reflect total volume strain for these deposits due to the original clast oblateness; however, the most welded FTMs visually correspond to experimental results having undergone a total volume strain of 30 – 40%.

- Distributions of oblateness and orientation for each FTM are more accurate in indicating welding intensity than average FTM values alone.

Petrography and SEM analysis were used to describe and identify micro-scale textures associated with the welding of the block and ash deposit. In addition, deposit components and porosity were examined to document the changes from non-welded to welded facies.

- Welding textures observed in thin section include: (a) visibly flattened clasts, (b) collapsed vesicles, (c) deformation around clasts/crystals, and (d) parallel alignment of clasts, clast length, and collapsed vesicles.

- Shards observed in the block and ash flow deposit are (in decreasing order from most abundant): (a) blocky, (b) bubble-wall, (c) platy, and (d) pumiceous.

- Porosity evolution can be documented using image analysis of SEM photos such that results correspond well to values obtained in physical property measurements.

Physical property measurements were used to elucidate the progression from non-welded to welded facies of the block and ash flow deposit. Using values of density and porosity, several inferences can be made regarding the welding process involving the 2360 B.P. eruption of the Keyhole Falls Member:

- Non-welded clasts reveal an original bulk density of $1.50 - 1.89 \pm 0.020$ g/cm^3, corresponding to a porosity of $24 - 40 \pm 4.75\%$. Non-welded matrix shows an original bulk density of $1.39 - 1.59 \pm 0.057$ g/cm^3, with a corresponding porosity of $38 - 45 \pm 2.26\%$.

- Both clasts and matrix record strain equally, unlike in ignimbrites whereby clasts accommodate more strain than the surrounding matrix.

- The maximum total (volume) strain accommodated by the deposit is approximately 38%.

- Isolated porosity exists in highly-porous, non-welded clasts only, and is reduced along with connected porosity during the welding process; possible vehicles for this are volatile resorption or connection of isolated porosity during compaction.

- Volume strain in the viscous regime is the dominant strain mechanism, reducing the original thickness of the Keyhole Falls Member by 50 m (from 162 – 112 m); this corresponds to an average of 31% volume strain over the entire deposit.

- Pure shear strain (constant volume) in the viscous regime is a minimal component, only occurring locally as pull-apart clasts or shearing in proximity to lithic clasts.

- Comparison of porosity data from other volcanic deposits demonstrates that the block and ash flow was most likely generated by an explosive dome collapse triggered by a Vulcanian event, as evidenced by the presence of isolated porosity in clasts, and the presence of breadcrust bombs of the block and ash flow deposit at Mount Meager.

REFERENCES

Abdurachman, E.K., Bourdier, J.-L., Voight, B., 2000. Nuées ardentes of 22 November 1994 at Merapi Volcano, Java, Indonesia. Journal of Volcanology and Geothermal Research 100, 345-361.

Anderson, R.G., 1975. The geology of the volcanics in the Meager Creek map-area, southwestern British Columbia. B.Sc. thesis, Department of Geological Sciences, The University of British Columbia.

Bardintzeff, J.M., 1984. Merapi Volcano (Java, Indonesia) and Merapi-Type Nuée Ardente. Bulletin of Volcanology 47, 433-446.

Barker, D.S., Nixon, P.H., 1983. Carbonatite lava and welded air fall tuff, Fort Portal field, Western Uganda. Eos, Transactions, American Geophysical Union 64, 896.

Boudon, G., Camus, G., Gourgaud, A., Lajoie, J., 1993. The 1984 nuée-ardente deposits of Merapi volcano, Central Java, Indonesia: stratigraphy, textural characteristics, and transport mechanisms. Bulletin of Volcanology 55, 327-342.

Bourdier, J.-L., Abdurachman, E.K., 2001. Decoupling of small-volume pyroclastic flows and related hazards at Merapi volcano, Indonesia. Bulletin of Volcanology 63, 309-325.

Boyd, F.R., 1961. Welded tuffs and flows in the rhyolite plateau of Yellowstone Park, Wyoming. Geological Society of America Bulletin 72, 387– 426.

Branney, M.J., Kokelaar, B.P., 1992. A reappraisal of ignimbrite emplacement: Changes from particulate to non-particulate flow during progressive aggradation of high-grade ignimbrite. Bulletin of Volcanology 54, 504-520.

Calder, E.S., Luckett, R., Sparks, R.S.J., Voight, B., 2002. Mechanisms of lava dome instability and generation of rockfalls and pyroclastic flows at Soufrière Hills Volcano, Montserrat. In: T.H. Druitt and B.P. Kokelaar (eds.), The Eruption of Soufrière Hills Volcano, Montserrat, from 1995-1999. Geological Society of London, Memoir 21, London, England.

Cas, R.A.F., Wright, J.V., 1987. Volcanic Successions; modern and ancient. Chapman and Hall, London, 528 p.

Clague, J.J., Evans, S.G., Rampton, V.N., Woodsworth, G.J., 1995. Improved age estimates for White River and Bridge River tephras, western Canada. Canadian Journal of Earth Sciences 32, 1172–1179.

Clague, J.J., Friele, P.A., Hutchinson, I., 2003. Chronology and hazards of large debris flows in the Cheekye River basin, British Columbia, Canada. Environmental and Engineering Geoscience 9(2), 99-115.

Cole, P.D., Calder, E.S., Sparks, R.S.J., Clarke, A.B., Druitt, T.H., Young, S.R., Herd, R.A., Harford, C.L., Norton, G.E. 2002. Deposits from dome-collapse and fountain-collapse pyroclastic flows at Soufrière Hills Volcano, Montserrat. In: T.H. Druitt and B.P. Kokelaar (eds.), The Eruption of Soufrière Hills Volcano, Montserrat, from 1995-1999. Geological Society of London, Memoir 21, London, England.

Cordy, P., 1999. Sedimentological evidence for the damming of the Lillooet River by the 2350 B.P. eruption of Mount Meager, Southern Coast Mountains, BC. B.Sc. Thesis, The University of British Columbia.

Evans, S., 1992. Landslide and river damming events associated with the Plinth Peak volcanic eruption, southwestern British Columbia; Geotechnical and Natural Hazards, BiTech Publishing, Vancouver, British Columbia, pp. 405-412.

Formenti, Y., and Druitt, T.H. 2003. Vesicle connectivity in pyroclasts and implications for the fluidization of fountain-collapse pyroclastic flows, Montserrat (West Indies). Journal of Volcanology and Geothermal Research 214, 561-574.

Gabrielse, H., Monger, J.W.H., Wheeler, J.O., Yorath, C.J., 1992. Tectonic framework; Part A, Morphogeological belts, tectonic assemblages and terranes. In: H. Gabrielse and C.J. Yorath (eds.), Geology of the Cordilleran Orogen in Canada. Geological Survey of Canada.

Giordano, D., Dingwell, D.B., Romano, C., 2000. Viscosity of a Teide phonolite in the welding interval. In: Marti J., Wolff, J.A. (eds.), The geology and geophysics of Tenerife. Elsevier.

Giordano, D., Nichols, A.R.L., Dingwell, D.B., 2005. Glass transition temperatures of natural hydrous melts: a relationship with shear viscosity and implications for the welding process. Journal of Volcanology and Geothermal Research 142, 105-118.

Gottsman, J., Dingwell, D.B., 2001. Cooling dynamics of spatter-fed phonolite obsidian flows on Tenerife, Canary Islands. Journal of Volcanology and Geothermal Research 105, 323–342.

Green, N.L., Armstrong, R.L., Harakal, J.E., Souther, J.G., Read, P.B., 1988. Eruptive history and K-Ar geochronology of the late Cenozoic Garabaldi volcanic belt, southwestern British Columbia. Geological Society of America Bulletin 100, 563-579.

Green, N.L., Sinha, A.K., 2005. Consequences of varied slab age and thermal structure on enrichment processes in the sub-arc mantle of the northern Cascadia subduction system. Journal of Volcanology and Geothermal Research 140, 107-132.

Guest, J.E., Rogers, P.S., 1967. The sintering of glass and its relationship to welding in ignimbrites. Proceedings of the Geological Society of London 1641, 174-177.

Hickson, C.J., Russell, J.K., Stasiuk, M.V., 1999. Volcanology of the 2350 B.P. Eruption of Mount Meager Volcanic Complex, British Columbia, Canada: implications for Hazards from Eruptions in Topographically Complex Terrain. Bulletin of Volcanology 60, 489-507.

Kano, K., Matsuura, H., Yamauchi, S., 1997. Miocene rhyolitic welded tuff infilling a funnel-shaped eruption conduit Shiotani, southeast of Matsue, SW Japan. Bulletin of Volcanology 59, 125– 135.

Karatson, D., Sztano, O., Telbisz, T., 2002. Preferred clast orientation in volcaniclastic mass-flow deposits: application of a new photo-statistical method. Journal of Sedimentary Research 72(6), 823-835.

Kelman, M.C., Russell, J.K., Hickson, C.J., 2002. Effusive intermediate glaciovolcanism in the Garibaldi volcanic belt, southwestern British Columbia, Canada. In: J.L. Smellie and M.G.

Chapman (eds.), Volcano-ice interaction on Earth and Mars, Geological Society Special Publications 202, 195-211, Geological Society of London.

Klug, C., Cashman, K.V., 1994. Vesiculation of May 18, 1980, Mount St. Helen's magma. Geology 22: 468-472.

Kobberger, G., Schmincke, H.U., 1999. Deposition of rheomorphic ignimbrite D (Mogan Formation) Gran Canaria, Canary Islands, Spain. Bulletin of Volcanology 60, 465– 485.

Kokelaar, P., Busby, C., 1992. Subaqueous Explosive Eruption and Welding of Pyroclastic Deposits. Science 257, 196-201.

Kokelaar, P., Königer, S., 2000. Marine emplacement of welded ignimbrite: the Ordovician Pitts Head Tuff, North Wales. Journal of the Geological Society, London 157, 517-536.

Mathews, W.H., 1958. Geology of the Mount Garibaldi map-area, southwestern British Columbia, Canada; Part 1, Igneous and metamorphic rocks; Part 2, Geomorphology and Quaternary volcanic rocks. Geological Society of America Bulletin 69(2), 161-198.

McPhie, J., Doyle, M., Allen, R., 1993. Volcanic Textures; a guide to the interpretation of textures in volcanic rocks. Centre for Ore Deposit and Exploration Studies, University of Tasmania, Australia, 196p.

Miyabuchi, Y., 1999. Deposits associated with the 1990 – 1995 eruption of Unzen volcano, Japan. Journal of Volcanology and Geothermal Research 89, 139-158.

Naranjo, J.A., Sparks, R.S.J., Stasiuk, M.V., Moreno, H., Ablay, G.J., 1992. Morphological, textural and structural variations in the 1988–1990 andesite lava of Lonquimay Volcano, Chile. Geological Magazine 129, 657–678.

Nasmith, H., Mathews, W.H., Rouse, G.E., 1967. Bridge River ash and some other recent ash beds in British Columbia. Canadian Journal of Earth Sciences 4, 163-170.

Peterson, D.W., 1979. Significance of the flattening of pumice fragments in ash flow tuffs. In: Chapin, C.E., Elston, W.E. (eds), Ash-flow tuffs. Special Paper, Geological Society of America.

Quane, S.L., Russell, J.K., 2005a. Ranking welding intensity in pyroclastic deposits. Bulletin of Volcanology 67, 129-143.

Quane, S.L., Russell, J.K., 2005b. Welding: insights from high-temperature analogue experiments. Journal of Volcanology and Geothermal Research 142, 67-87.

Quane, S.L., Russell, J.K., 2006. Bulk and particle strain analysis in high-temperature deformation experiments. Journal of Volcanology and Geothermal Research 154, 63-73.

Ragan, D.H., Sheridan, M.F., 1972. Compaction of the Bishop Tuff, California. Geological Society of America Bulletin 83, 95-106.

Read, P.B., 1977. Meager Creek volcanic complex, southwestern British Columbia. In: Report of Activities, Part A. Geological Survey of Canada Paper 77-1A.

Read, P.B., 1978. Geology of Meager Creek geothermal area, British Columbia. Geological Survey of Canada, Open File 603.

Read, P.B., 1990. Mount Meager Complex, Garibaldi Belt, Southwestern British Columbia. Geoscience Canada 17(3), 167-170.

Riehle, J.R., Miller, T.F., Bailey, R.A., 1995. Cooling, degassing and compaction of rhyolitic ash-flow tuffs: a computational model. Bulletin of Volcanology 57, 319-336.

Russell, J.K., Quane, S.L., 2005. Rheology of welding: inversion of field constraints. Journal of Volcanology and Geothermal Research 142, 173-191.

Russell, J.K., Stasiuk, M.V. 1997. Characterization of volcanic deposits with ground penetrating radar. Bulletin of Volcanology 58: 515-527.

Rust, A.R., Russell, J.K., Knight, R.J., 1999. Dielectric constant as a predictor of porosity in dry volcanic rocks. Journal of Volcanology and Geothermal Research 91, 79-96.

Rust, A.R., Russell, J.K., 2000. Detection of welding in pyroclastic flows with ground penetrating radar: insights from field and forward modeling data. Journal of Volcanology and Geothermal Research 95, 23-34.

Sato, H., Fujii, T., Nakada, S., 1992. Crumbling of dacite dome lava and generations of pyroclastic flows at Unzen volcano. Nature 360, 664-666.

Schipper, C.I., 2002. The catastrophic failure of a volcanic dam at Mount Meager, Southwest British Columbia., 2360 BP: an engineering approach to volcanic hazards. B.A.Sc. Thesis, The University of British Columbia.

Schmincke, H.U., Swanson, D.A., 1967. Laminar viscous flowage structures in ash-flow tuffs from Gran Canaria, Canary islands. Journal of Geology 75, 641– 664.

Sherrod, D.R., Smith, J.G., 1990. Quaternary extrusion rates of the Cascade Range, northwestern United States and southern British Columbia. Journal of Geophysical Research 95, 19645-19474.

Sheridan, M.F., Ragan, D.H., 1976. Compaction of ash-flow tuffs. In: G.V. Chilingarian and K.H. Wolf, (eds.), Compaction of coarse-grained sediments, II. Elsevier.

Smith, R.L., 1960a. Ash flows. Geological Society of America Bulletin 71(6), 795-841.

Smith, R.L., 1960b. Zones and zonal variations in welded ash flows. U.S. Geological Survey Professional Paper 354-F, 149–159.

Soriano, C., Zafrilla, S., Marti, J., Bryan, S., Cas, R., Ablay, G., 2002. Welding and rheomorphism of phonolitic fallout deposits from the Las Cañadas caldera, Tenerife, Canary Islands. Geological Society of America Bulletin 114(7), 883-895.

Sparks, R.S.J., Wright, J.V., 1979. Welded air-fall tuffs. In: Chapin, C.E., Elston, W.E. (eds.), Ash-Flow Tuffs. Special Paper, Geological Society of America 180, 155–166.

Sparks, R.S.J., Stasiuk, M.V., Gardeweg, M., Swanson, D.A., 1993. Welded breccias in andesite lavas. Journal of the Geological Society (London) 150, 897– 902.

Sparks, R.S.J., Tait, S.R., Yanev, Y., 1999. Dense welding caused by volatile resorption. Journal of the Geological Society of London 156, 217-225.

Stasiuk, M.V., Russell, J.K., Hickson, C.J., 1996. Distribution, nature, and origins of the 2400 BP eruption products of Mount Meager, British Columbia: linkages between magma chemistry and eruption behaviour. Geological Survey of Canada Bulletin 486.

Stewart, M.L. 2002. Dacite block and ash avalanche hazards in mountainous terrain: 2360 yr. BP eruption of Mount Meager, British Columbia. M.Sc. Thesis, The University of British Columbia.

Stewart, M.L., Russell, J.K., Hickson, C.J., 2003. Discrimination of hot versus cold avalanches: Implications for hazard assessment at Mount Meager, B.C. Natural Hazards and Earth System Science 3, 712-724.

Streck, M.J., Grunder, A.L., 1995. Crystallization and welding variations in a widespread ignimbrite sheet; the Rattlesnake Tuff, eastern Oregon, USA. Bulletin of Volcanology 57(3), 151-169.

Sumner, J.M, Blake, S., Matela, R.J., Wolff, J.A., 2005. Spatter. Journal of Volcanology and Geothermal Research 142, 49-65.

Tuffen, H., Dingwell, D.B., Pinkerton, H., 2003. Repeated fracture and healing of silicic magma generate flow banding and earthquakes? Geology 31, 1089–1092.

Ui, T., Suzuki-Kamata, K., Matsusue, R., Fujita, K., Metsugi, H., Araki, M., 1989. Flow behavior of large-scale pyroclastic flows; evidence obtained from petrofabric analysis. Bulletin of Volcanology 51(2), 115-122.

Ui, T., Matsuwo, N., Sumita, M., Fujinawa, A. 1999. Generation of block and ash flows during the 1990-1995 eruption of Unzen volcano, Japan. Journal of Volcanology and Geothermal Research 89, 123-137.

White, M.J., McPhie, J., 1997. A submarine welded ignimbrite-crystal-rich sandstone facies association in the Cambrian Tyndall Group, western Tasmania, Australia. Journal of Volcanology and Geothermal Reseach 76, 277-295.

Wilson, C.J.N., Hildreth, W., 2003. Assembling an ignimbrite: mechanical and thermal building blocks in the Bishop Tuff, California. Journal of Geology 111, 653–670.

Wolff, J.A., Sumner, J.M., 2000. Lava fountains and their products. In: Sigurdson, H. (Ed.), Encyclopedia of Volcanoes. Academic Press, pp. 321– 329.

Wolff, J.A., Wright, J.V., 1981. Rheomorphism of welded tuffs. Journal of Volcanology and Geothermal Research 10, 13–34.

Woods, A.W., Sparks, R.S.J., Ritchie, L.J., Batey, J., Gladstone, C., Bursik, M.I., 2002. The explosive decompression of a pressurized volcanic dome: the 26 December 1997 collapse and explosion of Soufrière Hills Volcano, Montserrat. In: T.H. Druitt and B.P. Kokelaar (eds.), The Eruption of Soufrière Hills Volcano, Montserrat, from 1995-1999. Geological Society of London, Memoir 21, London, England.

Wright, H., Cashman, K.V., Rosi, M., Cioni, R. 2007. Breadcrust bombs as indicators of Vulcanian eruption dynamics at Guagua Pichincha volcano, Ecuador. Bulletin of Volcanology 69(3), 281-300.

APPENDIX A

DETAILED DESCRIPTIONS OF FIELD TEXTURE MAPS

FIELD TEXTURE MAP #1
(Densely Welded Block and Ash Flow Deposit, Block #1, Field Site 1)

- Clast types:
    - o Black:
        - ▪ Glassy
        - ▪ Dense
        - ▪ Variably welded showing different shades of grey – black
        - ▪ Porphyritic, with (avg. 2 mm) phenos of plag/hbl/pyx (20-40%)
        - ▪ 95-98% of clasts
        - ▪ Subangular-subrounded
        - ▪ Some flow banding
        - ▪ Up to 1 m in diameter
    - o Light grey:
        - ▪ Partially welded pumiceous clasts (?)
        - ▪ Porphyritic, with (avg. 2 mm) phenos. of hbl/plag/pyx (<20%)
        - ▪ Subrounded
        - ▪ 1-3% of clasts
        - ▪ Up to 35 cm in diameter
    - o Flow banded:
        - ▪ Partially welded pumiceous clasts (?)
        - ▪ White and grey coloured
        - ▪ Porphyritic, with (avg. 1 mm) phenos. of plag/hbl/pyx (10-15%)
        - ▪ Subrounded, with wavy/irregular margins
        - ▪ 1% of clasts
        - ▪ Banding is wavy in nature
        - ▪ Up to 7 cm in diameter
    - o White/beige/light pink monzonite:
        - ▪ Medium-grained
        - ▪ Slightly weathered/altered
        - ▪ Subrounded
        - ▪ Small phenos. of plag (less than 1 mm)/qtz (avg. 1 mm)/pyx (avg. 1 mm) (<5%)
        - ▪ 1% of clasts
        - ▪ Less than 5 cm in diameter
- Overall clast shape: subrounded – subangular
- Overall clast size: variable, from 1 mm to ~1 m
- Matrix: Grey, fine-grained, ashy, also with fragments of the clasts listed above; oxidized in some areas
- Matrix supported, but locally nearly clast supported
- Sections with larger clasts mingled with sections of smaller clasts (different flow units? explosivity?)
- Some clasts appear to fit together (pull-aparts)
- Some clasts have rounded embayments, or tails
- Poorly sorted, no structure
- Clasts are elongated, mostly in the same direction – deformation/flattening due to welding & compaction

FIELD TEXTURE MAP #2
(Densely welded block and ash flow deposit, Block #3, Field Site 1)

- Clast types:
    - o Black:
        - ▪ Glassy
        - ▪ Dense
        - ▪ Variably welded showing different shades of grey – black
        - ▪ Porphyritic, with (avg. 2 mm) phenos of plag/hbl/pyx (<20%)
        - ▪ 95% of clasts
        - ▪ Subangular – subrounded
        - ▪ Some flow banding, at a maximum of 60o to fabric, but no preference to orientation
        - ▪ Up to 1 m in diameter
    - o Medium - light grey:
        - ▪ Partially welded pumiceous clasts (?)
        - ▪ Porphyritic, with (avg. 2 mm) phenos. of hbl/plag/pyx (<20%)
        - ▪ Subangular
        - ▪ Some flow banding at acute angles
        - ▪ 1% of clasts
        - ▪ Up to 15 cm in diameter
    - o Plinth clasts:
        - ▪ Medium grey
        - ▪ Porphyritic, with plag/qtz/some biot (<2%)
        - ▪ Irregular margins
        - ▪ Subrounded – subangular
        - ▪ 1-2% of clasts
        - ▪ Up to 20 cm in diameter
    - o White/beige/light pink monzonite:
        - ▪ Medium-grained
        - ▪ Slightly weathered/altered
        - ▪ Subrounded
        - ▪ Small phenos. of plag (less than 1 mm)/qtz (avg. 1 mm)/pyx (avg. 1 mm) (<5% mafic phenocrysts)
        - ▪ 1-2% of clasts
        - ▪ Up to 6 cm in diameter
- Overall clast shape: subrounded – subangular
- Overall clast size: variable, from 1 mm to ~1 m
- Matrix: Grey, fine-grained, ashy, also with fragments of the clasts listed above; oxidized in some areas
- Matrix supported
- More random size distribution than Block #1
- Some alignment of medium-sized clast sizes in the gridded area
- Preferred orientation/elongation of clasts
- Some very irregular shapes
- Poorly sorted, no structure

FIELD TEXTURE MAP #3
(Densely welded block and ash flow deposit (plane of flattening), Block #4,
Field Site 1)

- Clast types:
    - o Black:
        - ▪ Glassy
        - ▪ Dense
        - ▪ Variably welded showing different shades of grey – black
        - ▪ Porphyritic, with (avg. 2 mm) phenos of plag/hbl/pyx (<20%)
        - ▪ 85-90% of clasts
        - ▪ Subangular – subrounded
        - ▪ Up to 40 cm in diameter, but variable
    - o Dark grey #1:
        - ▪ Slate (?)
        - ▪ Microcrystalline
        - ▪ Subrounded
        - ▪ 1% of clasts
        - ▪ Up to 7 cm in diameter
    - o Grey #2:
        - ▪ Weathered Plinth? Partially welded pumiceous clasts?
        - ▪ Porphyritic, with small phenos. of plag/mafic minerals (biot?)
        - ▪ Subangular
        - ▪ 1% of clasts
        - ▪ Up to 7 cm in diameter
    - o Plinth clasts:
        - ▪ Light – dark grey
        - ▪ Porphyritic, with plag/qtz/some biot (<2%)
        - ▪ Irregular margins
        - ▪ Subangular
        - ▪ 5% of clasts
        - ▪ Up to 70 cm in diameter
    - o Black & white:
        - ▪ Granodiorite (?)
        - ▪ Subrounded
        - ▪ 1% of clasts
        - ▪ Up to 10 cm in diameter
    - o White/beige/light pink monzonite:
        - ▪ Medium-grained
        - ▪ Slightly weathered/altered
        - ▪ Subrounded
        - ▪ Small phenos. of plag (less than 1 mm)/qtz (avg. 1 mm)/pyx (avg. 1 mm) (<5% mafic phenocrysts)
        - ▪ 1-2% of clasts
        - ▪ Up to 15 cm in diameter, but variable
- Overall clast shape: subrounded – subangular
- Overall clast size: variable, from 1 mm to ~1 m
- Matrix: Grey, fine-grained, ashy, also with fragments of the clasts listed above (sometimes lone phenocrysts)
- Clasts are noticeably more rounded, for the most part, in the plane of flattening; some exceptions include small clasts in proximity to the edges of larger clasts

- Matrix supported
- Embayments in some clasts
- Several clasts are in contact with each other
- Slate clasts? They have a sheen indicative of fine-grained micas & contain a few phenos/porphyroblasts
- Flow banded clasts exist on the surface, but none present in mapped area; banding is inconsistent in orientation
- Some dense, glassy clasts appear very porphyritic like the Plinth clasts
- Inclusions in some dense clasts (?)

FIELD TEXTURE MAP #4
(Densely welded block and ash flow deposit, Block #4, Field Site 1)

- Clast types:
    - Black:
        - Glassy
        - Dense
        - Variably welded showing different shades of grey – black
        - Porphyritic, with (avg. 2 mm) phenos of plag/hbl/pyx (<20%)
        - 90-95% of clasts
        - Angular – rounded
        - Some flow banding, but difficult to see
        - Up to 40 cm in diameter, but mostly 5-15 cm
    - Grey:
        - Weathered Plinth? Partially welded pumiceous clasts?
        - Porphyritic, with small phenos. of plag/mafic minerals (biot?)
        - Subangular
        - Some flow banding
        - 3-5% of clasts
        - Up to 40 cm in diameter, but most 1-10 cm
    - White/beige/light pink monzonite:
        - Medium-grained
        - Slightly weathered/altered
        - Subrounded
        - Small phenos. of plag (less than 1 mm)/qtz (avg. 1 mm)/pyx (avg. 1 mm) (<5% mafic phenocrysts)
        - 1-2% of clasts
        - Up to 5 cm in diameter
- Matrix: Grey, fine-grained, ashy, also with fragments of the clasts listed above (sometimes lone phenocrysts)
- Matrix supported
- Surface is very weathered, making it difficult to distinguish clast types
- Clasts much more angular – even polygonal at times, but some are still very rounded
- Clasts don't appear particularly aligned or deformed, like lower down on the block surface
- Pull-aparts observed

FIELD TEXTURE MAP #5
(Densely welded block and ash flow deposit, Block #4, Field Site 1)

- Clast types:
    - o Black:
        - ▪ Glassy
        - ▪ Dense
        - ▪ Variably welded showing different shades of grey – black
        - ▪ Porphyritic, with (avg. 2 mm) phenos of plag/hbl/pyx (<20%)
        - ▪ 90-95% of clasts
        - ▪ Subangular – subrounded
        - ▪ Some flow banding
        - ▪ Very elongated
        - ▪ Up to 50 cm in diameter, but mostly 5-15 cm
    - o Plinth:
        - ▪ Very weathered (tan-coloured)
        - ▪ Subrounded
        - ▪ Can't see texture due to weathering
        - ▪ 3% of clasts
        - ▪ Up to 25 cm in diameter
    - o Grey:
        - ▪ Weathered Plinth? Partially welded pumiceous clasts?
        - ▪ Porphyritic, with small phenos. of plag/mafic minerals (biot?)
        - ▪ Subangular
        - ▪ <1% of clasts
        - ▪ Up to 40 a few cm's in diameter
    - o Other:
        - ▪ Sandstone & slate clasts?
        - ▪ Subrounded
        - ▪ <1% of clasts
        - ▪ Up to a few cm's in diameter
    - o White/beige/light pink monzonite:
        - ▪ Medium-grained
        - ▪ Very weathered/altered
        - ▪ Subrounded
        - ▪ Small phenos. of plag (less than 1 mm)/qtz (avg. 1 mm)/pyx (avg. 1 mm) (<5% mafic phenocrysts)
        - ▪ <1% of clasts
        - ▪ Up to a few cm's in diameter
- Matrix: Grey, fine-grained, ashy, also with fragments of the clasts listed above (sometimes lone phenocrysts)
- Matrix supported
- Surface is very weathered, making it difficult to distinguish clast types
- Deformation is especially evident around lithics (especially Plinth) and their boundaries
- Clasts are visibly deformed/elongated, displaying a fabric
- Pull-aparts observed

FIELD TEXTURE MAP #6
(Densely welded block and ash flow deposit, Block #5, Field Site 1)

- Clast types:
  - Black:
    - Glassy
    - Dense
    - Variably welded showing different shades of grey – black
    - Porphyritic, with (avg. 2 mm) phenos of plag/hbl/pyx (<20%)
    - 90-95% of clasts
    - Subangular – subrounded
    - Some flow banding (~2%) at 55-60° from fabric
    - Some very elongated, arcuate shapes
    - Up to 75 cm in diameter, but mostly <20 cm
  - Plinth:
    - Light grey
    - Porphyritic, with plag/qtz…biot seems to have weathered out
    - Subrounded
    - 3% of clasts
    - Up to 50 cm in diameter
  - Grey:
    - Weathered Plinth? Partially welded pumiceous clasts?
    - Porphyritic, with small phenos. of plag/mafic minerals (biot?)
    - Subrounded
    - Some flow banding
    - 1% of clasts
    - Up to 40 cm in diameter, but mostly just a few cm's
  - Other:
    - Slate?
    - Subrounded – subangular
    - Microcrystalline
    - Dark grey
    - Platy habit
    - 1% of clasts
    - Up to 5 cm in diameter
  - Other:
    - Sandstone?
    - Grey
    - Fine-grained
    - Structureless
    - Subrounded
    - <1% of clasts
    - Up to a 6 cm in diameter
  - White/beige/light pink monzonite:
    - Medium-grained
    - Subangular – subrounded
    - Small phenos. of plag (less than 1 mm)/qtz (avg. 1 mm)/pyx (avg. 1 mm) (<5% mafic phenocrysts)
    - 1% of clasts
    - Less than 10 cm in diameter
- Matrix: Grey, fine-grained, ashy, full of fragments (<1 cm in diameter)

- Matrix supported
- Shearing and folding of densely welded clasts around Plinth clasts
- Possible areas at edges/corners of clasts which resemble pressure shadows
- Clasts are visibly deformed/elongated, displaying a fabric
- Pull-aparts observed

FIELD TEXTURE MAP #7
(Basal non-welded block and ash flow deposit, Field Site 1)

- Clast types:
  - o Black:
    - Glassy
    - Densely welded
    - Variably welded showing different shades of grey – black
    - Phenocryst-poor
    - 3% of clasts
    - Subangular
    - Some flow banding (~2%) at 55-60° from fabric
    - Some very elongated, arcuate shapes
    - Up to 5 cm in diameter
  - o Plinth:
    - None seen in mapped area, but they do exist nearby in the outcrop
    - Light grey
    - Porphyritic, with plag/qtz/biot
    - Subrounded
    - Trace - 1% of clasts
    - Up to 15 cm in diameter
  - o Dark grey:
    - Welded
    - Porphyritic, with (avg. 2 mm) phenos of plag/hbl/pyx (10-20%)
    - Subangular
    - 46% of clasts
    - Up to 1 m+ in diameter, but mostly 5-15 cm
  - o Pumiceous clasts:
    - White – light grey
    - Subrounded
    - Porphyritic, with mafic phenos of hbl/pyx visible (10-20%)
    - 50% of clasts
    - Up to 1 m in diameter, but mostly 5-15 cm
  - o White/beige/light pink monzonite:
    - Medium-grained
    - Weathered orange
    - Subangular – subrounded
    - Small phenos. of plag (less than 1 mm)/qtz (avg. 1 mm)/pyx (avg. 1 mm) (5-10% mafic phenocrysts)
    - 1% of clasts
    - Up to 4 cm in diameter
- Matrix: Light grey/brown, sand-like, fine-grained, ashy, full of fragments of clast types mentioned above
- Matrix supported
- Very pumice-rich compared to densely welded blocks
- Erosional surface/gradation up to densely welded block and ash flow deposit?
- Not much elongation/flattening or fabric, although some larger clasts seem to have their long axis parallel to the fabric observed above in the densely welded zone
- Possible imbrication
- Generally, clasts are more rounded, especially the pumice, although the welded clasts have more distinctive boundaries (maybe b/c they aren't as welded?)

- Poorly sorted
- Slight fining-upward trend see at the outcrop scale

FIELD TEXTURE MAP #8
(Basal non-welded block and ash flow deposit, Field Site 1 (1-1.5 m NE of TM#7))

- Clast types:
    - o Black:
        - Glassy
        - Densely welded
        - Variably welded showing different shades of grey – black
        - Phenocryst-poor
        - 2% of clasts
        - Subangular
        - Some flow banding (~2%) at 55-60° from fabric
        - Some very elongated, arcuate shapes
        - Up to 6 cm in diameter
    - o Dark grey:
        - Welded
        - Porphyritic, with (avg. 2 mm) phenos of plag/hbl/pyx (10-20%)
        - Subangular
        - 42% of clasts
        - Up to 30 cm in diameter, but mostly 5-15 cm
    - o Pumiceous clasts:
        - White – light grey
        - Subrounded
        - Porphyritic, with mafic phenos of hbl/pyx visible (10-20%)
        - 55% of clasts
        - Up to 1 m in diameter, but mostly 5-15 cm
    - o White/beige/light pink monzonite:
        - Medium-grained
        - Weathered orange
        - Subangular – subrounded
        - Small phenos. of plag (less than 1 mm)/qtz (avg. 1 mm)/pyx (avg. 1 mm) (5-10% mafic phenocrysts)
        - 1% of clasts
        - Up to 3 cm in diameter
- Matrix: Light grey/brown, sand-like, fine-grained, ashy, full of fragments of clast types mentioned above
- Matrix supported
- Very pumice-rich compared to densely welded blocks
- Erosional surface/gradation up to densely welded block and ash flow deposit?
- Not much elongation/flattening or fabric, although some larger clasts seem to have their long axis parallel to the fabric observed above in the densely welded zone
- Possible imbrication
- Generally, clasts are more rounded, especially the pumice, although the welded clasts have more distinctive boundaries (maybe b/c they aren't as welded?)
- Poorly sorted
- Slight fining-upward trend see at the outcrop scale

110

FIELD TEXTURE MAP #9
(Upper, incipiently welded block and ash flow deposit (oxidized), Field Site 2)

- Clast types:
    - o Black:
        - Glassy
        - Densely welded
        - Variably welded showing different shades of grey – black
        - Mafic phenocrysts of hbl/pyx visible (~10%)
        - 5% of clasts
        - Subangular
        - Up to 6 cm in diameter
    - o Pumiceous clasts:
        - Various shades of grey, incipiently welded
        - Subangular - subrounded
        - Porphyritic, with felsic & mafic phenos of hbl/pyx visible (~20%)
        - 95% of clasts
        - Up to 1.5 m in diameter, but mostly 5-15 cm
- Matrix: Orange/brown (oxidized), sand-like, fine-grained, ashy, full of fragments of clast types mentioned above
- Matrix supported, but with a lot of small <1 cm clasts/grains
- Pumice-rich, but some pumice seems more welded/dense than at the base of the Classic Section
- Not much elongation/flattening or fabric, although some larger clasts seem to have their long axis parallel to the fabric observed above in the densely welded zone
- Possible imbrication
- Pumice-like clasts are less rounded that at the base of the Classic Section
- Poorly sorted
- Weathered surface makes it difficult to note clast types and textures
- Pumice-like clasts sometimes have a ~1 cm, orange alteration ring
- Flow banding only seen in very small clasts; no breadcrusting observed
- Apparent thickness of indurated section: 2-2.5 m
- Other types of clasts? Accidental sed/plutonic/meta. rocks?

FIELD TEXTURE MAP #10
(Upper, incipiently welded block and ash flow deposit (oxidized),
Field Site 2 (90 m SE of TM#9))

- Clast types:
    o Black:
        ▪ Glassy
        ▪ Densely welded
        ▪ Variably welded showing different shades of grey – black
        ▪ Mafic phenocrysts of hbl/pyx visible (~5-10%)
        ▪ 25-30% of clasts
        ▪ Subangular
        ▪ Up to 10 cm in diameter
    o Pumiceous clasts:
        ▪ Various shades of grey, incipiently welded
        ▪ Subangular - subrounded
        ▪ Porphyritic, with felsic & mafic phenos of hbl/pyx visible (~20%)
        ▪ 70% of clasts
        ▪ Up to 1 m in diameter, but mostly 5-15 cm
    o White/beige/light pink monzonite:
        ▪ Only 1 clast observed in mapped area
        ▪ Medium-grained
        ▪ Weathered orange/brown
        ▪ Subrounded
        ▪ Small mafic phenos. observed (~5%)
        ▪ In general, 1% of clasts
        ▪ Up to 5 cm in diameter
- Some Plinth Assemblage clasts observed outside of mapped area; ~1% of clasts; some are red, grey in colour
- Matrix: Light pink/orange/brown (oxidized), sand-like, fine-grained, ashy, full of fragments of clast types mentioned above
- Matrix supported, but with a lot of small <1 cm clasts/grains
- Rich in pumice-like clasts
- Not much elongation/flattening or fabric, although some larger clasts seem to have their long axis parallel to the fabric observed above in the densely welded zone
- Pumice-like clasts are more rounded that at TM#9
- Poorly sorted
- Weathered surface makes it difficult to note clast types and textures
- Pumice-like clasts sometimes have a ~1 cm, orange alteration ring
- No breadcrusting observed
- Apparent thickness of indurated section: 2 m with a ~10 m talus slope

- Clast types:
    - o Black:
        - ▪ Glassy
        - ▪ Densely welded
        - ▪ Variably welded showing different shades of grey – black
        - ▪ Mafic phenocrysts of hbl/pyx visible (~5-10%)
        - ▪ 60-70% of clasts
        - ▪ Some red oxidation/alteration
        - ▪ Subangular
        - ▪ Up to 20 cm in diameter
    - o Pumiceous clasts:
        - ▪ Whitish, altered orange/brown
        - ▪ Subangular – subrounded
        - ▪ Porphyritic, with mafic phenos of hbl/pyx visible (~5-15%)
        - ▪ 15-20% of clasts
        - ▪ No flow banding observed
        - ▪ Up to 35 cm in diameter
    - o Plinth:
        - ▪ Dark grey – black, with white/pink alteration
        - ▪ Porphyritic, with plag/qtz/biot
        - ▪ Subrounded
        - ▪ 5-10% of clasts
        - ▪ Up to 50 cm in diameter, but most 5-15 cm
    - o White/beige/light pink monzonite:
        - ▪ None in mapped area…granite?
        - ▪ Medium-grained
        - ▪ Pink/red alteration
        - ▪ Subrounded
        - ▪ Rich in large, felsic phenocrysts
        - ▪ < 1% of clasts
        - ▪ 2-8 cm in diameter
    - o Metamorphosed bedrock:
        - ▪ Only 2 clasts seen in mapped area
        - ▪ Blue-green with white (oxidized orange) stringers/veins
        - ▪ Porphyritic, with plag/qtz/biot
        - ▪ Subangular
        - ▪ In general, accounts for ~1% of clasts
        - ▪ 5-10 cm in diameter
- Matrix: Grey/brown, sand-like, fine-grained, ashy, full of fragments of clast types mentioned above
- Matrix supported, but with a lot of small <1 cm clasts/grains
- Not much elongation/flattening or fabric, although some larger clasts seem to have their long axis parallel to the fabric observed above in the densely welded zone
- Poorly sorted
- Weathered surfaces makes it difficult to note clast types and textures

FIELD TEXTURE MAP #12
(Upper, incipiently welded block and ash flow deposit (oxidized), Field Site 2)

- Clast types:
  - Black:
    - Glassy
    - Densely welded
    - Variably welded showing different shades of grey – black
    - Mafic phenocrysts of hbl/pyx visible (~5-10%)
    - 25-30% of clasts
    - No flow banding observed, but weathering/oxidation commonly masks texture
    - Subangular – subrounded
    - Up to 30 cm in diameter, but mostly 5-15 cm
  - Pumiceous clasts:
    - Various shades of grey, incipiently welded
    - Subrounded – subangular
    - Porphyritic, with mafic phenos of hbl/pyx visible (~10-20%)
    - 70% of clasts
    - No flow banding observed
    - Up to 1 m in diameter, but mostly 5-15 cm
- Plinth and monzonite clasts weren't observed in mapped area, but exist in outcrop & could also be masked by weathering/oxidation
- Matrix: Light pink/orange/brown (oxidized), sand-like, fine-grained, ashy, full of fragments of clast types mentioned above
- Matrix supported, but with a lot of small <1 cm clasts/grains
- Rich in pumice-like clasts
- Not much elongation/flattening or fabric, although some larger clasts seem to have their long axis parallel to the fabric observed above in the densely welded zone
- Poorly sorted
- Weathered surface makes it difficult to note clast types and textures
- Pumice-like clasts sometimes have a ~1 cm, orange alteration ring
- Apparent thickness of indurated section: 2 m with 5 m talus slope
- No breadcrusting observed

FIELD TEXTURE MAP #13
(Basal, non-welded block and ash flow deposit,
Field Site 1 (3 m NE of bulk sample area))

- Clast types:
  - Black:
    - Glassy
    - Densely welded
    - Variably welded showing different shades of grey – black
    - Phenocryst-poor
    - 55% of clasts
    - Subangular – subrounded
    - Some flow banding observed
    - Up to 30 cm in diameter, but mostly ~5 cm
  - Pumiceous clasts:
    - White – light grey
    - Subangular – subrounded
    - Porphyritic, with mafic phenos of hbl/pyx visible (10-20%)
    - 45% of clasts
    - No flow banding observed
    - Up to 50 cm in diameter, but mostly 10-15 cm
  - No monzonite or Plinth observed in mapped area
- Matrix: Light grey/brown, sand-like, fine-grained, ashy, full of fragments of clast types mentioned above
- Matrix supported
- Very pumice-rich compared to densely welded blocks
- Erosional surface/gradation up to densely welded block and ash flow deposit?
- Not much elongation/flattening or fabric, although some larger clasts seem to have their long axis parallel to the fabric observed above in the densely welded zone
- Possible imbrication
- Generally, clasts are more rounded, especially the pumice, although the welded clasts have more distinctive boundaries (maybe b/c they aren't as welded?)
- Poorly sorted
- Slight fining-upward trend see at the outcrop scale

APPENDIX B

IMAGE ANALYSIS METHODS: FTMs

The following sequences of photos document the process of recovering data from the field to obtaining results from image analysis (e.g. from Scion Image™, Image J™). The FTMs represent the full spectrum of welding intensity observed in the Keyhole Falls Member. The process for each FTM is as follows: **(a)** a field photo is taken of the mapped area overlain by the 1 m^2 grid, where "T" represents the top of the field texture map; **(b)** clasts greater than 0.5 cm are hand-drawn with the aid of the grid and graph paper; **(c)** the original FTM is retraced and scanned into a digital image; **(d)** the image in **(c)** is run through image analysis software and the output image is created based on clast recognition within the 1 m^2 area.
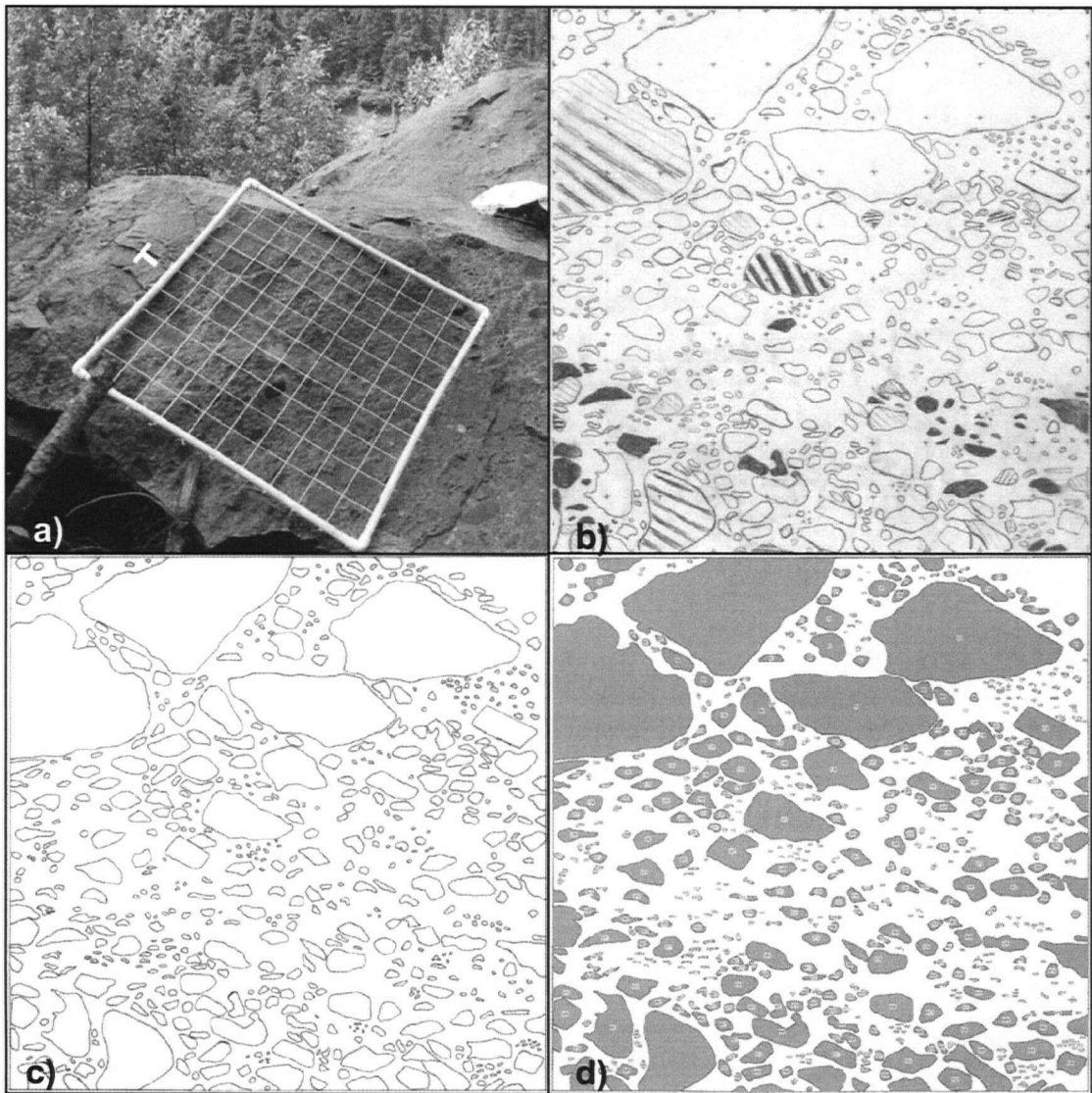
Figure B1: FTM 01 – Densely welded facies
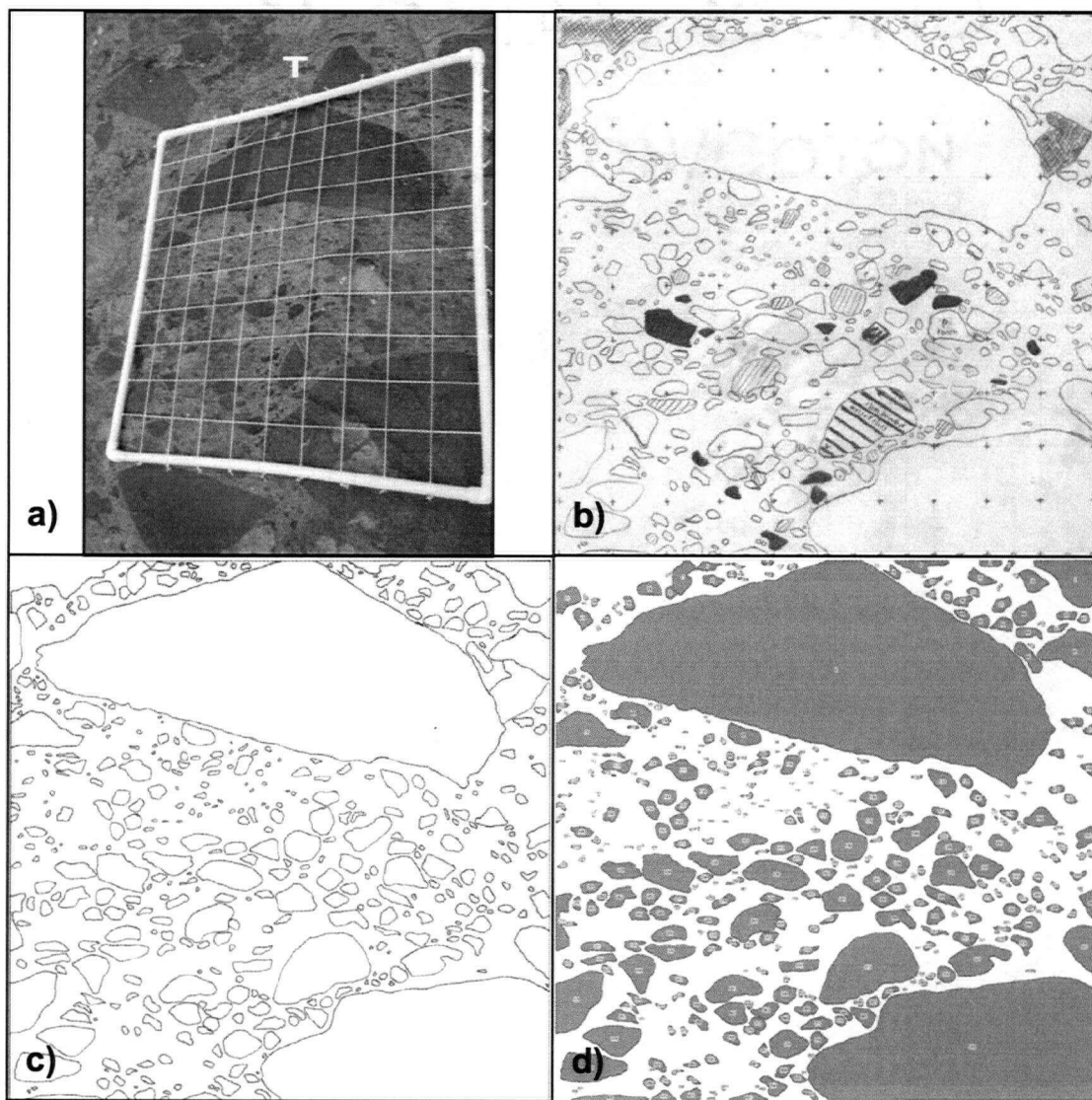
Figure B2: FTM 02 – Densely welded facies
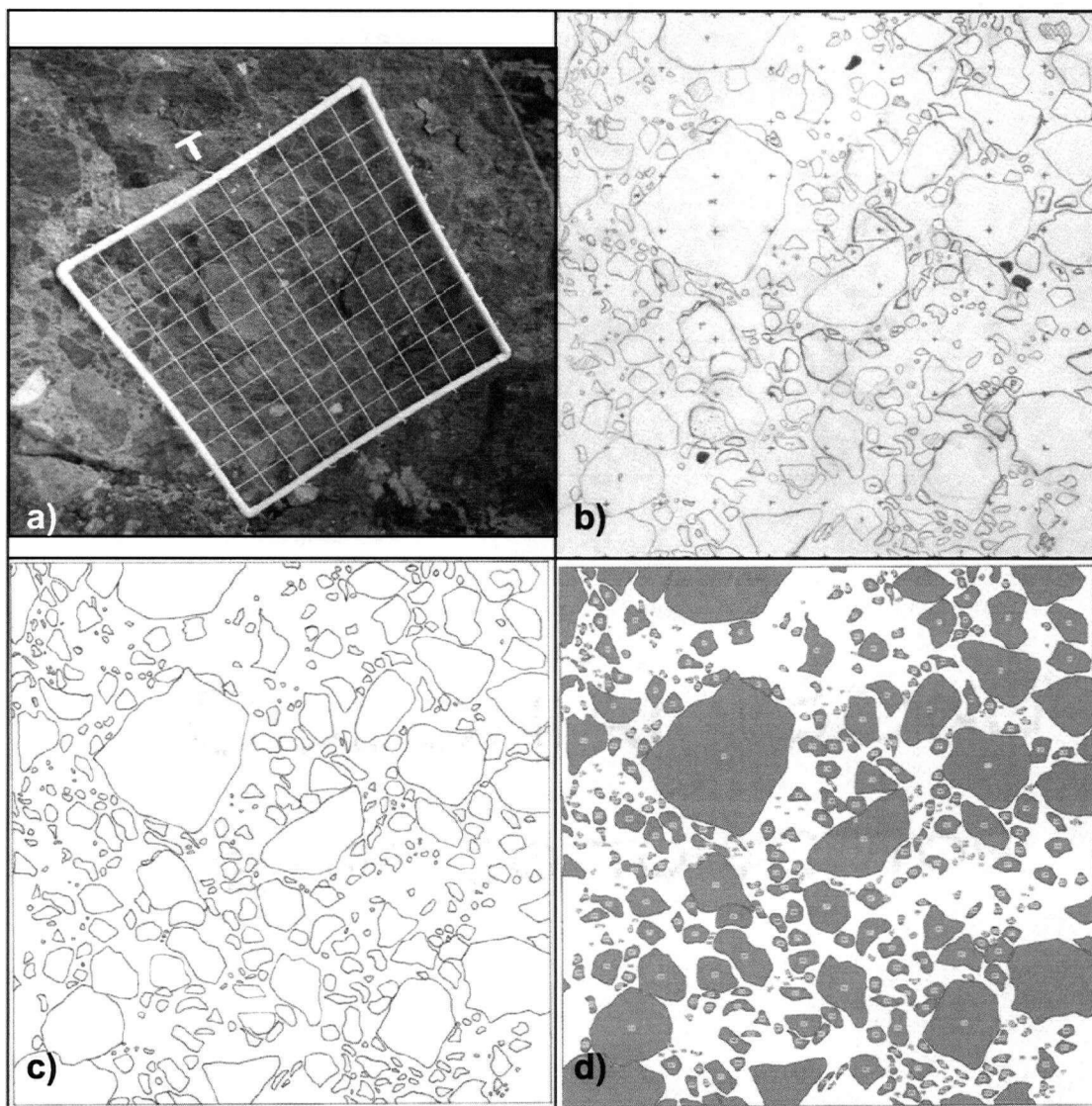
Figure B3: FTM 03 – Densely welded facies, in the plane of flattening

120
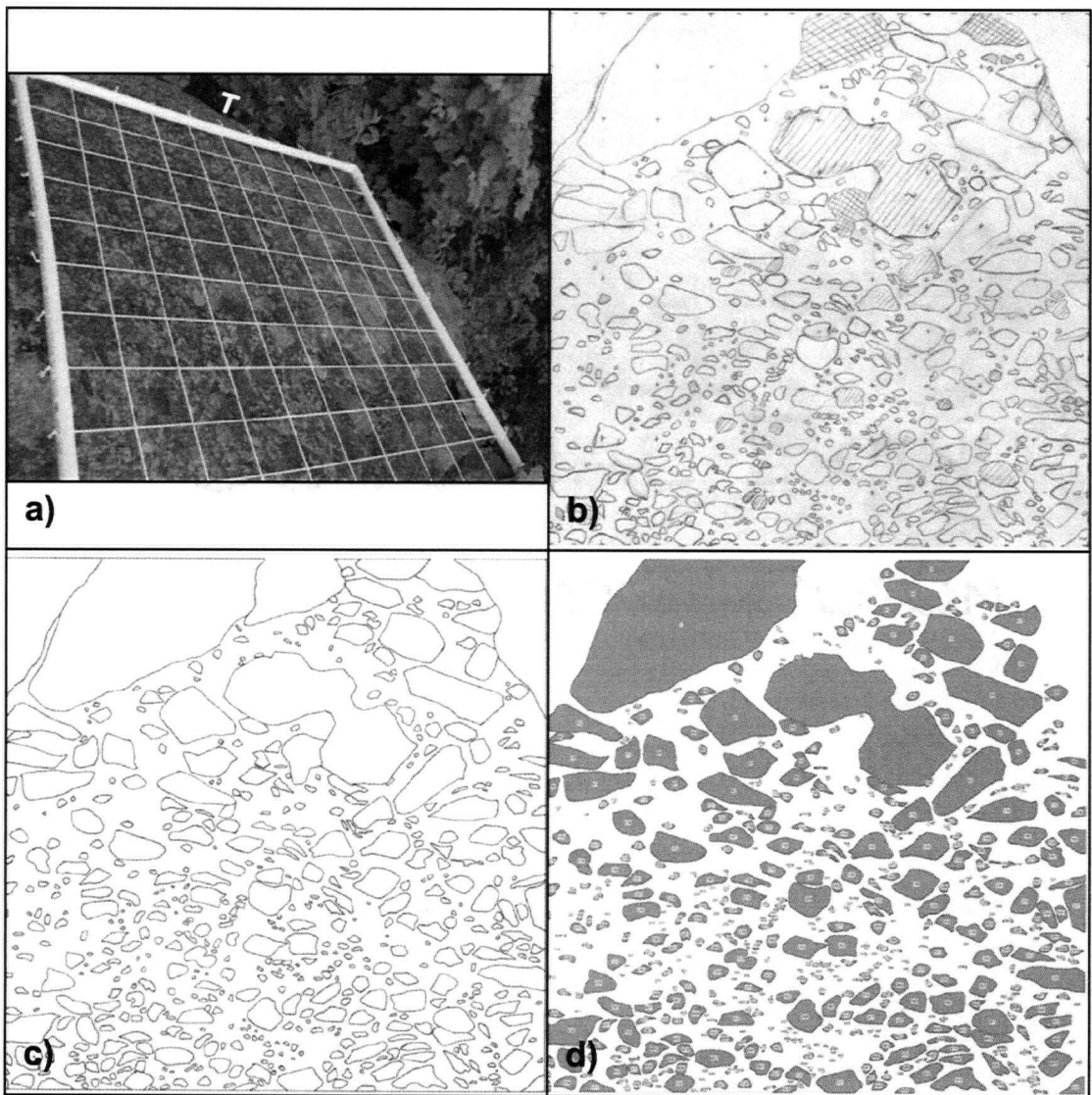
Figure B4: FTM 04 – Densely welded facies
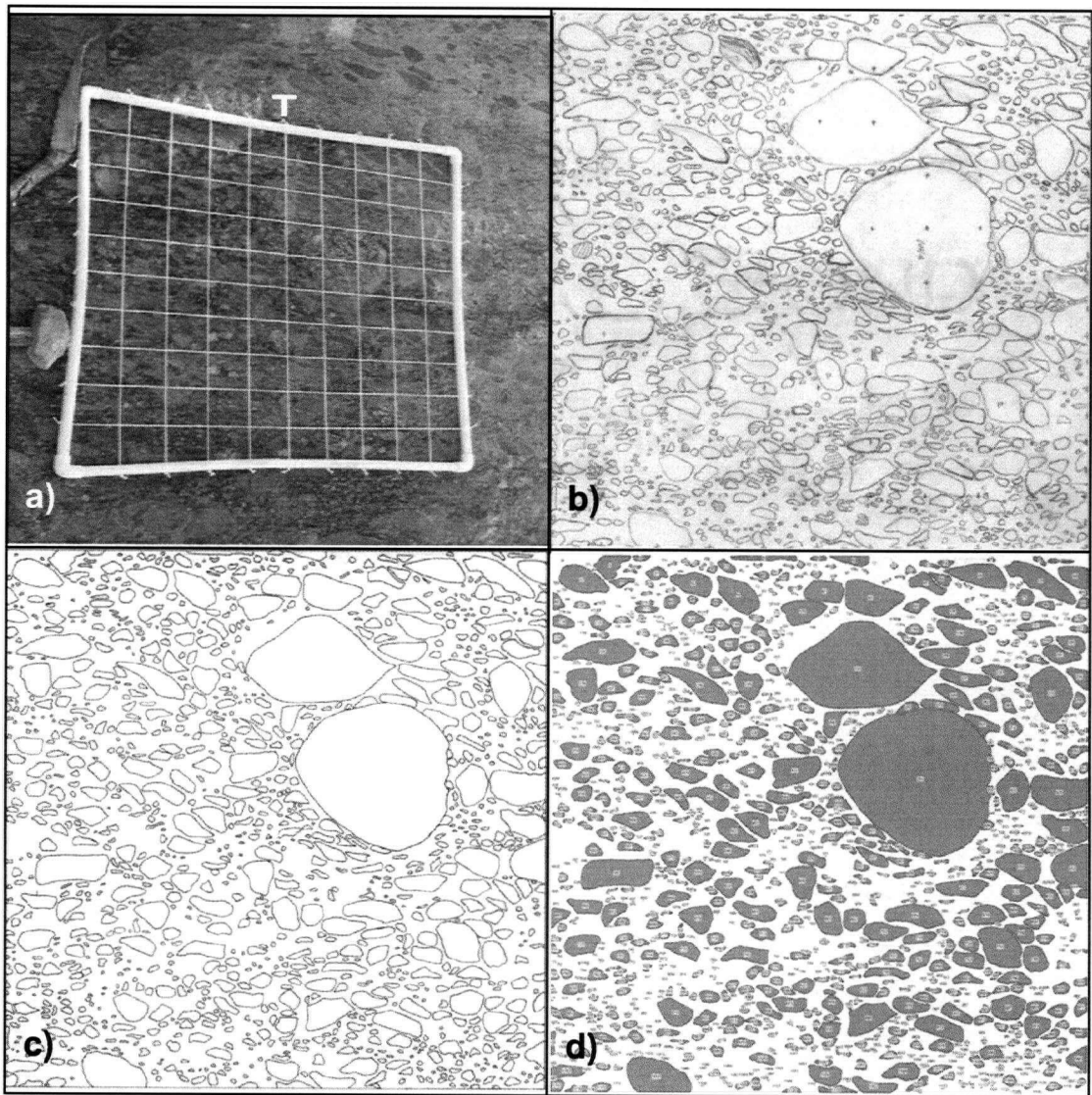
Figure B5: FTM 05 – Densely welded facies
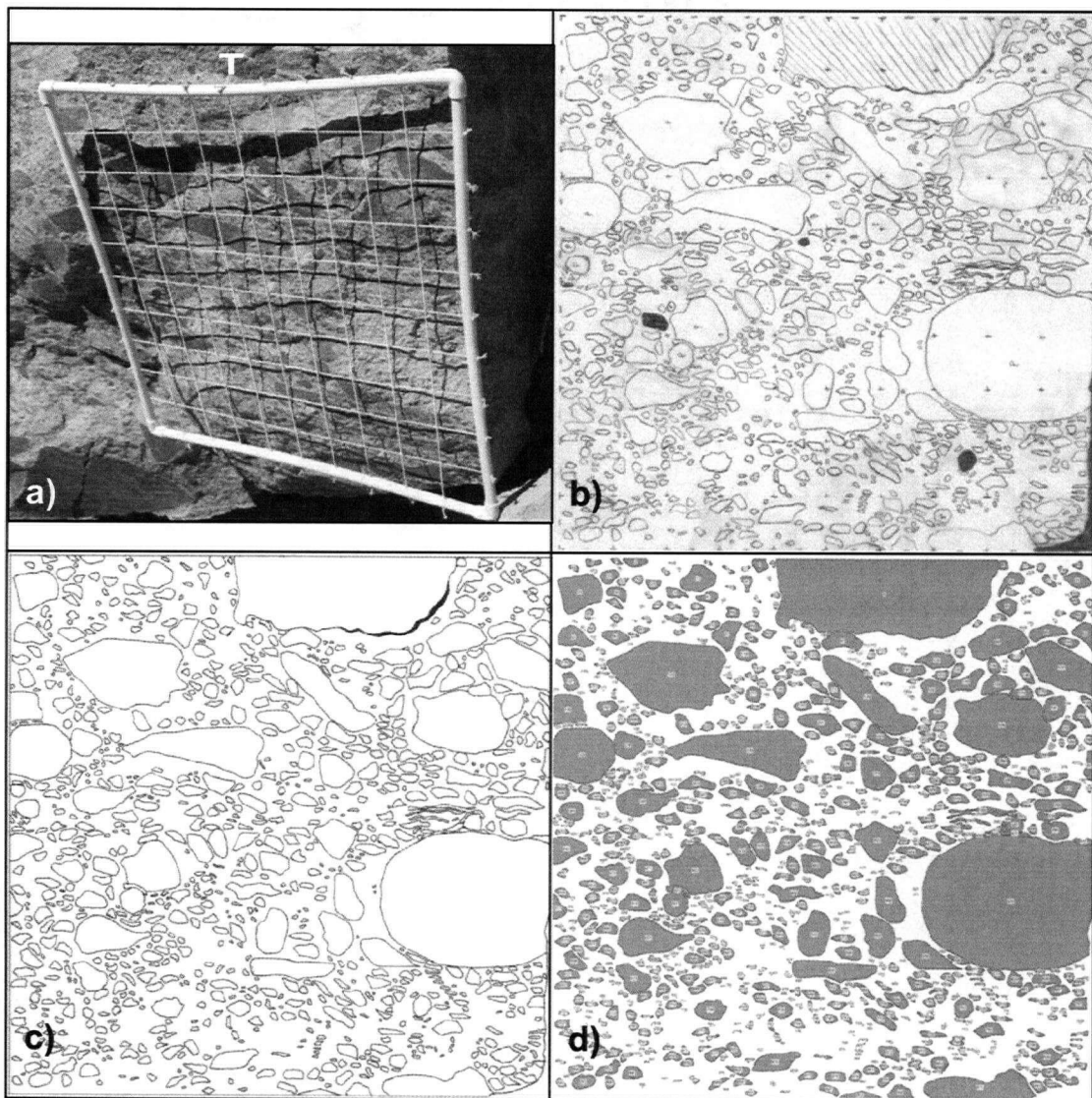
Figure B6: FTM 06 – Densely welded facies
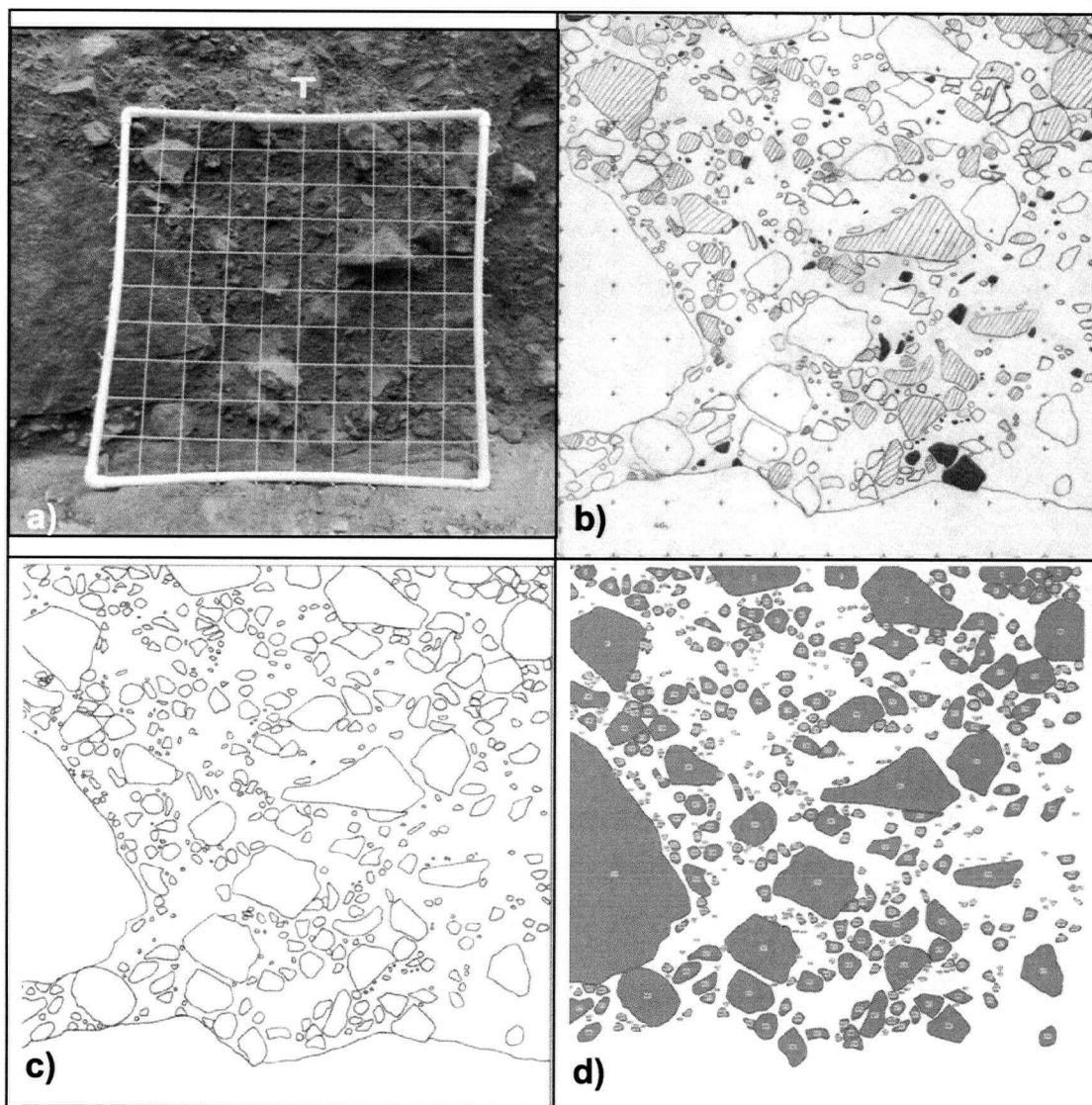
Figure B7: FTM 07 – Basal non-welded facies
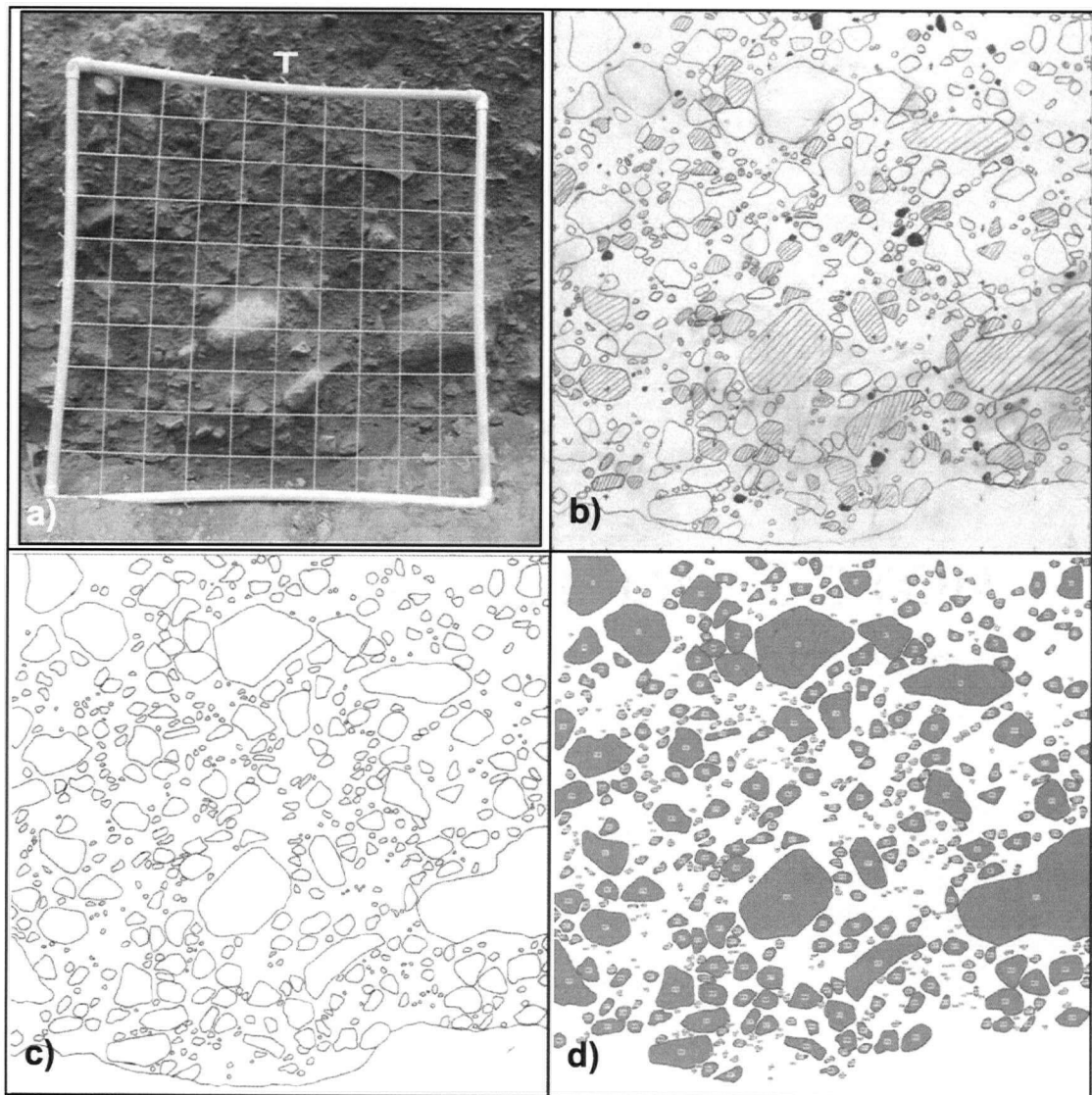
Figure B8: FTM 08 – Basal non-welded facies
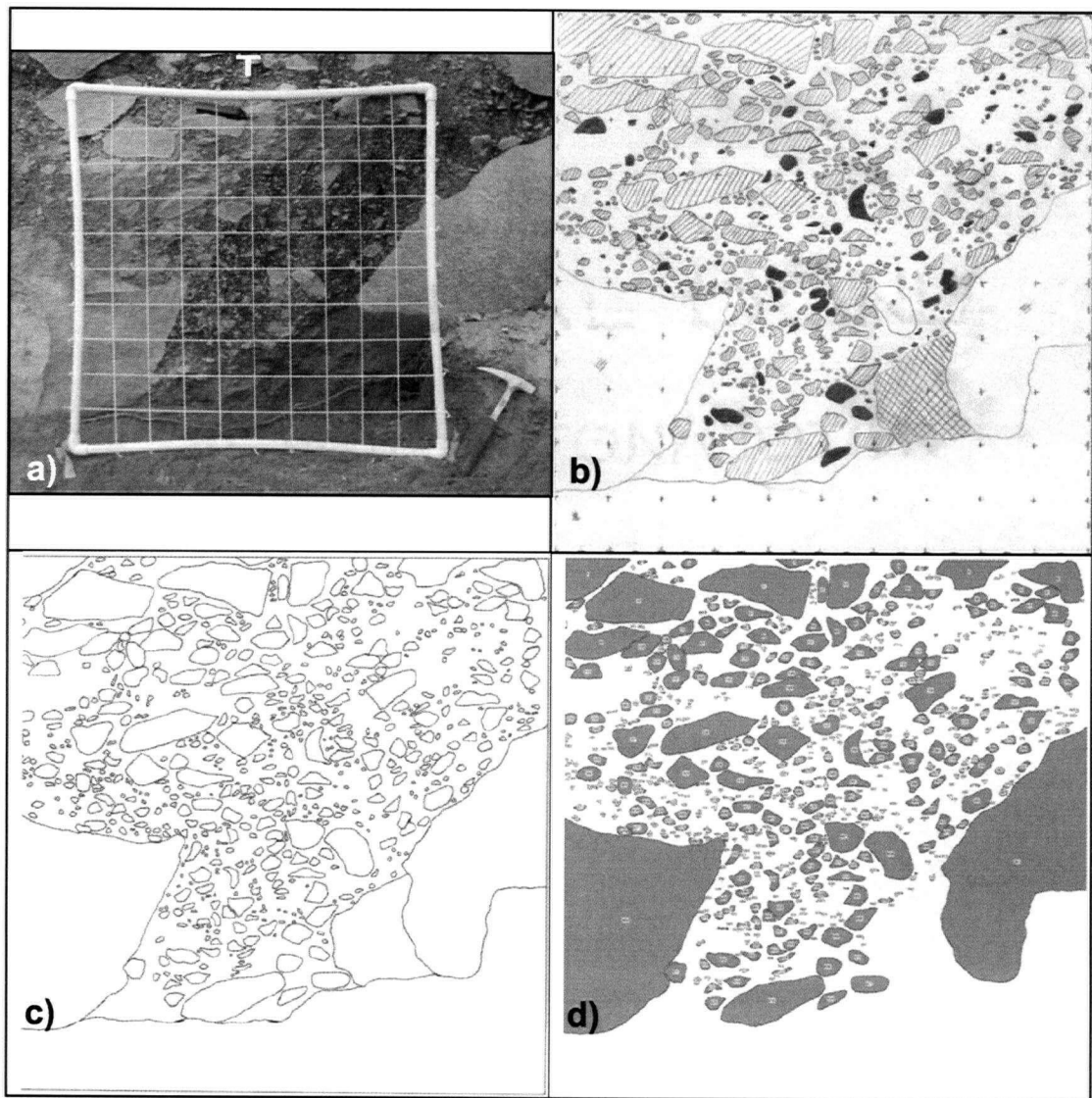
Figure B9: FTM 09 - Incipiently welded facies
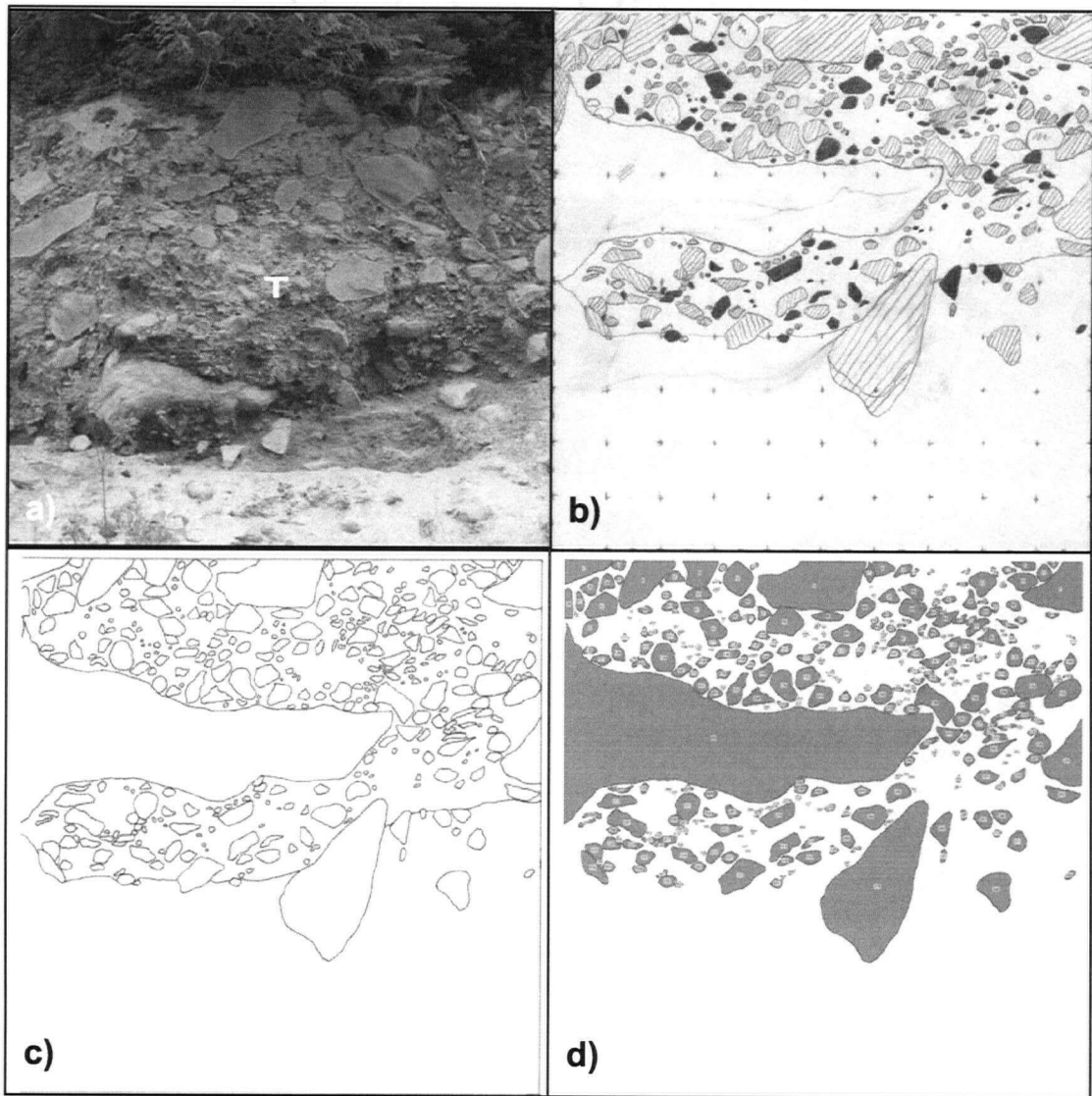
Figure B10: FTM 10 – Incipiently welded facies
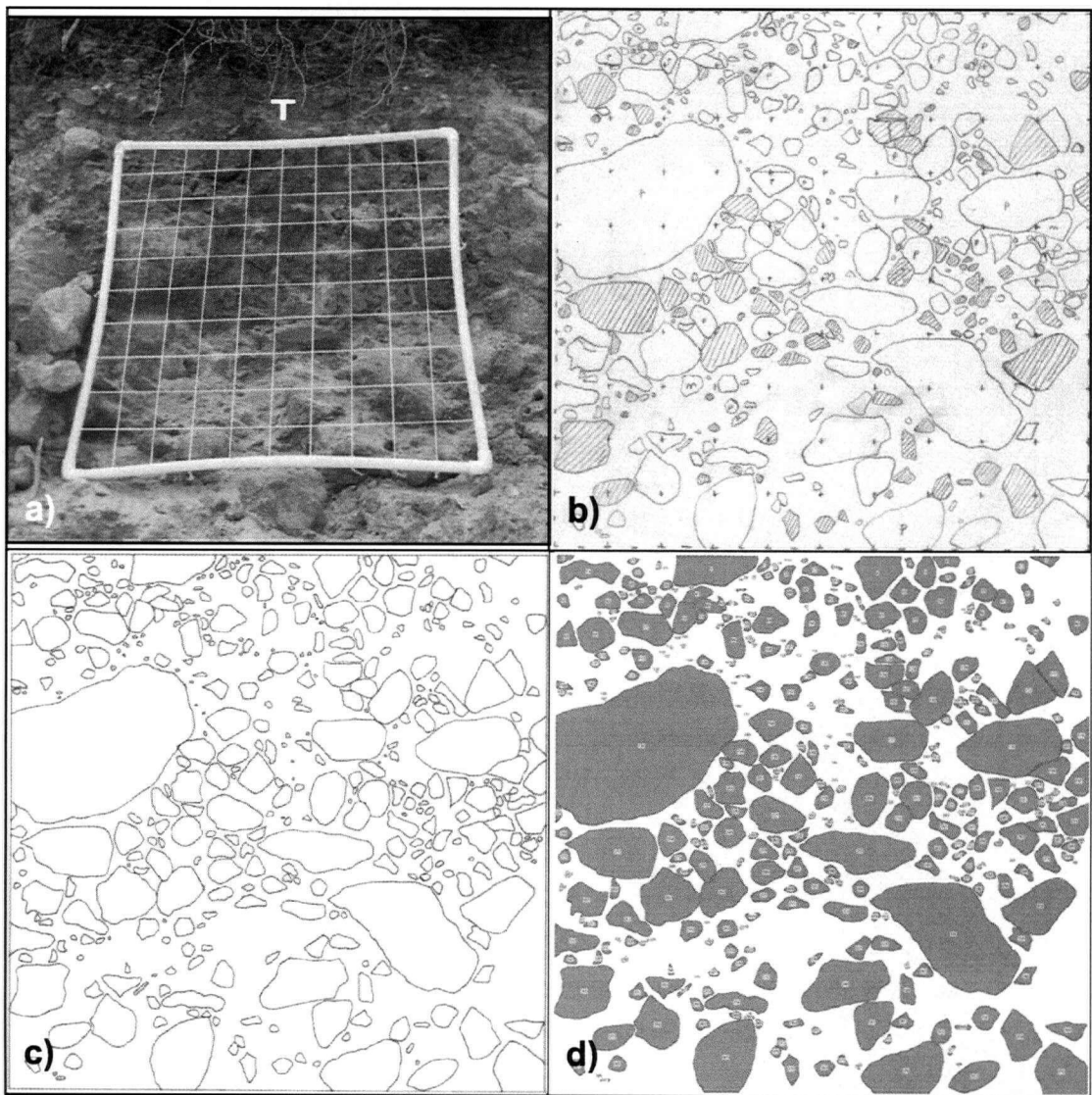
Figure B11: FTM 11 – Upper non-welded facies
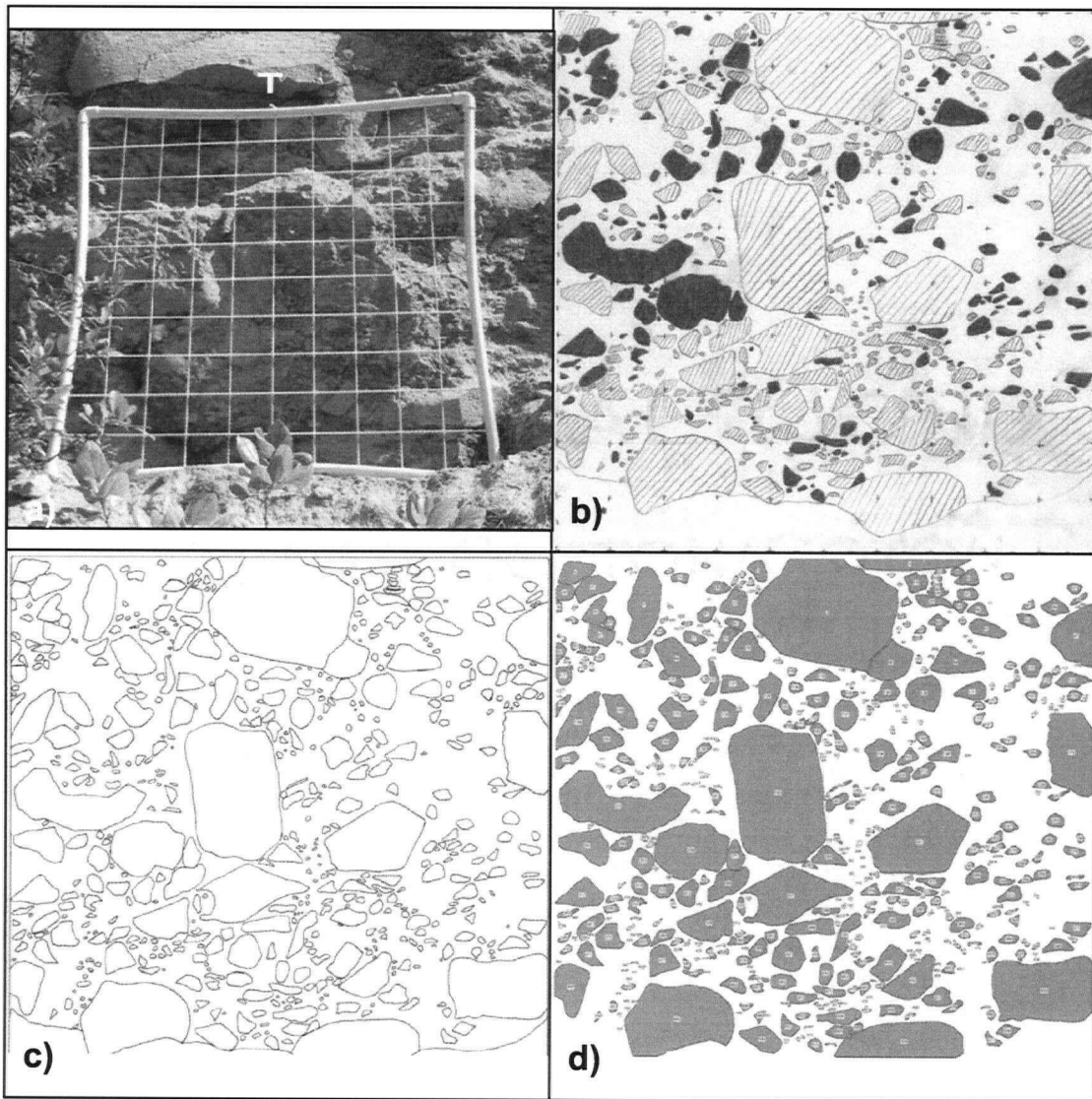
Figure B12: FTM 12 – Incipiently welded facies
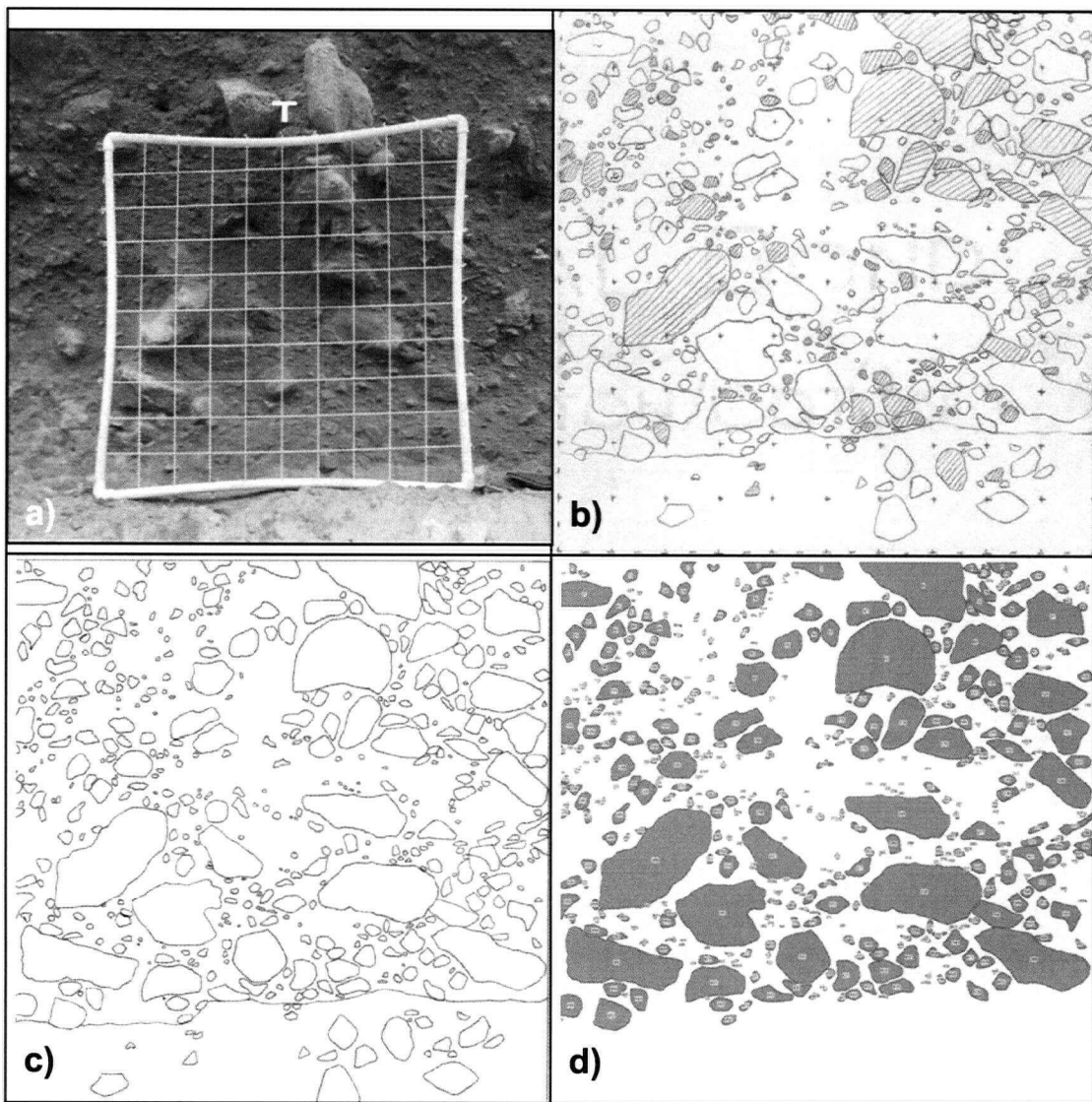
Figure B13: FTM 13 – Basal non-welded facies

APPENDIX C

IMAGE ANALYSIS METHODS: STMs

The following sequences of photos document the process of recovering data from the slabs/hand samples to obtaining results from image analysis (e.g. from Scion Image™, Image J™). All STMs were created from slabs of densely welded material due to its' competence. The process for each STM is as follows: **(a)** a photo is taken of the polished slab; **(b)** clasts greater than 0.5 mm are hand-drawn with the aid of an acetate and permanent marker; **(c)** the original FTM is retraced and scanned into a digital image; **(d)** the image obtained in **(c)** is run through image analysis software where the output image is created based on clast recognition.
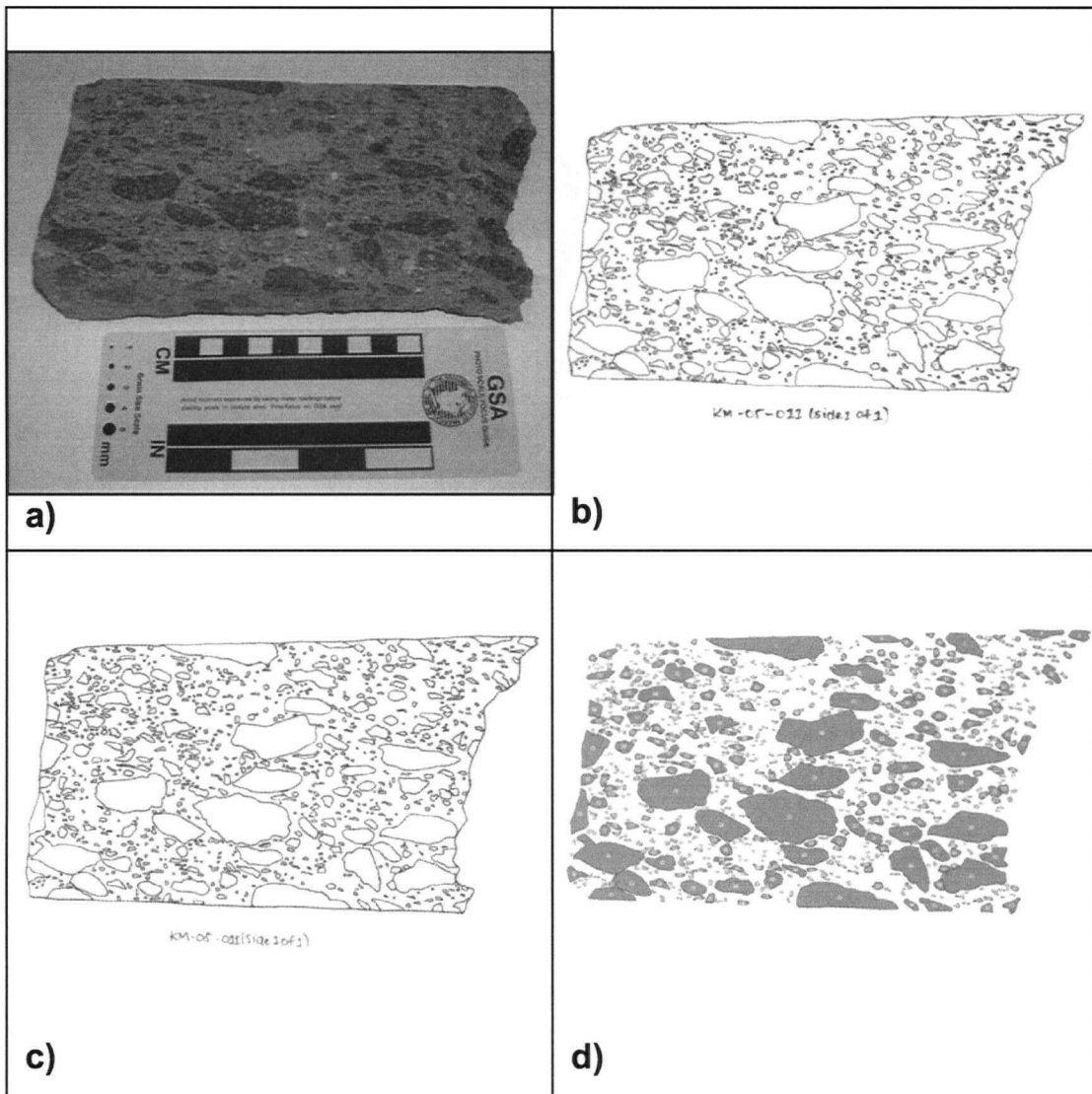
Figure C1: STM 01 – Densely welded facies
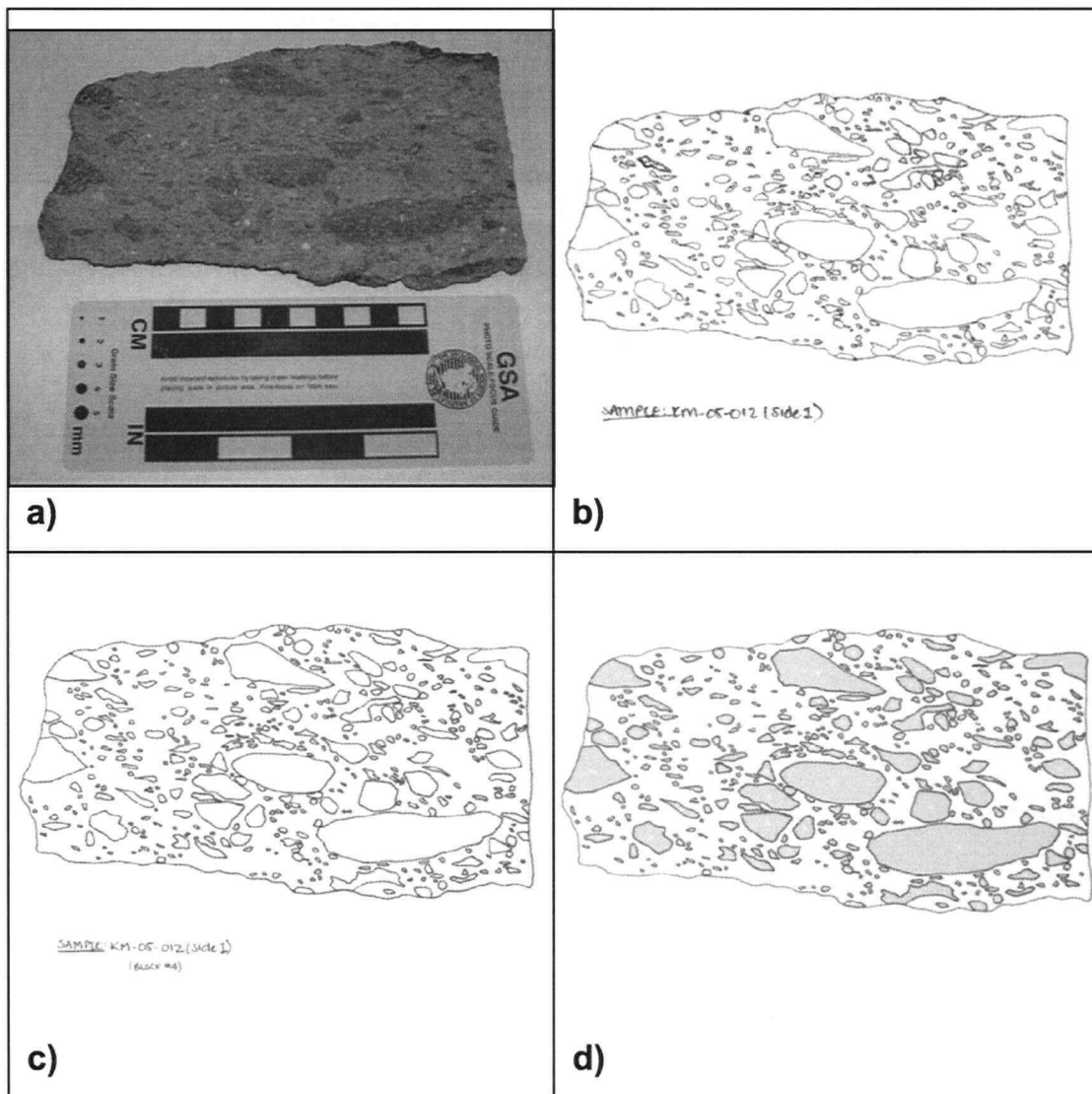
Figure C2: STM 02 – Densely welded facies

a)

b)

SAMPLE: KM-05-017c (Side1 - w Krylon)

c)

SAMPLE: KM-05-017c (Side1)
(BLOCKED)

d)
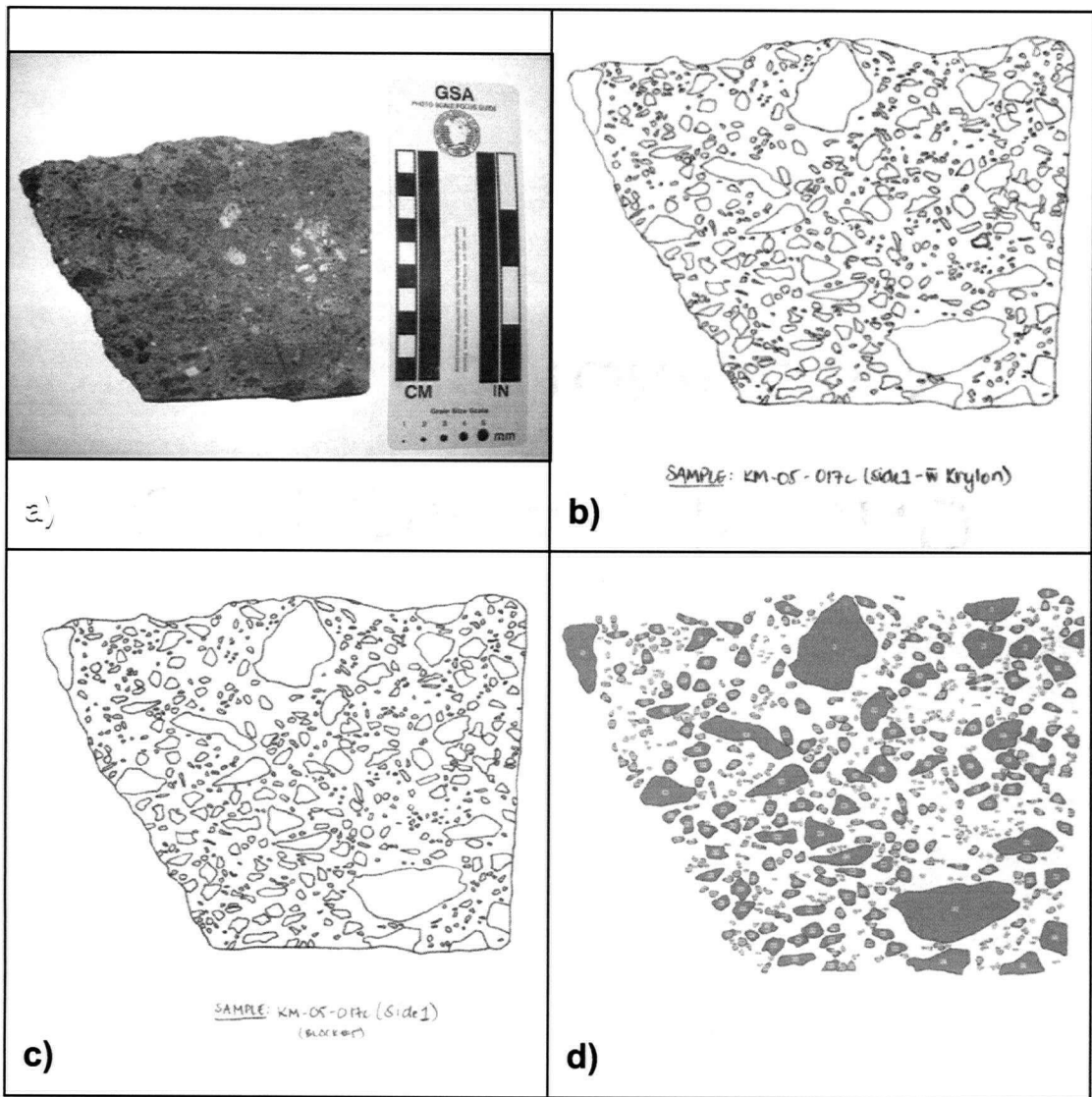
Figure C3: STM 03 – Densely welded facies
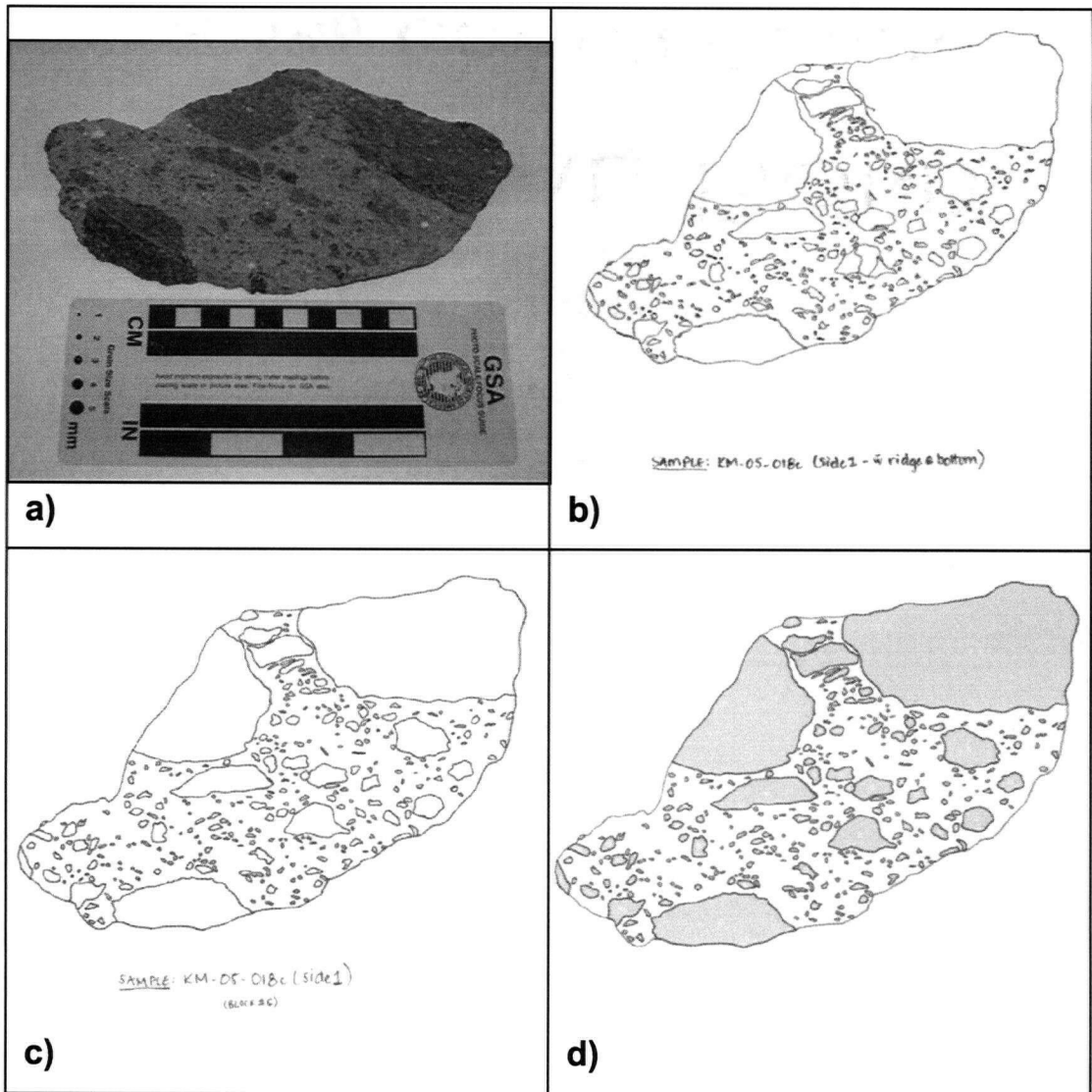
Figure C4: STM 04 – Densely welded facies
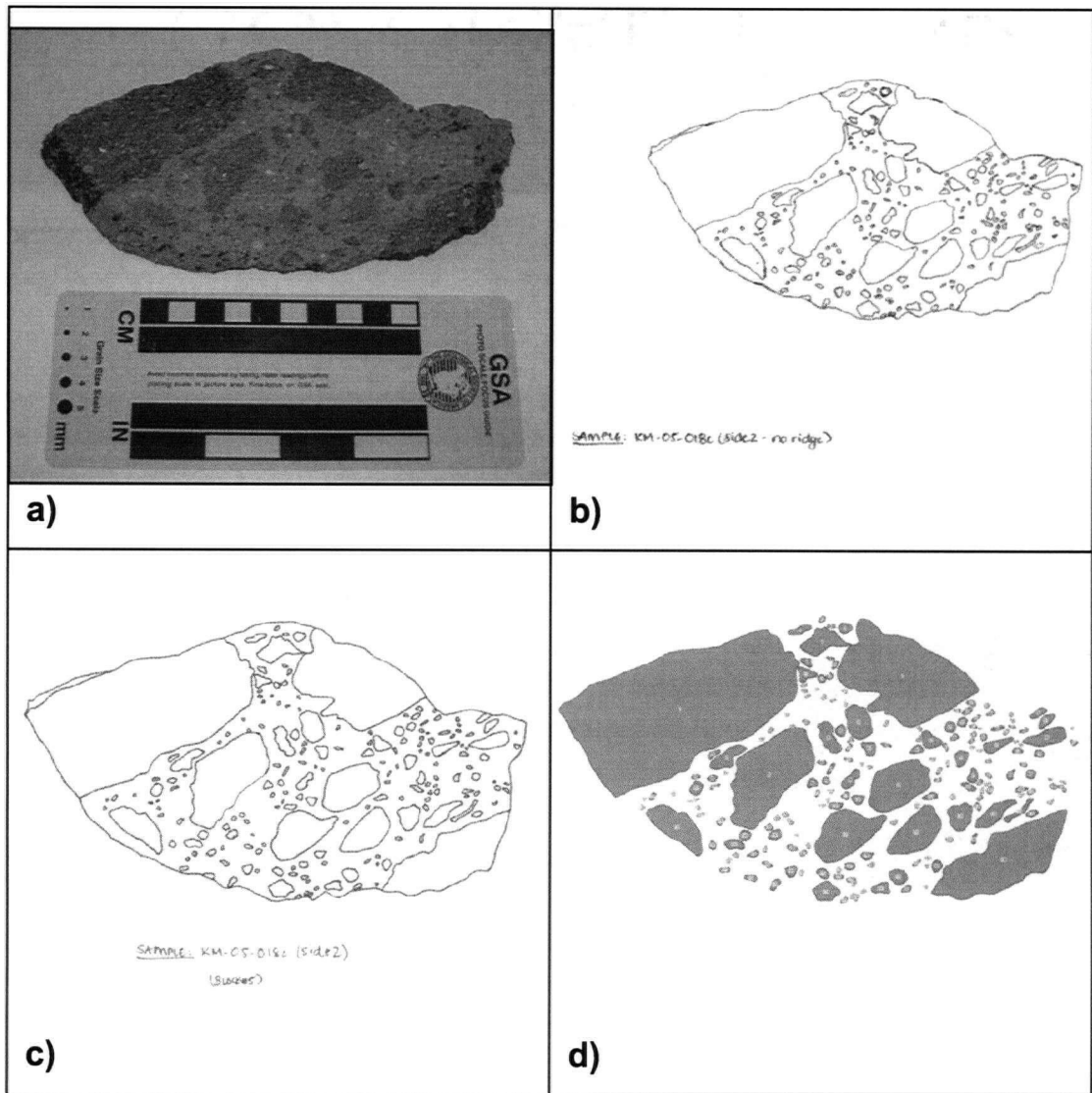
Figure C5: STM 05 – Densely welded facies
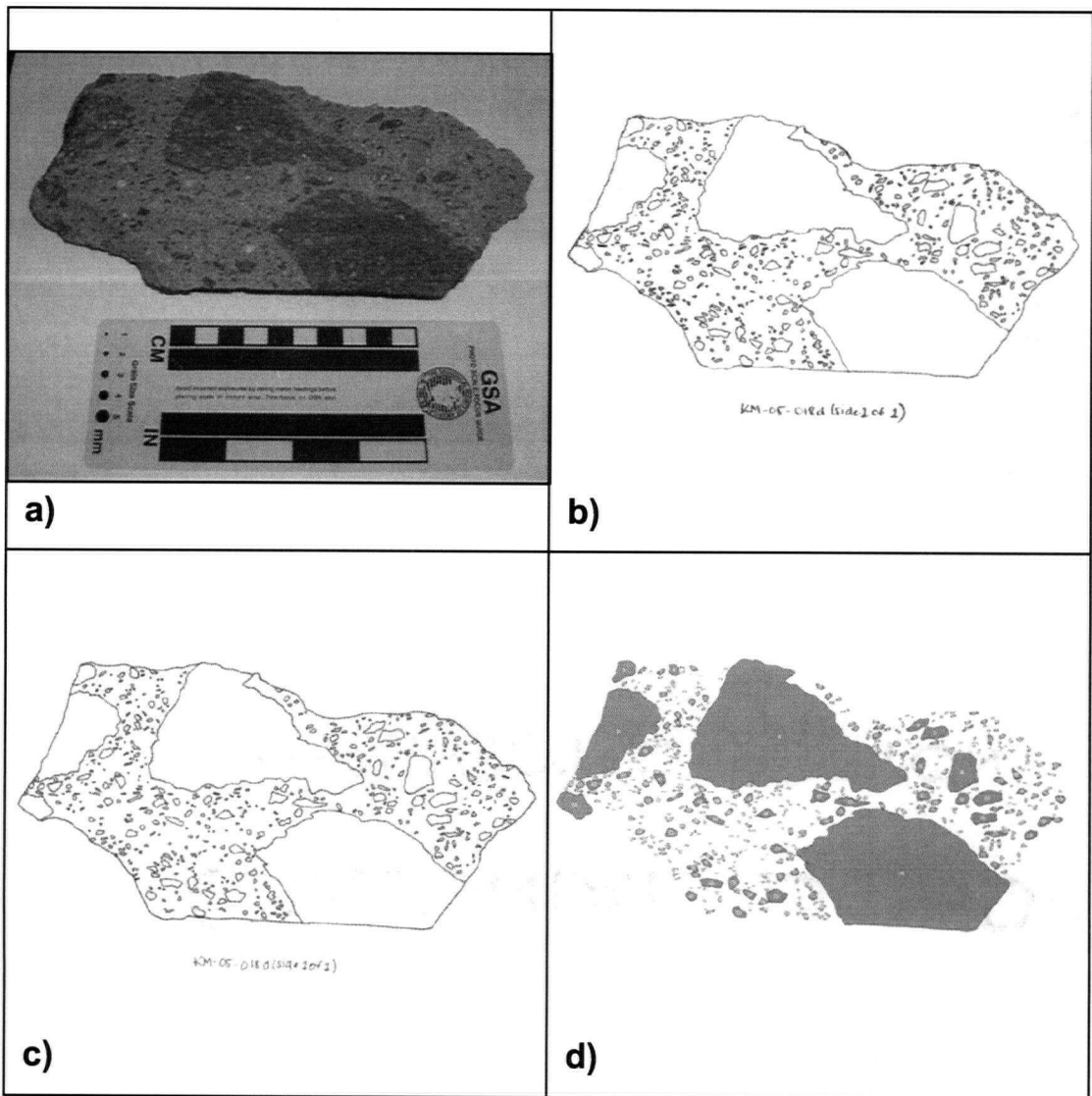
Figure C6: STM 06 – Densely welded facies
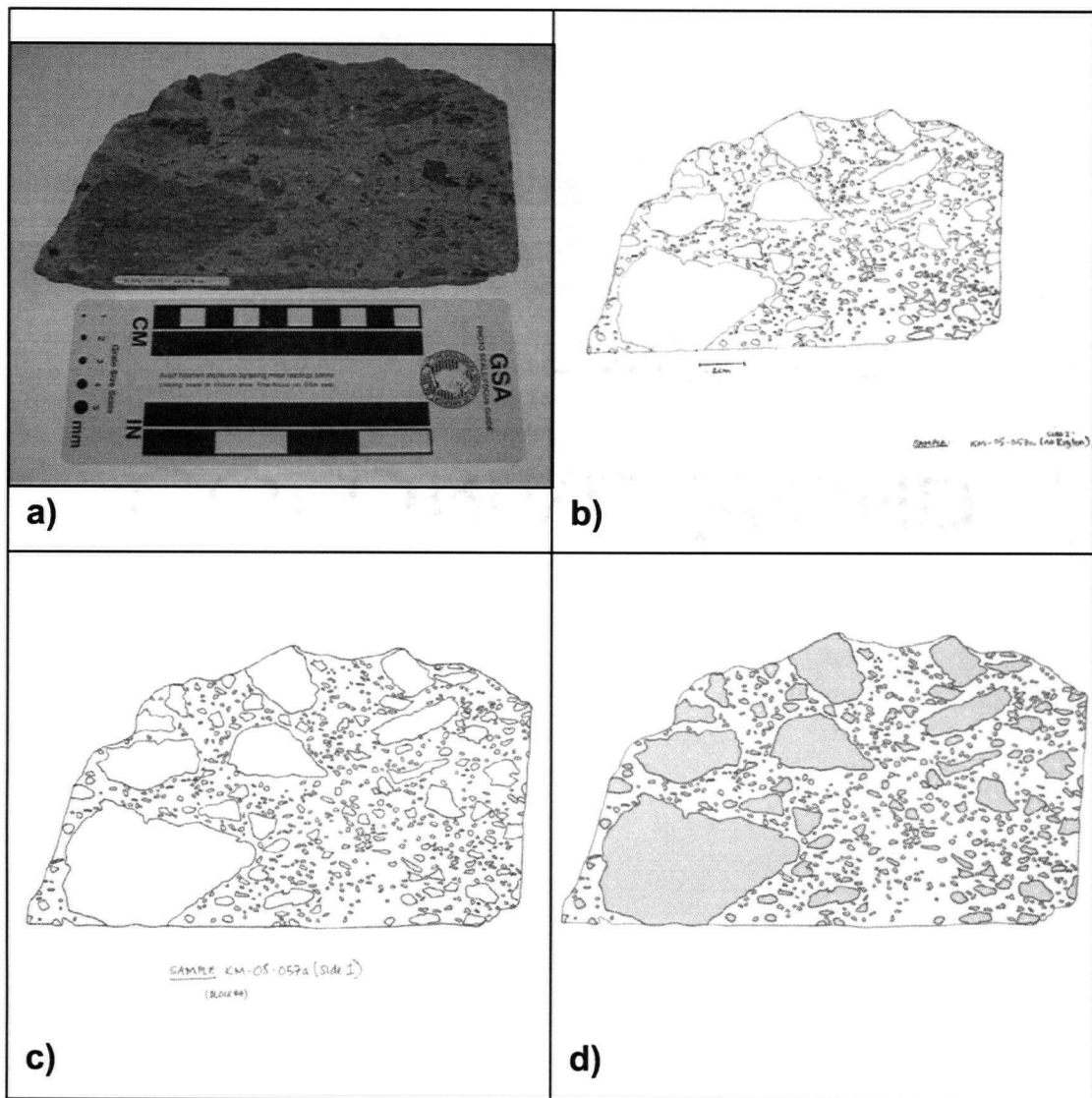
Figure C7: STM 07 – Densely welded facies

a)

b)

c)

d)
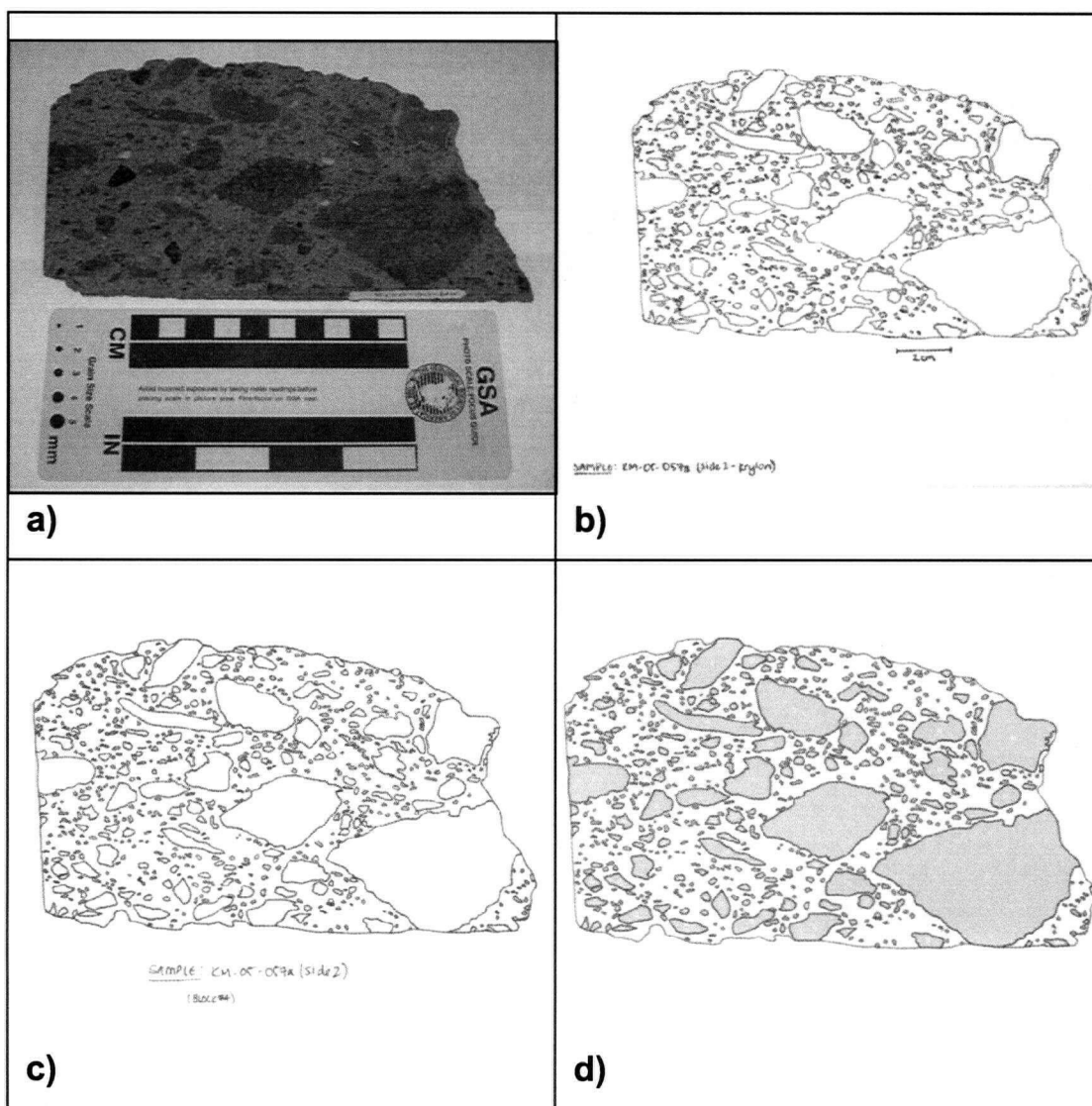
Figure C8: STM 08 – Densely welded facies
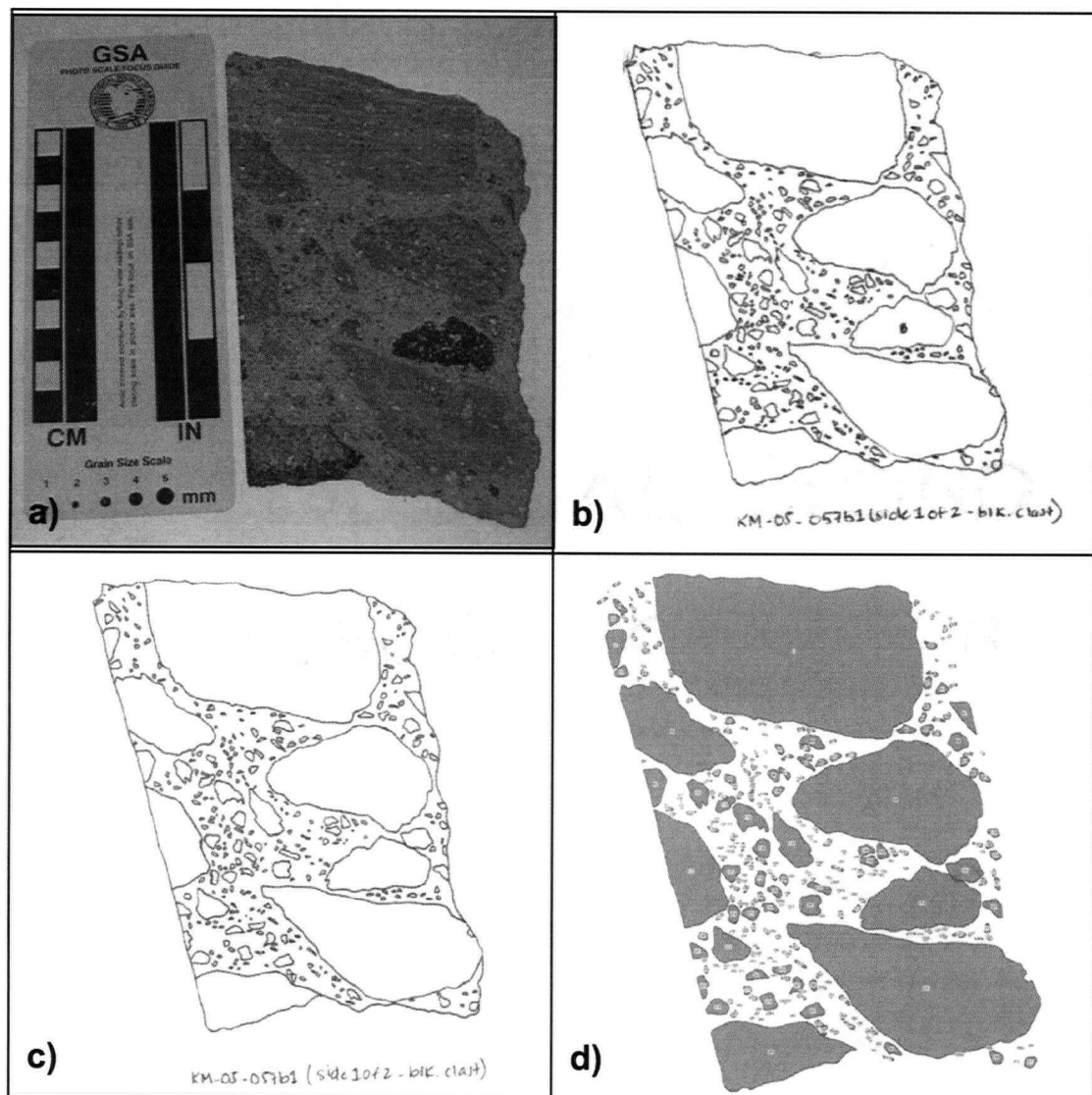
Figure C9: STM 09 – Densely welded facies

141
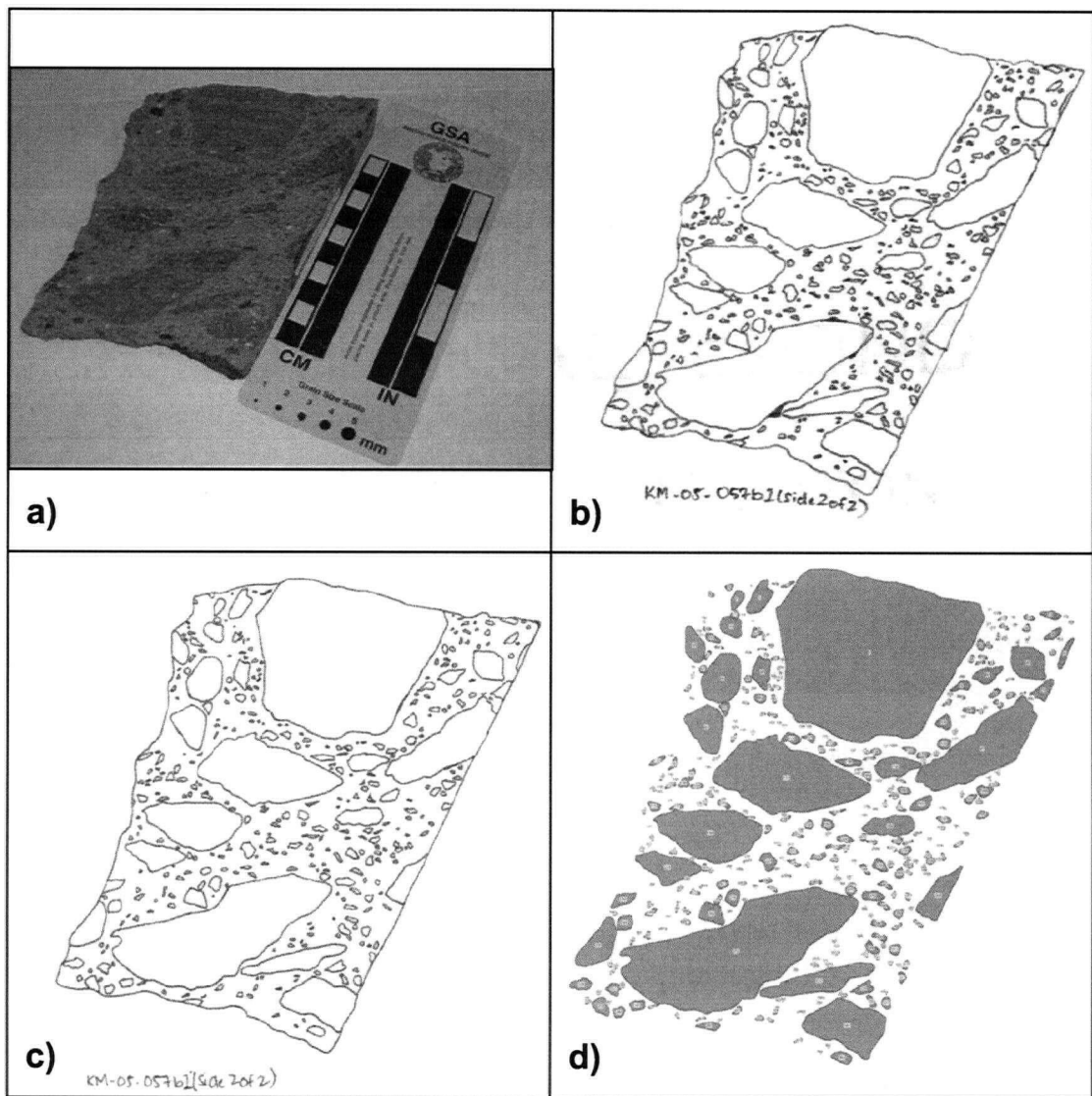
Figure C10: STM 10 – Densely welded facies
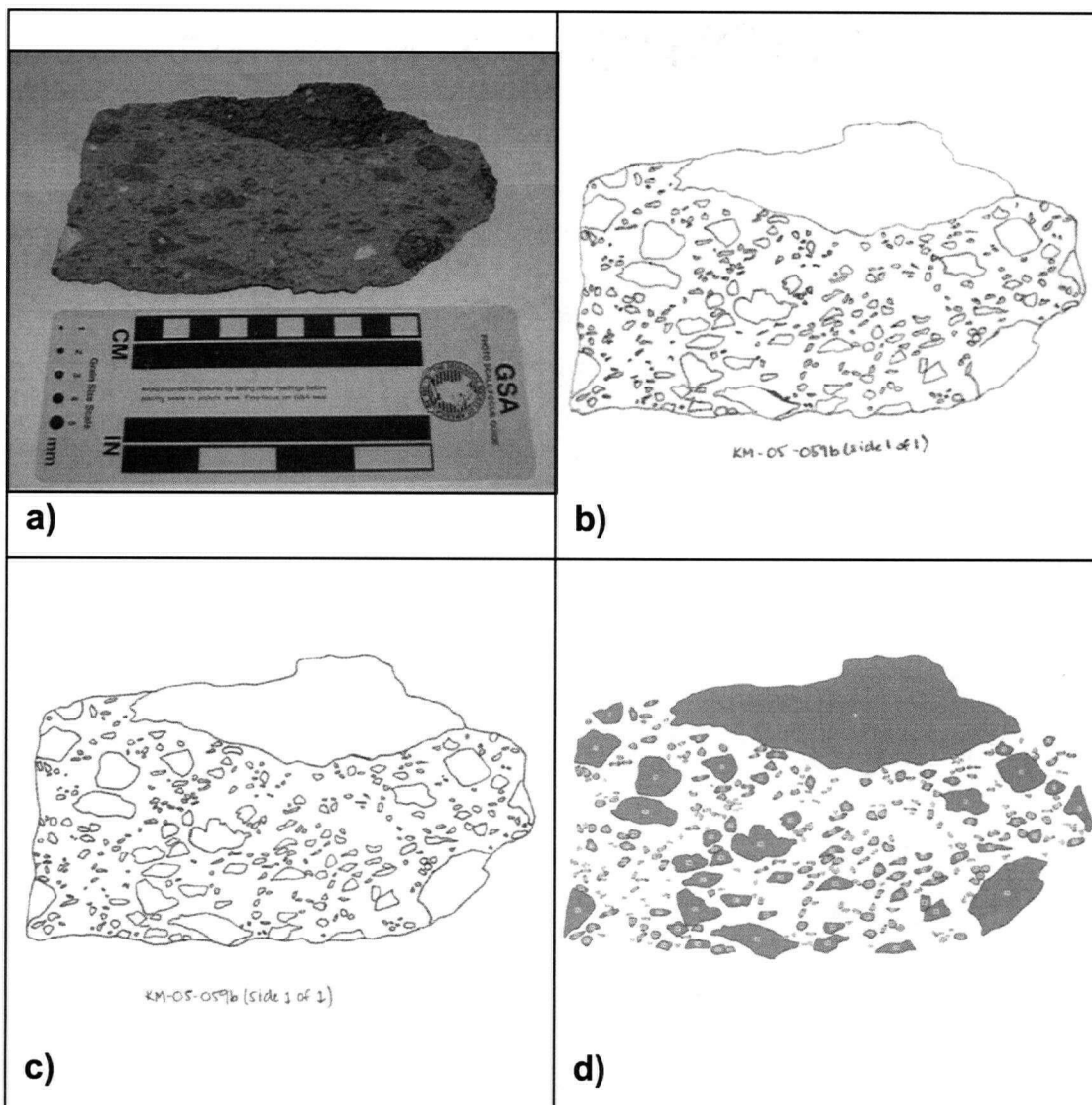
Figure C11: STM 11 – Densely welded facies
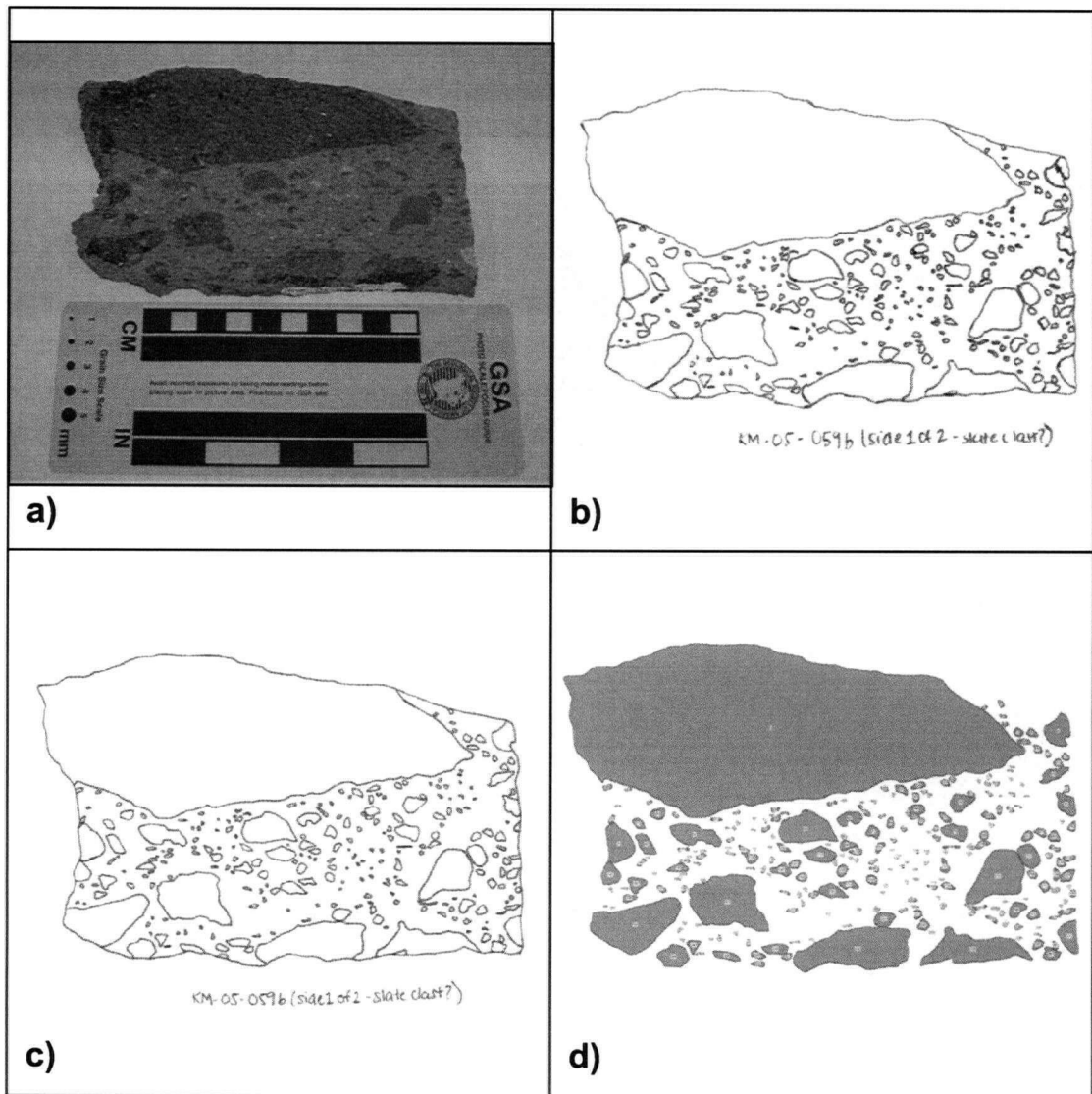
Figure C12: STM 12 – Densely welded facies
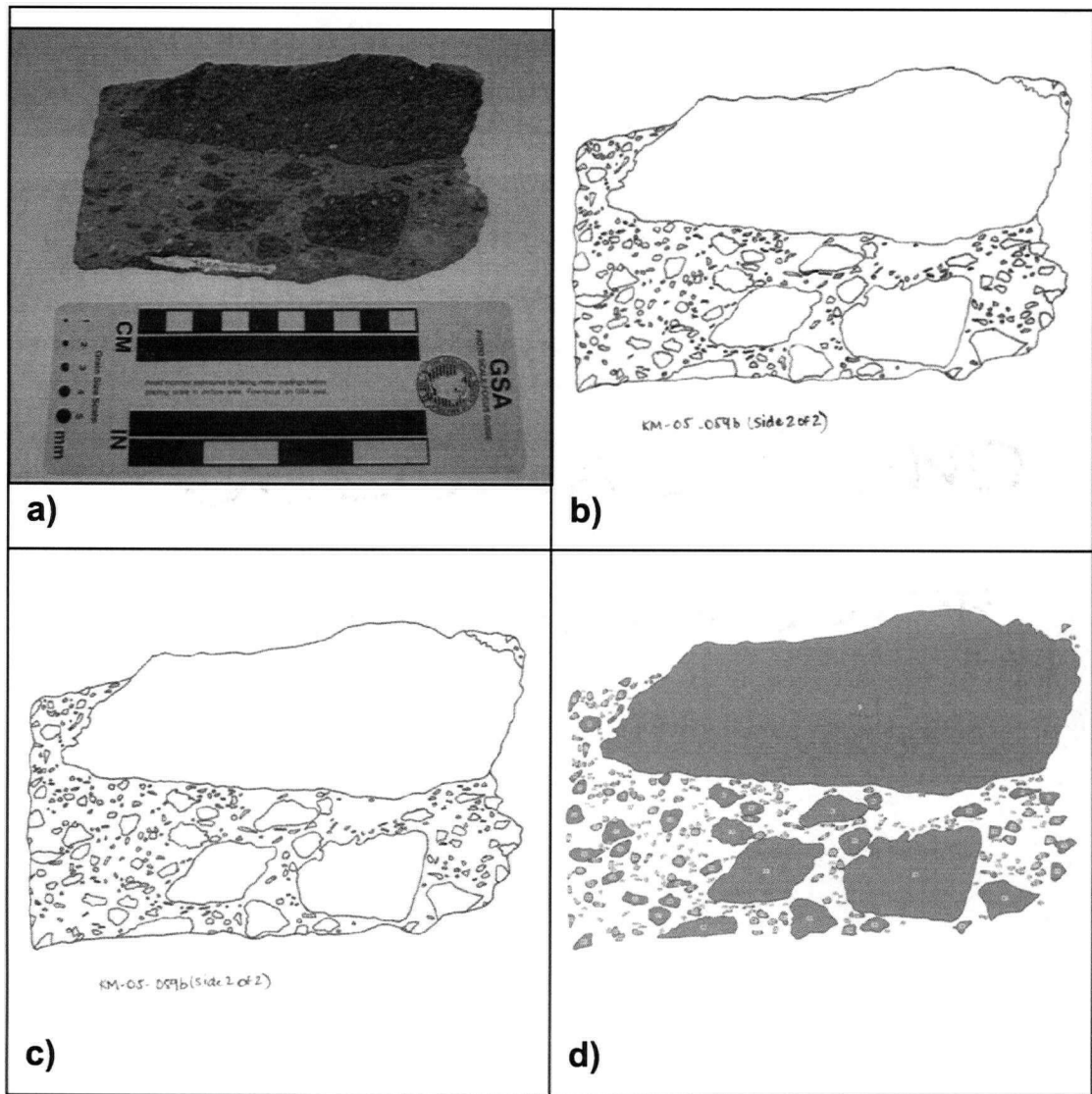
Figure C13: STM 13 – Densely welded facies
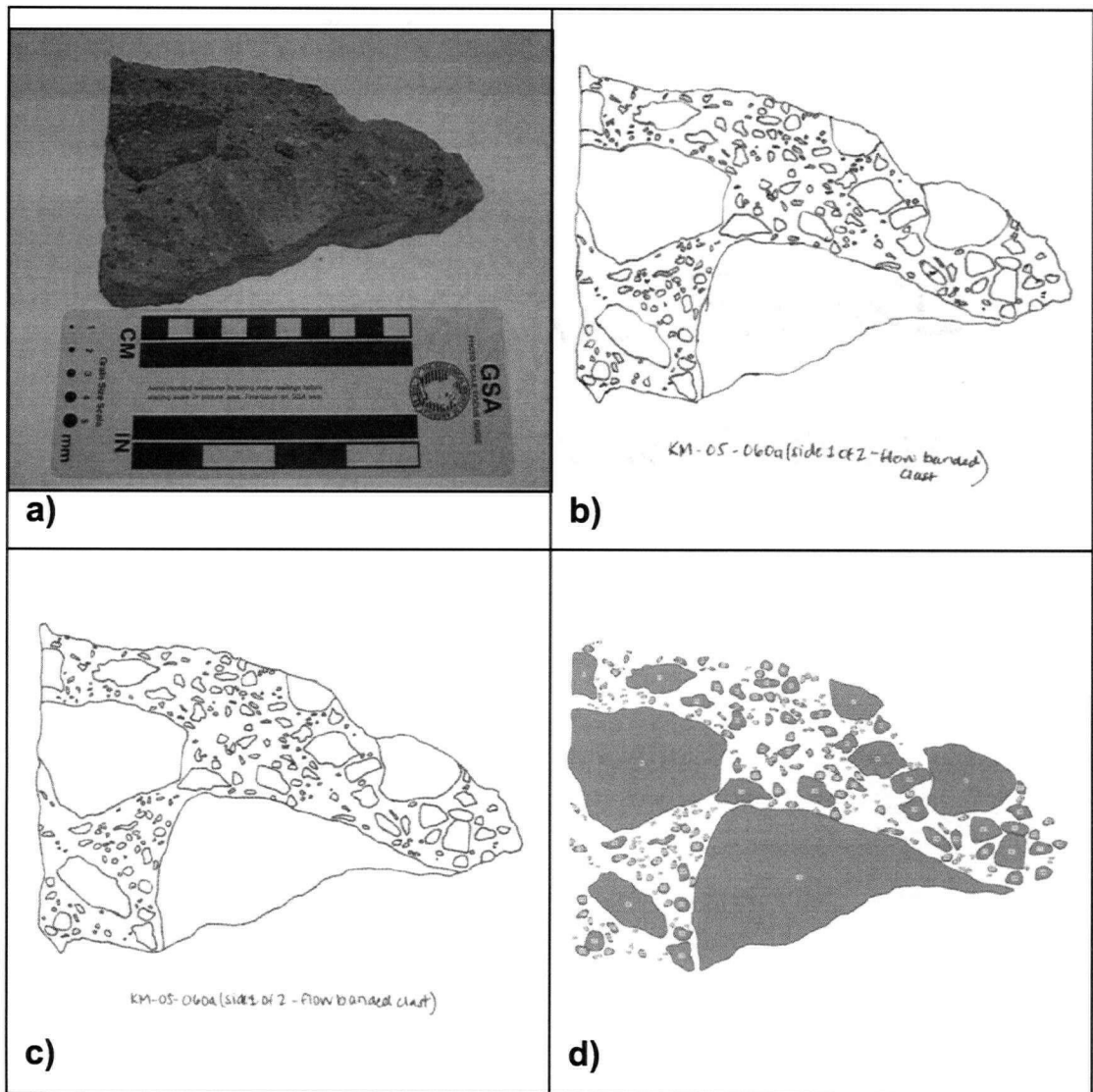
Figure C14: STM 14 – Densely welded facies
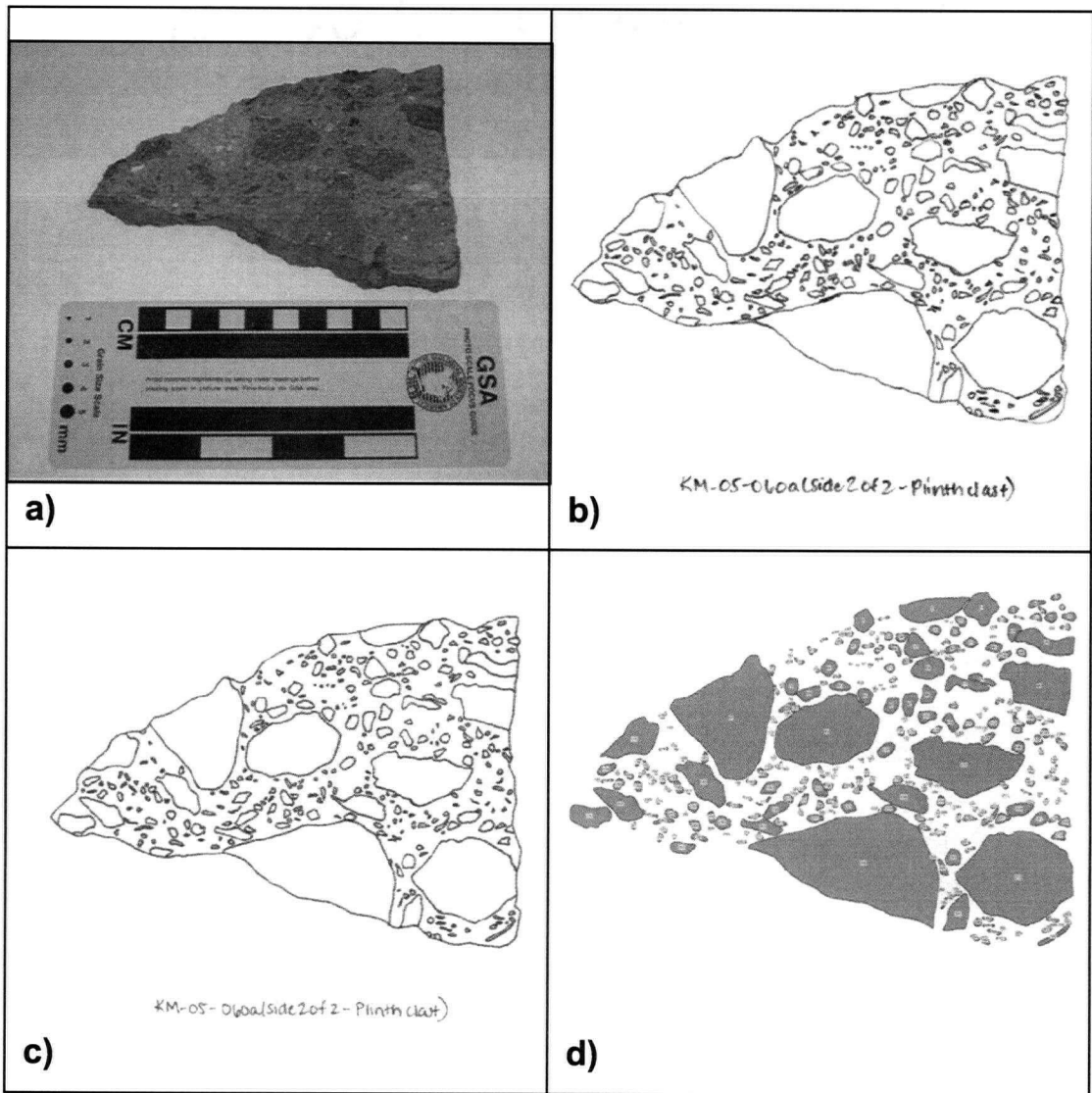
Figure C15: STM 15 – Densely welded facies
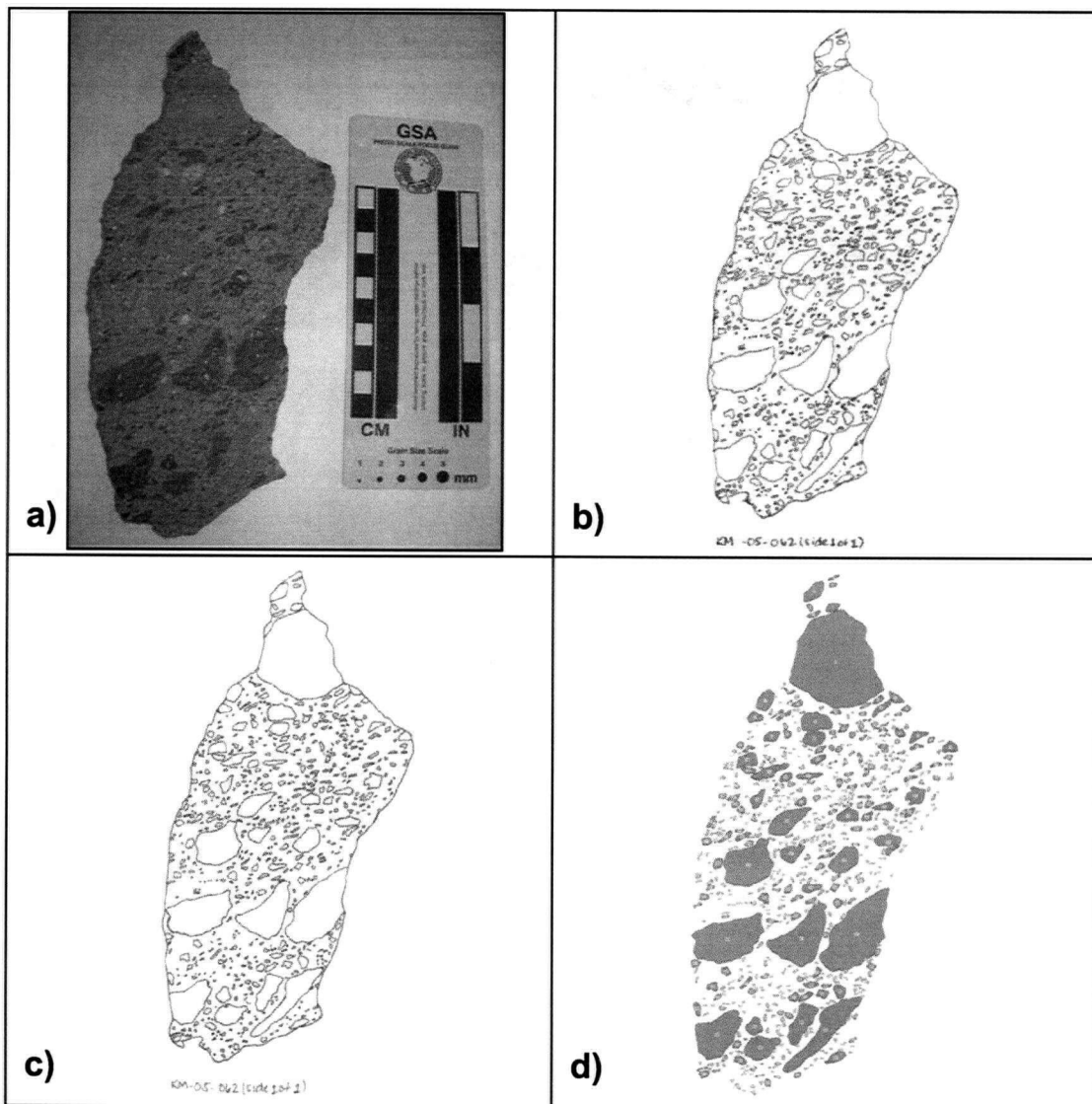
Figure C16: STM 16 – Densely welded facies

APPENDIX D

PHYSICAL PROPERTY MEASUREMENTS & CALCULATIONS

Sample Preparation

1.) All solid rock samples are cut into cores using a drill press and a 30 mm diameter cylindrical drill bit.
2.) The ends of the cored samples are cut with a rock saw and ground down using a lap and 240 Al_2O_3 grit to make a cylinder.
3.) Individual cores are placed in a sonic bath for 5-10 minutes to remove any residual grit or rock fragments.
4.) Cored samples (mass = 26-101 g) are dried in an oven at 120°C for a minimum of 12 hours and cooled to room temperature.
5.) Residual materials (minimum 10 g) from each cored sample are powdered in a tungsten carbide ring mill for 20-60 seconds.

Bulk Density – Consolidated Samples

1.) Digital calipers are used to obtain average values of core height and diameter based on at least six measurements of each.
2.) Using the cylindrical shape of the core, the bulk density is calculated using the geometrical equation for the volume of a cylinder: $V_{bulk} = \pi r^2 h$.
3.) This value of volume is then used to calculate bulk density: $\rho_{bulk} = m_{samp}/ V_{bulk}$.

Quality Control Issues

Accuracy: Digital calipers were used, which are accurate to 0.01 mm; ends were flattened to $\Delta h \leq 0.5$ mm. The balance used is accurate to within 0.001 (<40 g) or 0.01 (>40 g).
Precision: Measurements used are averages of at least six measurements of height and diameter. Results are precise within ±4%.

Bulk Density – Unconsolidated Samples

1.) The mass of a 500 mL graduated cylinder is determined.
2.) The graduated is filled carefully with a precise volume of the unconsolidated material (250-500 mL).
3.) The sample and graduated cylinder (tempered glass) are placed in an oven at 120°C for a minimum of 12 hours, and then cooled to room temperature.
4.) The mass of the graduated cylinder and sample are determined (Fig. D1)
5.) The mass and volume are then used to calculate bulk density: $\rho_{bulk} = m_{samp}/V_{samp}$

Quality Control Issues

Accuracy: The graduated cylinder is accurate to ~5 mL; the balance is accurate to 0.1 g.
Precision: Measurements were done twice to obtain an average and standard deviation. Results are precise within ±4%.

Skeletal Density

1.) Skeletal density is determined using the cored sample and an automated helium pycnometer (Fig. D2i, D3). The largest aluminum cell insert is placed inside the sample and reference cells to maximize the sample to void ratio. Smaller cores require an additional filler (Fig. D2ii) to achieve this result.

2.) Each of the four sample cells and the reference cell of the pycnometer are calibrated against steel spheres of a known volume (Fig. D2iii). The sample cell and reference cell volumes are thus determined by the following equations:

$$V_{cell} = \frac{(V_{known})(P1^* - P2^*)}{(P1^* - P2^*) - (P2^*/P2)(P1 - P2)}, \text{ where } V_{known} = 22.1880 \text{ cm}^3 \text{ (with filler) or}$$

$$31.0082 \text{ cm}^3 \text{ (without filler)}$$

$$V_{ref} = V_{cell}\left(\frac{P1 - P2}{P2}\right)$$

The resulting values of V_{cell} and V_{ref} are calibration factors for each cell. These values are unique to each cell and depend on temperature. They represent an average of five consecutive measurements.

3.) The core is placed in the pycnometer to acquire an averaged value of volume (over five consecutive measurements):

$$V_{skeletal} = V_{cell} - \frac{V_{ref}}{(P1/P2) - 1}$$

4.) The volume acquired is used to calculate skeletal density (that is, the density of rock ± isolated porosity): $\rho_{skeletal} = m_{samp}/V_{skeletal}$.

Quality Control Issues

Accuracy: Experiments were performed on various combinations of steel spheres (of known volume) prior to running samples, in order to check the accuracy of the pycnometer; results were within 1% relative error. The temperature was controlled in such a way (dwell time = 1-2 hrs.) that it varied ≤1°C from time of calibration to the final run of the day. The smallest possible configuration of inserts was used in order to maximize the sample to void space ratio.

Precision: Calibration values are averages of five measurements (five with the cell empty, five with the known volume in the cell); sample volumes are also averages of five consecutive measurements. Results are precise within ±0.3%.

Rock Powder Density

1.) Rock powder density is determined using the powdered sample and an automated helium pycnometer (Fig. D2i, Fig D3). The largest aluminum cell insert and the accompanying filler (Fig. D2ii) are placed inside the sample and reference cells in order to allow large amounts of powder to be used (maximum powder mass = ~45-60 g), thus minimizing the void space to sample ratio.

151

2.) Each of the four sample cells of the pycnometer is calibrated against steel spheres of a known volume (Fig. D2iii). The sample cell and reference cell volumes are thus determined by the following equations:

$$V_{cell} = \frac{(V_{known})(P1^* - P2^*)}{(P1^* - P2^*) - (P2^*/P2)(P1 - P2)}, \text{ where } V_{known} = 22.188 \text{ cm}^3$$

$$V_{ref} = V_{cell}\left(\frac{P1 - P2}{P2}\right)$$

These calibration values are unique to each cell and depend on temperature. They represent an average of five consecutive measurements.

3.) The powder (~15-60 g) is placed in the pycnometer to acquire an averaged value of volume (over five consecutive measurements):

$$V_{rock} = V_{cell} - \frac{V_{ref}}{(P1/P2) - 1}$$

4.) The volume acquired is used to calculate matrix density (that is, the density of the rock only): $\rho_{rock} = m_{samp}/V_{rock}$.

Quality Control Issues

Accuracy: Experiments were performed on various combinations of steel spheres (of known volume) prior to running samples, in order to check the accuracy of the pycnometer; results were within 1% relative error. The temperature was controlled in such a way (dwell time = 1-2 hrs.) that it varied $\leq 1^\circ C$ from time of calibration to the final run of the day. The maximum amount of powder was used in order to ensure that the powder is representative of the sample, and to maximize the sample to void space ratio. Also, a standard powder is measured with the other samples in order to monitor the variability from day to day, run to run.

Precision: Calibration values are averages of five measurements (five with the cell empty, five with the known volume in the cell); sample volumes are also averages of five consecutive measurements. Results are precise within $\pm 0.6\%$.
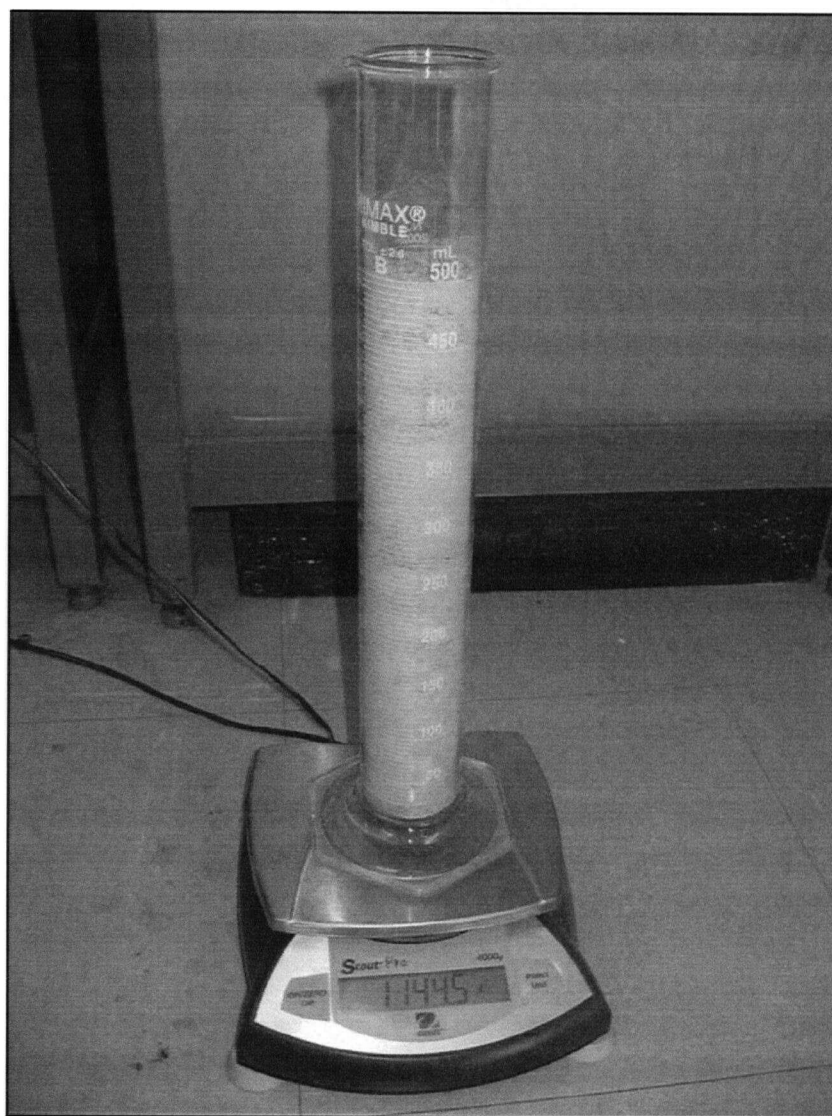
Figure D1: Measurement of bulk density for unconsolidated samples. A 500 mL graduated cylinder is packed full with material and mass is acquired with a digital balance precise to 0.1 g.
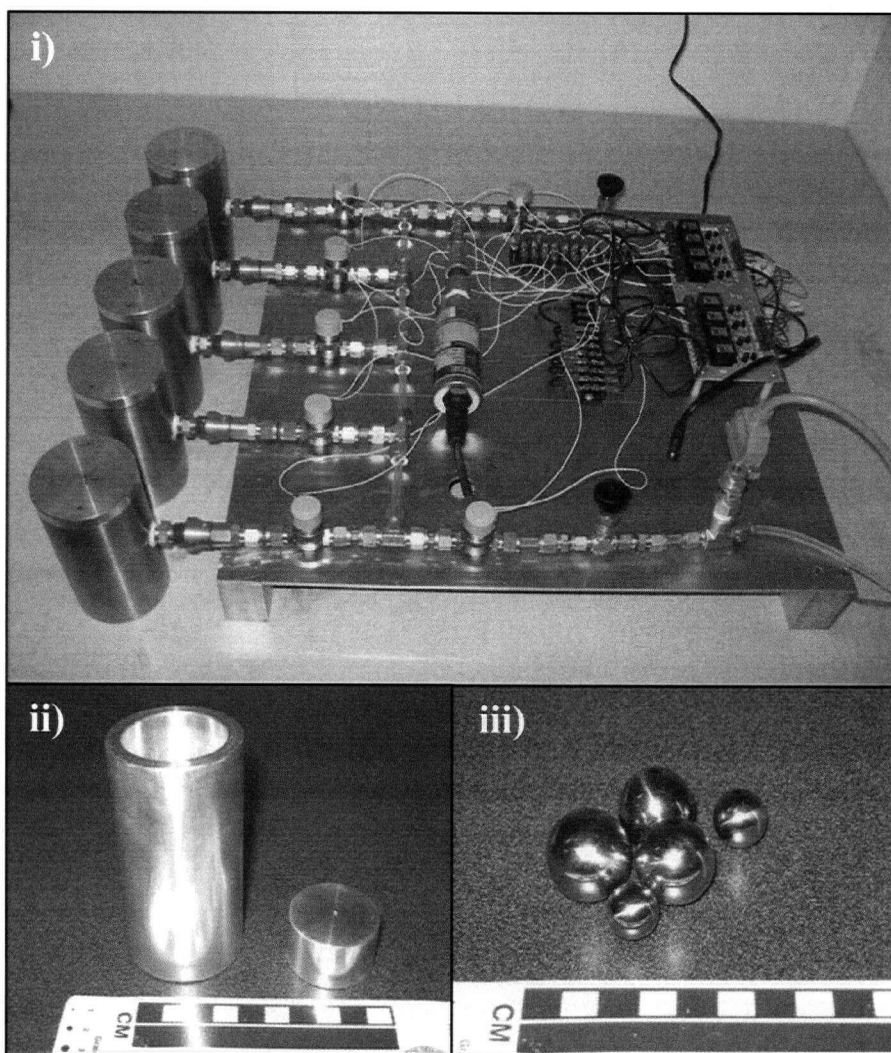
Figure D2: Helium pycnometry setup: **(i)** automatic helium pycnometer; **(ii)** aluminum cell insert (left) and filler (right) for use with smaller samples; **(iii)** steel balls of known volume used for calibration.

low voltage switch

vent rate regulator

vent valve

reference cell

cell #4

cell #3

cell #2

cell #1

circuit board

transducer

fill rate regulator

connector valve

fill valve

overpressure valve

①	to He tank
②	to serial port on computer
③	to parallel port on computer
④	to power source
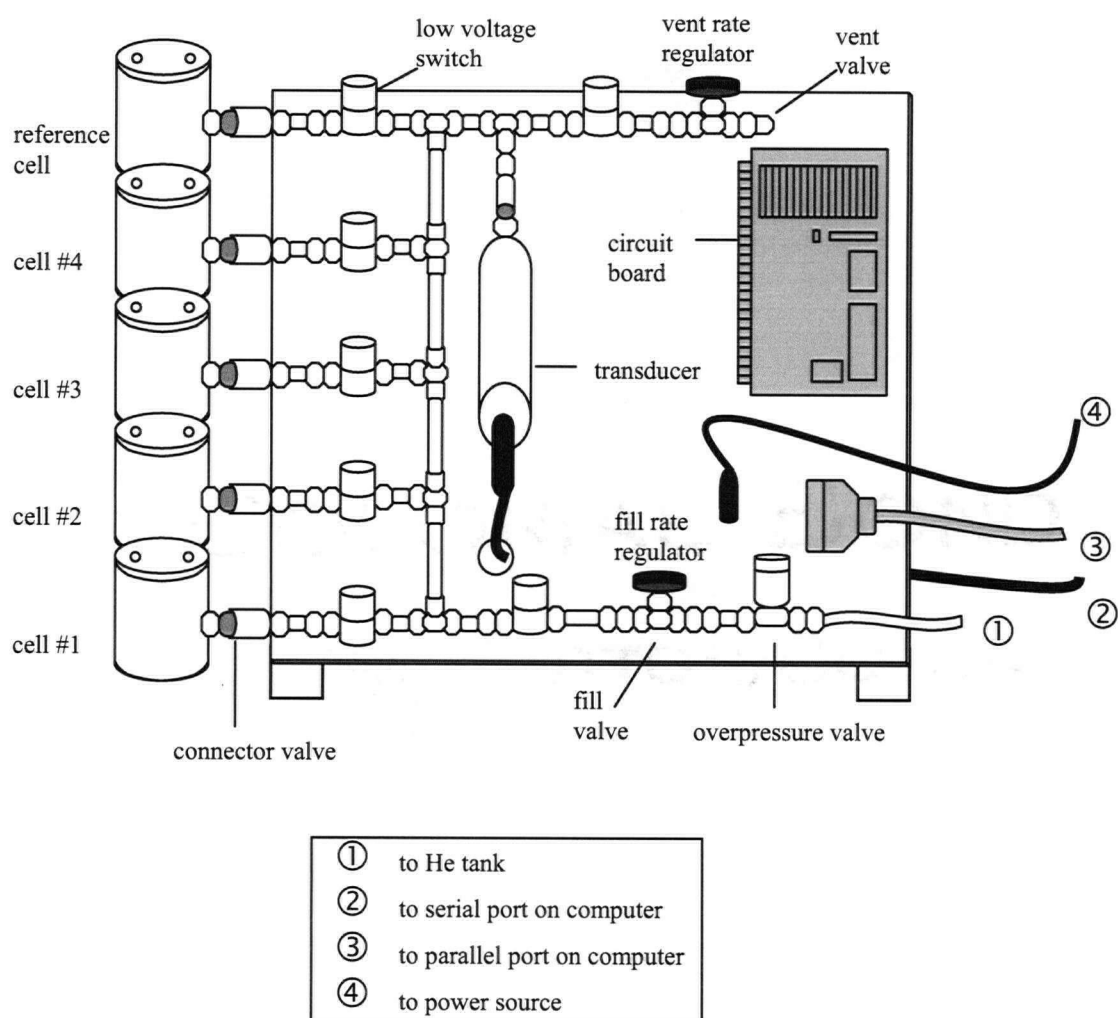
Figure D3: Schematic diagram of automated helium pycnometer, indicating major components and connections.

APPENDIX E

COMPLETE TABLES OF PHYSICAL PROPERTY DATA

Table E1. Full summary of core pycnometry, including: component measured (C = clast, M = matrix), mass (m), volume by geometry (V_{geo}), volume by core pycnometry (V_S), bulk density (ρ_B), skeletal density (ρ_S), and connected porosity (Φ_C). Standard deviations are reported as 1σ.

FIELD SITE	LITHOFACIES	LOCATION	SAMPLE #	C/M	m (g)	σ	V_{geo} (cm³)	σ	V_S (cm³)	σ	ρ_B (g/cm³)	σ	ρ_S (g/cm³)	σ	Φ_C (%)	σ
1	Intermediate, densely welded block and ash flow deposit	Block #3	KM-05-059a(2)	M	52.15	0.010	23.705	0.4932	20.277	0.0243	2.20	0.046	2.572	0.0031	14.46	1.337
			KM-05-060a(1)	M	78.14	0.010	38.061	0.1532	30.350	0.0226	2.05	0.008	2.575	0.0019	20.38	1.241
			KM-05-060a(2)	M	84.22	0.010	40.126	0.3822	33.103	0.0254	2.10	0.020	2.544	0.0020	17.46	1.412
			KM-05-060a(3)	M	76.27	0.010	36.283	0.4518	30.191	0.0255	2.10	0.026	2.526	0.0021	16.87	1.427
			KM-05-060a(4)	M	44.62	0.010	20.905	0.1165	17.715	0.0200	2.13	0.012	2.519	0.0028	15.44	1.125
		Block #4	KM-05-012(1)	M	46.68	0.010	22.566	0.1968	18.181	0.0320	2.08	0.018	2.568	0.0045	18.99	1.760
			KM-05-012(2)	M	44.93	0.010	20.109	0.2605	17.733	0.0355	2.23	0.029	2.534	0.0051	11.99	1.981
			KM-05-012(3)	M	42.23	0.010	20.013	0.8065	16.773	0.0096	2.11	0.085	2.518	0.0014	16.20	0.541
			KM-05-057a(1)	M	49.01	0.010	24.371	0.2308	19.680	0.0263	2.01	0.019	2.490	0.0033	19.29	1.494
			KM-05-057a(2)	M	43.80	0.010	21.385	0.2537	17.381	0.0093	2.05	0.024	2.520	0.0014	18.65	0.524
			KM-05-057a(3)	M	32.62	0.001	16.499	0.3296	12.939	0.0304	1.98	0.039	2.521	0.0059	21.46	1.707
			KM-05-057b(1)	M	82.70	0.010	40.184	0.1800	32.987	0.0222	2.06	0.009	2.507	0.0017	17.83	1.250
			KM-05-057b(2)	M	54.14	0.010	26.904	0.2109	21.527	0.0212	2.01	0.016	2.515	0.0025	20.08	1.190
			KM-05-057b(3)	M	78.94	0.010	38.832	0.1954	31.449	0.0350	2.03	0.010	2.510	0.0028	19.13	1.970
			KM-05-057b(4)	M	62.35	0.010	30.520	0.2929	24.884	0.0300	2.04	0.020	2.506	0.0030	18.58	1.693
			KM-05-057b(5)	M	77.99	0.010	38.840	0.1278	30.980	0.0133	2.01	0.007	2.517	0.0011	20.16	0.748
			KM-05-057b(6)	M	31.25	0.001	15.549	0.2111	12.421	0.0141	2.01	0.027	2.516	0.0029	20.11	0.793
			KM-05-057c(1)	C	98.04	0.010	41.867	0.1665	39.876	0.0125	2.34	0.009	2.459	0.0008	4.82	0.721
			KM-05-057c(2)	C	88.54	0.010	37.959	0.1032	36.188	0.0140	2.33	0.006	2.447	0.0009	4.77	0.810
			KM-05-057c(3)	C/M	98.14	0.010	42.456	0.3043	39.722	0.0231	2.31	0.017	2.471	0.0014	6.50	1.325
			KM-05-057c(4)	C/M	101.02	0.010	44.993	0.2366	40.752	0.0140	2.25	0.012	2.479	0.0008	9.23	0.797
			KM-05-057c(5)	C/M	93.53	0.010	41.040	0.2231	37.935	0.0277	2.28	0.012	2.466	0.0018	7.53	1.588
			KM-05-057c(6)	C	98.44	0.010	41.718	0.2260	40.021	0.0146	2.36	0.013	2.460	0.0009	4.05	0.840
			KM-05-057c(7)	C	85.41	0.010	36.173	0.1431	34.778	0.0073	2.36	0.009	2.456	0.0005	3.90	0.420
			KM-05-057c(8)	C/M	66.47	0.010	31.433	0.4713	26.770	0.0247	2.11	0.032	2.483	0.0023	15.02	1.408
			KM-05-058a(1)	C	47.60	0.010	20.086	0.3470	19.324	0.0091	2.37	0.041	2.463	0.0012	3.78	0.524
			KM-05-058a(2)	M	51.33	0.010	22.944	0.1977	20.674	0.0189	2.24	0.019	2.483	0.0023	9.78	1.075
			KM-05-058a(3)	C/M	52.23	0.010	22.492	0.2241	21.308	0.0168	2.32	0.023	2.451	0.0019	5.35	0.972
			KM-05-058b(1)	M	51.77	0.010	23.909	0.1651	20.555	0.0188	2.17	0.015	2.519	0.0023	13.84	1.055
			KM-05-058b(2)	M	59.91	0.010	27.102	0.5498	23.800	0.0194	2.21	0.045	2.517	0.0021	12.21	1.092

157

		Sample													
		KM-05-058d(1)	M	76.89	0.010	34.795	0.2888	30.478	0.0223	2.21	0.018	2.523	0.0018	12.40	1.249
		KM-05-058d(2a)	M	59.87	0.010	27.927	0.2037	23.748	0.0191	2.14	0.016	2.521	0.0020	15.12	1.072
		KM-05-058d(2b)	M	64.82	0.010	28.607	0.1442	26.168	0.0156	2.27	0.011	2.477	0.0015	8.36	0.893
		KM-05-058d(3)	M	86.05	0.010	37.140	0.3433	34.242	0.0262	2.32	0.021	2.513	0.0019	7.68	1.476
		KM-05-058d(4a)	M	62.96	0.010	27.745	0.1070	25.164	0.0115	2.27	0.009	2.502	0.0011	9.27	0.649
		KM-05-058d(4b)	M	64.29	0.010	29.745	0.1167	25.592	0.0167	2.16	0.008	2.512	0.0016	14.02	0.941
		KM-05-058d(5)	M	54.43	0.010	24.244	0.2584	21.627	0.0178	2.25	0.024	2.517	0.0021	10.60	0.998
		KM-05-058d(6)	M	87.16	0.010	38.962	0.3220	34.913	0.0286	2.24	0.018	2.497	0.0020	10.27	1.618
		KM-05-058d(7)	M	101.08	0.010	45.068	0.1971	40.062	0.0090	2.24	0.010	2.523	0.0006	11.22	0.506
		KM-05-058d(8a)	M	57.84	0.010	26.683	0.1324	23.911	0.0117	2.17	0.011	2.419	0.0012	10.29	0.683
		KM-05-058d(8b)	M	60.54	0.010	28.311	0.1531	23.702	0.0081	2.14	0.012	2.554	0.0009	16.22	0.446
	Block #5	KM-05-017b(1a)	M	65.05	0.010	30.111	0.3105	25.450	0.0285	2.16	0.022	2.556	0.0029	15.45	1.576
		KM-05-017b(1b)	M	67.89	0.010	31.800	0.2863	26.659	0.0095	2.13	0.019	2.547	0.0009	16.16	0.528
		KM-05-017b(2)	M	88.00	0.010	41.283	0.2432	34.574	0.0259	2.13	0.013	2.545	0.0019	16.24	1.439
		KM-05-017b(3)	M	63.61	0.010	29.915	0.1969	24.803	0.0232	2.13	0.014	2.565	0.0024	17.10	1.282
		KM-05-017b(4)	M	79.62	0.010	37.538	0.1964	31.501	0.0222	2.12	0.011	2.528	0.0018	16.08	1.243
		KM-05-017b(5a)	M	61.02	0.010	28.827	0.3113	24.065	0.0238	2.12	0.023	2.536	0.0025	16.51	1.327
		KM-05-017b(5b)	M	67.11	0.010	31.709	0.2013	26.268	0.0125	2.12	0.013	2.555	0.0012	17.14	0.690
		KM-05-017b(6)	C	63.55	0.010	26.896	0.3551	25.861	0.0257	2.36	0.031	2.457	0.0024	3.84	1.478
		KM-05-017b(7)	C/M	48.54	0.010	21.147	0.1212	18.826	0.0389	2.30	0.013	2.578	0.0053	10.99	2.133
		KM-05-017c(1)	M	36.24	0.001	17.048	0.2582	14.130	0.0455	2.13	0.032	2.565	0.0083	17.11	2.510
		KM-05-017c(2)	C	50.82	0.010	22.134	0.2447	20.614	0.0233	2.30	0.025	2.465	0.0028	6.87	1.334
		KM-05-018d(1)	M	41.51	0.010	19.921	0.1945	16.287	0.0260	2.08	0.020	2.549	0.0041	18.23	1.444
		KM-05-018d(2)	C	62.03	0.010	27.023	0.1967	25.387	0.0162	2.30	0.017	2.443	0.0016	6.03	0.939
		KM-05-018d(3)	C	49.07	0.010	21.611	0.2641	20.265	0.0196	2.27	0.028	2.421	0.0023	6.21	1.144
		KM-05-019b(1)	C	92.07	0.010	39.060	0.2635	36.665	0.0288	2.36	0.016	2.511	0.0020	6.14	1.621
		KM-05-019b(2)	C	81.18	0.010	34.236	0.2966	32.760	0.0108	2.37	0.021	2.478	0.0008	4.32	0.617
	Near Classic	KM-05-063(1)	M	39.30	0.001	18.740	0.3022	15.675	0.0263	2.10	0.034	2.507	0.0042	16.24	1.484
		KM-05-063(2)	M	39.51	0.001	19.300	0.2449	15.951	0.0204	2.05	0.026	2.477	0.0032	17.24	1.165
		KM-05-063(3)	M	94.25	0.010	44.745	0.3688	37.494	0.0165	2.11	0.017	2.514	0.0011	16.06	0.931
		KM-05-063(4)	M	52.49	0.010	26.025	0.1858	20.417	0.0196	2.02	0.014	2.571	0.0025	21.43	1.077
		KM-05-063(5)	M	49.00	0.010	23.053	0.3241	19.457	0.0295	2.13	0.030	2.518	0.0038	15.42	1.658
		KM-05-063(6)	M	51.15	0.010	24.483	0.3909	20.321	0.0295	2.09	0.033	2.517	0.0037	16.97	1.658
Basal, non-	Base of	KM-05-023	bulk	57.13	0.010	-	-	22.713	0.0152	1.54	0.028	2.515	0.0017	38.73	0.867

	Description	Section	Sample	Type												
	welded block and ash flow deposit	Classic Section	KM-05-024(1)	C	68.39	0.010	44.833	0.1092	30.032	0.0215	1.53	0.004	2.277	0.0016	32.81	1.335
			KM-05-024(2a)	C	46.30	0.010	29.589	0.3119	20.028	0.0471	1.56	0.016	2.312	0.0054	32.52	2.882
			KM-05-024(2b)	C	47.46	0.010	31.559	0.2277	21.164	0.0122	1.50	0.011	2.243	0.0013	33.11	0.771
			KM-05-024(3)	C	70.94	0.010	45.541	0.3387	31.486	0.0306	1.56	0.012	2.253	0.0022	30.76	1.920
			KM-05-024(4a)	C	41.75	0.010	27.613	0.2063	18.501	0.0232	1.51	0.011	2.257	0.0028	33.09	1.457
			KM-05-024(4b)	C	49.16	0.010	31.335	0.2383	21.808	0.0334	1.57	0.012	2.254	0.0035	30.35	2.095
			KM-05-026(1)	C	49.46	0.010	30.197	0.1215	21.629	0.0267	1.64	0.007	2.287	0.0028	28.28	1.651
			KM-05-026(2)	C	60.37	0.010	36.435	0.2000	26.006	0.0238	1.66	0.009	2.321	0.0021	28.49	1.450
			KM-05-026(3)	C	68.37	0.010	40.454	0.2160	29.183	0.0372	1.69	0.009	2.343	0.0030	27.90	2.245
			KM-05-026(4)	C	42.33	0.010	27.015	0.2276	18.692	0.0202	1.57	0.013	2.265	0.0025	30.67	1.264
			KM-05-046(1)	C	26.14	0.001	15.926	0.1661	11.401	0.0349	1.64	0.017	2.293	0.0070	28.47	2.155
			KM-05-046(2)	C	60.37	0.010	28.130	0.2520	26.006	0.0238	1.80	0.016	2.335	0.0021	22.92	1.441
			KM-05-046(3)	C	89.09	0.010	47.503	0.4274	37.535	0.0662	1.88	0.017	2.374	0.0042	20.79	3.946
			KM-05-046(4)	C	36.81	0.001	19.549	0.1356	15.665	0.0269	1.88	0.013	2.350	0.0040	19.99	1.616
2	Upper, incipiently welded (oxidized) block and ash flow deposit	Oxidized Roadcut	KM-04-018	bulk	56.14	0.010	-	-	22.504	0.0267	1.47	0.003	2.495	0.0030	41.15	1.516
			KM-04-019	bulk	52.16	0.010	-	-	20.735	0.0185	1.48	0.012	2.516	0.0022	41.25	1.042
			KM-04-020	bulk	61.94	0.010	-	-	24.633	0.0161	1.52	0.014	2.515	0.0016	39.51	0.905
			KM-05-032	bulk	59.87	0.010	-	-	23.723	0.0062	1.39	0.028	2.524	0.0007	44.84	0.349
		Near TM#10	KM-05-033(1)	C	100.18	0.010	47.711	0.2490	40.772	0.0215	2.10	0.011	2.457	0.0013	14.53	1.236
			KM-05-033(2)	C	60.29	0.010	29.393	0.2772	24.745	0.0296	2.05	0.019	2.437	0.0029	15.86	1.719
			KM-05-033(3)	C	60.07	0.010	28.759	0.1722	24.566	0.0168	2.09	0.013	2.445	0.0017	14.53	0.969
		Near TM#12	KM-05-056(1a)	C	62.80	0.010	31.986	0.1776	25.955	0.0344	1.96	0.011	2.420	0.0032	18.99	2.012
			KM-05-056(1b)	C	67.55	0.010	33.751	0.2454	28.349	0.0364	2.00	0.015	2.383	0.0031	16.06	2.161
			KM-05-056(2a)	C	47.33	0.010	24.097	0.2446	19.779	0.0313	1.96	0.020	2.393	0.0038	18.09	1.851
			KM-05-056(2b)	C	53.05	0.010	27.107	0.2304	22.434	0.0207	1.96	0.017	2.365	0.0022	17.11	1.240
			KM-05-056(3)	C	67.08	0.010	33.950	0.2931	28.615	0.0253	1.98	0.017	2.344	0.0021	15.54	1.526
3	Upper, non-welded, block and ash flow deposit	Keyhole Falls	KM-04-031	bulk	68.14	0.010	-	-	26.868	0.0212	1.59	0.025	2.536	0.0020	37.35	1.184
			KM-05-036	bulk	45.49	0.010	-	-	17.964	0.0076	1.43	0.057	2.532	0.0011	43.49	0.422
			KM-05-043(1)	C	44.38	0.010	26.917	0.0744	18.301	0.0205	1.65	0.005	2.425	0.0027	31.96	1.194
			KM-05-043(2)	C	60.31	0.010	34.257	0.1433	24.964	0.0250	1.76	0.007	2.416	0.0024	27.15	1.463
			KM-05-043(3)	C	49.20	0.010	30.336	0.1658	20.780	0.0228	1.62	0.009	2.368	0.0026	31.58	1.364
			KM-05-043(4)	C	54.20	0.010	30.108	0.1254	22.542	0.0250	1.80	0.008	2.404	0.0027	25.14	1.469
			KM-05-044(1)	C	74.62	0.010	43.432	0.2176	29.858	0.0100	1.72	0.009	2.499	0.0008	31.18	0.565

KM-05-044(2)	C	72.17	0.010	41.652	0.1323	28.971	0.0222	1.73	0.006	2.491	0.0019	30.55	1.262
KM-05-044(3)	C	82.89	0.010	47.322	0.1470	32.890	0.0197	1.75	0.005	2.520	0.0015	30.56	1.107
KM-05-044(4)	C	82.27	0.010	45.654	0.4345	33.158	0.0138	1.82	0.017	2.511	0.0010	27.53	0.775
KM-05-045(1)	C	55.27	0.010	29.191	0.1667	21.931	0.0113	1.89	0.011	2.520	0.0013	25.01	0.632
KM-05-045(2)	C	58.16	0.010	30.927	0.2378	23.170	0.0209	1.88	0.014	2.510	0.0023	25.10	1.178
KM-05-054(1)	C	73.31	0.010	45.054	0.0964	30.615	0.0238	1.63	0.003	2.395	0.0019	31.93	1.408
KM-05-054(2)	C	71.23	0.010	43.144	0.1561	29.375	0.0224	1.65	0.006	2.425	0.0018	31.95	1.305
KM-05-054(3)	C	33.44	0.001	20.665	0.2319	14.072	0.0190	1.62	0.018	2.376	0.0032	31.83	1.131
KM-05-054(4)	C	50.71	0.010	31.805	0.1113	21.105	0.0157	1.59	0.006	2.403	0.0018	33.83	0.922

Table E2. Full summary of rock powder pycnometry, including: field site (FS), lithofacies (LF), location (LOC), component measured (C = clast, M = matrix), mass of powder (m_R), volume of powder (V_R), rock powder density (ρ_R), total porosity (Φ_T), connected porosity (Φ_C), and isolated porosity (Φ_I). Standard deviations are reported as 1σ.

FS	LF	LOC	SAMPLE #	C/M	m_R (g)	σ	V_R (cm^3)	σ	ρ_R (g/cm^3)	σ	Φ_T (%)	σ	+/-	Φ_I (%)	σ
1	Intermediate, densely welded block and ash flow deposit	Block #1	KM-05-061(1)	M	28.51	0.001	11.245	0.0302	2.535	0.0068	-	-	-	-	-
			KM-05-062(3)	M	46.75	0.010	18.674	0.0168	2.504	0.0023	-	-	-	-	-
		Block #3	KM-05-059a(1)	M	26.87	0.001	10.335	0.0117	2.600	0.0029	15.38	1.763	1.782	1.08	0.163
			KM-05-059a(2)	M	45.04	0.010	17.763	0.0059	2.536	0.0010	13.23	1.805	1.782	-1.43	0.128
			KM-05-060a(1)	M	33.22	0.001	13.032	0.0092	2.549	0.0018	19.58	0.329	0.326	-1.00	0.104
			KM-05-060a(2)	M	38.69	0.001	15.333	0.0140	2.523	0.0023	16.77	0.796	0.788	-0.83	0.120
			KM-05-060a(3)	M	37.51	0.001	14.713	0.0130	2.550	0.0023	17.63	1.029	1.039	0.91	0.121
			KM-05-060a(4)	M	45.33	0.010	17.963	0.0092	2.524	0.0014	15.60	0.474	0.482	0.19	0.126
		Block #4	KM-05-012(1)	M	28.60	0.001	11.252	0.0132	2.542	0.0030	18.17	0.719	0.717	-1.01	0.213
			KM-05-012(2)	M	24.03	0.001	9.396	0.0260	2.557	0.0071	12.80	1.157	1.156	0.93	0.339
			KM-05-012(3)	M	25.10	0.001	9.773	0.0158	2.568	0.0041	17.85	3.313	3.378	1.97	0.168
			KM-05-057a(1)	M	24.43	0.001	9.429	0.0348	2.591	0.0096	22.43	0.789	0.772	3.89	0.378
			KM-05-057a(2)	M	21.00	0.001	8.350	0.0280	2.515	0.0084	18.49	1.004	0.965	-0.20	0.340
			KM-05-057a(3)	M	32.23	0.001	12.599	0.0250	2.558	0.0051	22.60	1.552	1.577	1.45	0.303
			KM-05-057b(1)	M	35.04	0.001	14.039	0.0197	2.496	0.0035	17.46	0.387	0.372	-0.45	0.156
			KM-05-057b(2)	M	38.09	0.001	15.187	0.0111	2.508	0.0018	19.86	0.632	0.632	-0.28	0.123
			KM-05-057b(3)	M	27.26	0.001	10.779	0.0061	2.529	0.0014	19.73	0.407	0.417	0.74	0.124
			KM-05-057b(4)	M	28.76	0.001	11.530	0.0031	2.494	0.0007	18.21	0.786	0.789	-0.45	0.124
			KM-05-057b(5)	M	28.08	0.001	10.966	0.0206	2.561	0.0048	21.50	0.297	0.265	1.69	0.189
			KM-05-057b(6)	M	46.38	0.010	18.207	0.0231	2.547	0.0033	21.09	1.076	1.088	1.24	0.169
			KM-05-057c(1)	C	26.61	0.001	10.634	0.0048	2.502	0.0011	6.49	0.374	0.380	1.75	0.054
			KM-05-057c(2)	C	37.87	0.001	15.331	0.0107	2.470	0.0017	5.68	0.265	0.262	0.95	0.079
			KM-05-057c(3)	C/M	28.75	0.001	11.496	0.0211	2.501	0.0046	7.63	0.684	0.673	1.20	0.190
			KM-05-057c(4)	C/M	40.08	0.010	16.035	0.0171	2.500	0.0027	9.98	0.483	0.477	0.82	0.114
			KM-05-057c(5)	C/M	37.21	0.001	15.135	0.0021	2.459	0.0003	7.26	0.504	0.507	-0.28	0.075

161

		Sample	Type											
		KM-05-057c(6)	C	32.58	0.001	13.314	0.0144	2.447	0.0027	3.56	0.533	0.521	-0.51	0.115
		KM-05-057c(7)	C	19.07	0.001	7.647	0.0056	2.494	0.0018	5.37	0.381	0.381	1.53	0.075
		KM-05-057c(8)	C/M	31.07	0.001	12.374	0.0303	2.511	0.0061	15.97	1.279	0.078	1.12	0.258
		KM-05-058a(1)	C	31.36	0.001	12.530	0.0185	2.503	0.0037	5.30	1.642	0.045	1.58	0.153
		KM-05-058a(2)	M	28.43	0.001	11.112	0.0114	2.559	0.0026	12.45	0.759	0.082	2.96	0.133
		KM-05-058a(3)	C/M	25.13	0.001	10.043	0.0173	2.502	0.0043	7.29	0.938	0.947	2.04	0.185
		KM-05-058b(1)	M	37.07	0.001	14.596	0.0104	2.540	0.0018	14.56	0.592	0.599	0.83	0.115
		KM-05-058b(2)	M	39.16	0.001	15.438	0.0067	2.537	0.0011	12.88	1.768	1.783	0.76	0.092
		KM-05-058d(1)	M	45.69	0.010	18.153	0.0345	2.517	0.0048	12.20	0.748	0.730	-0.23	0.205
		KM-05-058d(2)	M	37.93	0.001	14.903	0.0216	2.545	0.0037	15.92	0.626	0.624	0.95	0.164
		KM-05-058d(4)	M	34.40	0.001	13.454	0.0176	2.557	0.0033	15.52	0.350	0.342	1.75	0.144
		KM-05-058d(5)	M	48.95	0.010	19.442	0.0288	2.518	0.0038	10.63	0.960	0.954	0.04	0.171
		KM-05-058d(6)	M	40.83	0.010	16.250	0.0112	2.513	0.0018	10.85	0.739	0.744	0.64	0.109
		KM-05-058d(7)	M	48.78	0.010	18.998	0.0104	2.568	0.0015	12.76	0.385	0.389	1.73	0.062
		KM-05-058d(8)	M	44.97	0.010	17.814	0.0233	2.524	0.0033	15.23	0.472	0.454	-1.18	0.138
		KM-05-017b(1)	M	45.58	0.010	17.981	0.0318	2.535	0.0045	15.77	0.773	0.755	-0.46	0.182
		KM-05-017b(2)	M	45.01	0.010	17.713	0.0212	2.541	0.0031	16.10	0.505	0.497	-0.17	0.143
		KM-05-017b(3)	M	15.20	0.001	6.047	0.0180	2.514	0.0075	15.43	0.611	0.551	-2.02	0.318
		KM-05-017b(4)	M	46.03	0.010	18.183	0.0084	2.532	0.0013	16.26	0.440	0.443	0.16	0.087
		KM-05-017b(5)	M	43.08	0.010	17.003	0.0244	2.534	0.0037	16.45	0.910	0.905	-0.07	0.176
		KM-05-017b(6)	C	32.11	0.001	13.040	0.0204	2.462	0.0038	4.04	1.276	1.273	0.20	0.185
	Block #5	KM-05-017b(7)	C/M	47.69	0.010	18.737	0.0235	2.545	0.0032	9.64	0.530	0.542	-1.30	0.246
		KM-05-017c(1)	M	22.84	0.001	8.807	0.0566	2.594	0.0167	18.37	1.347	1.283	1.11	0.711
		KM-05-018d(1)	M	16.78	0.001	6.684	0.0169	2.510	0.0063	16.99	0.837	0.809	-1.53	0.304
		KM-05-018d(2)	C	23.21	0.001	9.368	0.0418	2.478	0.0111	4.63	0.798	0.686	1.38	0.445
		KM-05-018d(3)	C	19.61	0.001	7.968	0.0210	2.461	0.0065	6.75	1.154	1.149	1.62	0.276
		KM-05-019b(1)	C	35.58	0.001	14.308	0.0378	2.487	0.0066	5.10	0.687	0.638	-0.98	0.279
		KM-05-019b(2)	C	34.75	0.001	13.697	0.0434	2.537	0.0080	6.55	0.862	0.829	2.33	0.311
Intermediate, moderately welded block and ash flow deposit	Near Classic	KM-05-063(1)	M	45.37	0.010	17.957	0.0079	2.527	0.0012	16.88	1.339	1.356	0.77	0.173
		KM-05-063(2)	M	45.37	0.010	17.976	0.0164	2.524	0.0024	18.78	1.032	1.054	1.86	0.156
		KM-05-063(3)	M	41.15	0.010	16.164	0.0075	2.546	0.0013	17.12	0.683	0.692	1.26	0.068
		KM-05-063(4)	M	45.47	0.010	17.985	0.0130	2.528	0.0019	20.10	0.573	0.565	-1.69	0.124
		KM-05-063(5)	M	45.66	0.010	18.056	0.0136	2.529	0.0020	15.77	1.184	1.194	0.41	0.170
		KM-05-063(6)	M	45.39	0.010	18.108	0.0285	2.507	0.0040	16.62	1.337	1.331	-0.42	0.216

			Sample	Type											
	Basal, non-welded block and ash flow deposit	Base of Classic	KM-05-023	bulk	47.15	0.010	18.501	0.0190	2.549	0.0026	39.53	1.112	0.041	1.30	0.145
			KM-05-024(1)	C	35.07	0.001	14.024	0.0404	2.501	0.0072	38.82	0.231	0.170	8.94	0.270
			KM-05-024(2)	C	33.13	0.001	13.175	0.0225	2.515	0.0043	40.35	0.443	0.485	10.82	0.161
			KM-05-024(3)	C	45.93	0.010	18.381	0.0135	2.499	0.0019	37.57	0.466	0.519	9.83	0.112
			KM-05-024(4)	C	31.50	0.001	12.643	0.0369	2.492	0.0073	39.40	0.487	0.508	9.43	0.288
			KM-05-026(1)	C	46.74	0.010	18.715	0.0225	2.498	0.0031	34.33	0.277	0.301	8.44	0.159
			KM-05-026(2)	C	35.91	0.001	14.476	0.0165	2.481	0.0028	33.08	0.374	0.397	6.42	0.137
			KM-05-026(3)	C	35.22	0.001	14.212	0.0238	2.478	0.0041	31.80	0.382	0.396	5.45	0.199
			KM-05-026(4)	C	40.60	0.010	16.509	0.0228	2.459	0.0035	36.16	0.544	0.588	7.92	0.163
			KM-05-046(1)	C	28.64	0.001	11.570	0.0110	2.475	0.0024	33.75	0.694	0.778	7.37	0.297
			KM-05-046(2)	C	45.61	0.010	18.387	0.0083	2.481	0.0012	27.44	0.650	0.833	5.86	0.098
			KM-05-046(3)	C	45.65	0.010	18.331	0.0226	2.490	0.0031	24.51	0.684	0.724	4.69	0.206
			KM-05-046(4)	C	45.72	0.010	18.513	0.0173	2.470	0.0024	23.87	0.534	0.573	4.85	0.187
2	Upper, incipiently welded (oxidized) block and ash flow deposit	Near TM#10 (oxidized roadcut)	KM-05-031	C	50.45	0.010	20.407	0.0101	2.472	0.0013	-	-	-	-	-
			KM-05-032	bulk	41.22	0.010	16.277	0.0239	2.532	0.0038	45.03	1.092	0.014	0.34	0.151
			KM-05-033(1)	C	50.43	0.010	20.149	0.0193	2.503	0.0025	16.10	0.445	0.448	1.83	0.109
			KM-05-033(2)	C	47.49	0.010	18.985	0.0041	2.501	0.0008	18.05	0.774	0.800	2.59	0.120
			KM-05-033(3)	C	49.15	0.010	19.737	0.0078	2.490	0.0011	16.07	0.504	0.515	1.81	0.080
		Near TM#12 (oxidized roadcut)	KM-05-056(1)	C	42.44	0.010	17.096	0.0132	2.482	0.0020	21.05	0.444	0.463	2.53	0.151
			KM-05-056(2)	C	21.73	0.001	8.680	0.0128	2.504	0.0037	21.71	0.674	0.708	5.55	0.164
			KM-05-056(3a)	C	48.21	0.010	19.502	0.0056	2.472	0.0009	19.90	0.691	0.731	5.17	0.090
			KM-05-056(3b)	C	46.09	0.010	18.737	0.0175	2.460	0.0024	19.51	0.698	0.731	4.70	0.124
		Oxidized Roadcut	KM-04-018	bulk	50.06	0.010	19.741	0.0436	2.536	0.0056	42.11	0.170	0.070	1.62	0.248
			KM-04-019	bulk	50.28	0.010	19.709	0.0162	2.551	0.0022	42.07	0.479	0.053	1.40	0.121
			KM-04-020	bulk	37.45	0.001	14.832	0.0112	2.525	0.0019	39.76	0.568	0.040	0.41	0.100
3	Upper, non-welded, block and ash flow deposit	Keyhole Falls	KM-04-031	bulk	51.63	0.010	20.220	0.0119	2.553	0.0016	37.77	0.976	0.050	0.68	0.100
			KM-05-036	bulk	50.55	0.010	19.941	0.0090	2.535	0.0013	43.55	2.265	0.024	0.11	0.065
			KM-05-043(1)	C	40.40	0.010	16.146	0.0210	2.502	0.0033	34.06	0.202	0.203	3.08	0.168
			KM-05-043(2)	C	40.49	0.010	16.136	0.0273	2.509	0.0043	29.86	0.317	0.313	3.73	0.191
			KM-05-043(3)	C	30.80	0.001	12.264	0.0142	2.512	0.0029	35.50	0.361	0.382	5.73	0.150
			KM-05-043(4)	C	42.31	0.010	16.962	0.0225	2.494	0.0034	27.84	0.316	0.323	3.61	0.168
			KM-05-044(1)	C	18.28	0.001	7.047	0.0239	2.594	0.0088	33.69	0.401	0.345	3.65	0.329
			KM-05-044(2)	C	40.76	0.010	15.973	0.0126	2.552	0.0021	32.20	0.223	0.227	2.38	0.110

KM-05-044(3)	C	28.68	0.001	11.393	0.0145	2.517	0.0032	30.48	0.234	0.220	-0.12	0.141
KM-05-044(4)	C	38.11	0.001	15.023	0.0142	2.537	0.0024	28.26	0.688	0.692	1.01	0.102
KM-05-045(1)	C	43.41	0.010	17.114	0.0107	2.537	0.0017	25.49	0.429	0.431	0.64	0.084
KM-05-045(2)	C	19.58	0.001	7.885	0.0096	2.483	0.0030	24.29	0.590	0.580	-1.08	0.154
KM-05-054(1)	C	36.63	0.001	14.832	0.0072	2.470	0.0012	34.00	0.145	0.155	3.04	0.089
KM-05-054(2)	C	36.45	0.001	14.622	0.0120	2.493	0.0021	33.81	0.246	0.252	2.73	0.109
KM-05-054(3)	C	46.46	0.010	18.619	0.0397	2.495	0.0053	35.08	0.741	0.770	4.77	0.241
KM-05-054(4)	C	46.25	0.010	18.449	0.0364	2.507	0.0050	36.57	0.256	0.237	4.15	0.203